Modelling of Continuum Using Bonded Particle Model

Oskari Nihtilä

School of Engineering

Thesis submitted for examination for the degree of Master of Science in Technology.

Espoo 11.9.2017

Thesis supervisor and advisor:

Ass. Prof. Arttu Polojärvi

Aalto University
School of Engineering

AALTO UNIVERSITY
SCHOOL OF ENGINEERING

ABSTRACT OF THE
MASTER'S THESIS

Author: Oskari Nihtilä

Title: Modelling of Continuum Using Bonded Particle Model

Date: 11.9.2017 Language: English Number of pages: 8+79

Department of Applied Mechanics

Professorship: Technical Mechanics

Supervisor and advisor: Ass. Prof. Arttu Polojärvi

The behaviour of granular, heterogenous and discontinuous materials can be numerically modelled using discrete element methods (DEM). The material is discretized with a large number of finite rigid particles that interact between each other according to predefined contact laws. When modelling the failure of solid continuums with DEM, bonds are introduced between the rigid particles. These bonds can break creating microcracks and finally failure of the material.

In this thesis, a bonded particle model (BPM) is developed with a goal to simulate the elastic behaviour of a solid continuum. The model is implemented in MATLAB. The modelled material is discretized by packing equally sized rigid spheres. The effect of particle size and packing method is studied. Five sphere radii and three packing methods, namely uniform packing, hexagonal closepacking and random closepacking, are used. Additionally, two bond models, a parallel bond model based on multiple springs and a Timoshenko beam model, are implemented in the model.

The model was tested with numerical tensile, compression and three point flexural tests. The simulation results with the random (RCP) and hexagonal closepacked (HCP) specimens suggest that the Young's modulus decreases linearly as a function of porosity. Furthermore, the Poisson's ratio of the RCP specimens showed a converging behaviour as the particle size decreased. The anisotropy of the HCP specimens emerged in the uniaxial tests, as the Poisson's ratios differed in the y- and z-directions. The three point flexural test results indicate that the flexural stiffness is lower than the axial stiffness for all the packing methods. Furthermore, there was no clear increasing trend in the bending stiffness of the specimens as the particle size and porosity were decreased.

Keywords: Discrete element methods, bonded particle model, solid mechanics, numerical modelling, granular and discontinuous materials

AALTO-YLIOPISTO
INSINÖÖRITIETEIDEN KORKEAKOULU

DIPLOMITYÖN
TIIVISTELMÄ

Tekijä: Oskari Nihtilä

Työn nimi: Kontinuumin mallinnus diskreettielementtimenetelmällä

Päivämäärä: 11.9.2017 Kieli: Englanti Sivumäärä: 8+79

Sovelletun mekaniikan laitos

Professuuri: Teknillinen mekaniikka

Työn valvoja ja ohjaaja: Apulaisprof. Arttu Polojärvi

Kiteisiä, heterogeenisia ja epäjatkuvia materiaaleja, kuten merijäätä, voidaan mallintaa numeerisesti käyttäen diskreettielementtimenetelmää (DEM). Menetelmässä materiaali diskretoidaan käyttäen suurta määrää äärellisiä ja täysin jäykkiä partikkeleita. Materiaalin ollessa kuormituksessa partikkelit vuorovaikuttavat toistensa kanssa ennalta määrättyjen kontaktilakien mukaisesti. Mallinnettaessa materiaalin murtumista kontaktilait kuvataan partikkelien välisten sidosten avulla. Sidokset voivat murtua muodostaen mikrohalkeamia ja lopulta aiheuttaen materiaalin hajoamisen.

Tässä työssä kehitetään diskreettielementtimenetelmään perustuva malli, jonka tavoitteena on simuloida kiinteän aineen elastista käyttäytymistä kuormituksessa. Malli implementoidaan laskentaohjelmisto MATLABilla. Mallinnettava materiaali diskretoidaan pakkaamalla yhdenkokoisia jäykkiä palloja. Partikkelikoon ja diskretointimetodin vaikutusta tutkitaan käyttämällä viittä partikkelikokoa ja kolmea pakkaustapaa, jotka ovat yksinkertainen kuutiollinen pakkaus sekä heksagoninen ja satunnainen tiivispakkaus. Lisäksi malliin implementoidaan kaksi sidostyyppiä, jotka perustuvat joko lineaarisiin jousiin tai Timoshenko palkkeihin.

Mallia testattiin veto- ja puristuskokeilla sekä kolmipistetaivutuskokeilla. Simulaatioiden tulokset sekä satunnaisella (RCP) että heksagonisella (HCP) tiivispakkauksella diskretoiduilla koekappaleilla osoittavat, että materiaalin kimmokerroin kasvaa lineaarisesti huokoisuuden funktiona. Lisäksi RCP koekappaleiden Poissonin vakio konvergoituu kohti tiettyä arvoa partikkelikoon pienentyessä. Taivutuskokeet osoittavat, että materiaalin kimmokerroin taivutussuuntaan on alhaisempi kuin aksiaalisuuntaan riippumatta pakkaustyypistä. Tuloksista ei voida tehdä selkeitä johtopäätöksiä, että taivutusjäykkyys kasvaisi huokoisuuden pienentyessä.

Avainsanat: Numeerinen mallinnus, diskreettielementtimenetelmä, kiteiset ja epäjatkuvat materiaalit

Preface

This master's thesis was written in the ice mechanics research group at Aalto University School of Engineering. The work was funded through project "Arktisten rakenteiden jaakuormat: mallikokeista teollisuuden mittakaavaan (ARAJAA)" sponsored by Tekes - the Finnish Funding Agency for Innovation, Aker Arctic Technology Inc., ABB Marine, Arctia Shipping, Technip Offshore Finland Oy, Suomen Hyötytuuli Oy, Finnish Transport Agency and Ponvia Oy. The financial support is gratefully acknowledged.

I would like to express my deepest gratitude to my supervisor, Assistant Professor Arttu Polojärvi for his excellent guidance through this project. His ideas and comments were highly valuable and helped me through numerous issues encountered during the work. Furthermore, I wish to thank the whole ice mechanics research group for providing a supportive and pleasant working atmosphere. Especially, I would like to thank my friends Samuli Partanen, Unto Kujansuu and Ida Lemström for many interesting and inspiring conversations during lunch and coffee breaks.

Finally, I would like to extend my gratitude to my family and friends. The support and encouragement during my studies has been invaluable. Without you this thesis would not have been possible.

Otaniemi, 11.9.2017

Oskari Nihtilä

Contents

Symbols and abbreviations

Symbols

k_n, $\bar{k}_n$	normal spring stiffness
k_s, $\bar{k}_s$	shear spring stiffness
E	Young's modulus
G	shear modulus
ν	Poisson's ratio
r_p	radius of a particle
$\hat{C}_n$	average coordination number
N_p	number of particles
N_c	number of contacts
p	porosity
ρ	density
L	length
A	surface area
R_b	radius of a bond
I	moment of inertia
J	polar moment of inertia
F_i	force vector
M_i	moment vector
T_{ij}	coordinate transformation matrix
x_i	position vector of a particle
n_i	unit normal of the contact plane
t_i	unit tangent of the contact plane
u_i	displacement vector
v_i	velocity vector
a_i	acceleration vector
θ_i	angular orientation vector
ω_i	angular velocity vector
α_i	angular acceleration vector
e_{ijk}	permutation symbol
K_{ij}	stiffness matrix of a Timoshenko beam
Φ	Timoshenko shear coefficient
f_s	form factor of the cross section
Δt	time step
c	viscous damping coefficient
ξ	damping ratio
m, M_{ij}	mass, mass matrix
I_{ij}	inertia tensor
W	work
λ	eigenvalue
V	volume
σ_{ij}	stress tensor
δ_{ij}	Kronecker delta
δ	central deflection
f_b	natural frequency

Abbreviations

DEM	Discrete Element Method
BPM	Bonded Particle Model
FEM	Finite Element Method
FLAC	Fast Lagrangian Analysis of Continua
BSM	Bridging Scale Method
PB	Parallel Bond
HCP	Hexagonal Closepacking
RCP	Random Closepacking

1 Introduction

Understanding the mechanical behaviour of different materials is essential for designing efficient and safe structures and machines. The deformations and stresses under external loading together with the failure mechanisms of the designed structure need to be determined with good accuracy. Depending on the material and loading conditions, these behaviours vary significantly from linear elastic to nonlinear and from brittle to ductile behaviour.

Material modelling and solid mechanics analysis were for a long time based on experiments and derivation of theoretical models. Together with the development of computers, numerical methods have become more common in the analysis of solid mechanics problems. These numerical methods include amongst others the finite element methods (FEM), finite difference methods and discrete element methods (DEM). The finite element method is today the dominant tool in modelling continous materials both in the linear and nonlinear range of deformation. However, it has limitations when modelling macrocracks or fragmentation of the material (Potapov et al., 2016). This behaviour is important in the damage and failure of quasibrittle materials, such as ice, rock or concrete.

The discrete element method (DEM) is a completely discontinuous approach, which represents the material as a group of rigid particles or a lattice structure. The particle-based, or particulate, DEM can mimic the microstructure of granular materials when the particle length scale is related to the grain size (see Figure 1a). Thus, it allows studying phenomena at a microscale of the material. By assigning fracture criteria between individual particles, microcracks can be created in the material. The coalescence of microcracks lead to the formation of macroscopic cracks, which is an inherent property of the model. (Potyondy and Cundall, 2004)

In addition of producing realistic failure modes, DEM can also represent accurately the elastic behaviour of deformable structures. This is why DEM has become a widely used and accepted method of addressing engineering problems in granular and discontinuous materials. However, the method has not yet been extensively used to model failure of ice, and particularly the case of ice to ice contact. This study aims to be the first steps towards a long term objective of simulating breakage of ice with DEM. A particulate discrete element model, also referred to as bonded particle model, is developed with the goal to simulate the elastic behaviour of a continuum. The work is a part of the Aalto University research programme on Arctic technology and particularly ice mechanics.

1.1 Background

Discrete element methods (DEM) are numerical modelling methods that are commonly used to model granular, heterogeneous and discontinuous materials such as soil, rock or concrete. The term discrete element method usually refers to systems of finite rigid particles, but also lattice models can be considered as discrete element methods. In particle-based methods the material deformation is numerically solved using particle interaction laws and applying Newton's equation of motion on the

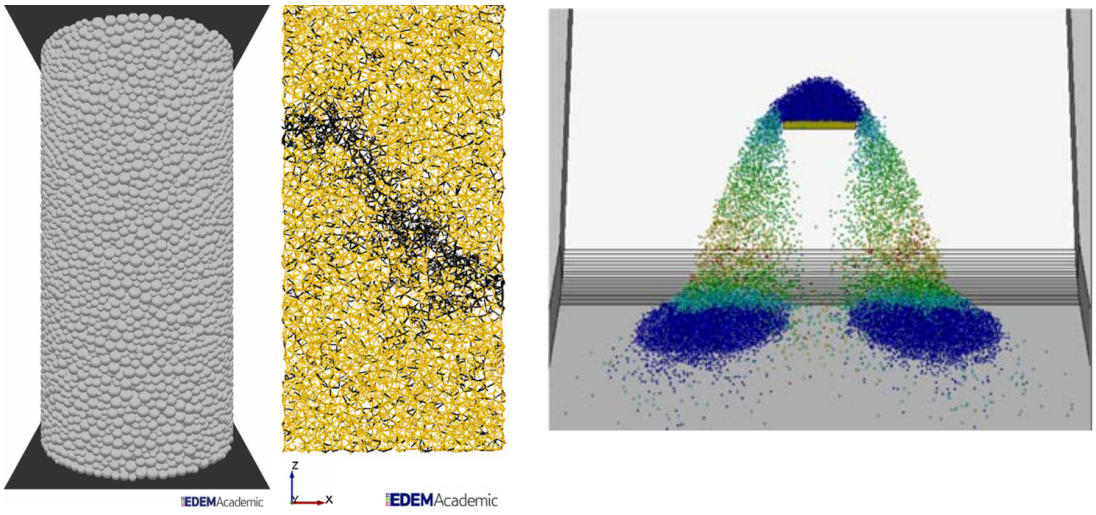

(a) (b)

Figure 1: Examples of DEM: (a) A cylindrical bonded particle specimen and the bond network after a uniaxial compression test. Black lines represent broken bonds. (Brown et al., 2014) (b) Modelling flow-obstacle interaction with a hard sphere granular flow model. Blue particles have zero velocity. (Teufelsbauer et al., 2009)

particles whereas, in lattice based methods there are no particles with discrete masses, and the displacements of the nodes are usually calculated by solving a set of elastic equations for beams or springs (Schlangen and Garboczi, 1996). Particulate DEM was first introduced by Cundall in 1971 and 1974 for the analysis of rock mechanics problems. Since then it has been used in a variety of fields, ranging from avalanche modelling to mining engineering.

Particulate DEM can be further divided into two categories called soft sphere and hard sphere models. These are illustrated in Figure 2. The models differ in terms of the way the particles are allowed to contact. In soft sphere models penetration, which is considered as particle deformation, is allowed. The hard sphere model does not allow penetration and they are the basis of the so-called "collisional" or "event driven" models. In these models, collisions are considered in the order in which they occur and only one collision can be analyzed at a discrete time. The particle velocities and trajectories are calculated based on the equations governing momentum exchange and the only energy dissipative factor is the coefficient of elastic restitution. These models are used in rapid granular flows such as avalanches or flows through pipes in industrial processes (see Figure 1b). (O'Sullivan, 2011)

Contrary to the name, the particles in soft sphere models are rigid and the elasticity of the material originates from the contact model. The particles can overlap, and the normal force between two particles is based on this overlap or separation if tensile force can be transmitted. Depending on the contact model, also shear forces and moments can be transmitted between contacting particles. The deformation of the material is governed by the displacements of individual particles in the model. The principle of obtaining the displacements, is to solve the dynamic equations of the linear and angular motion and calculate the incremental

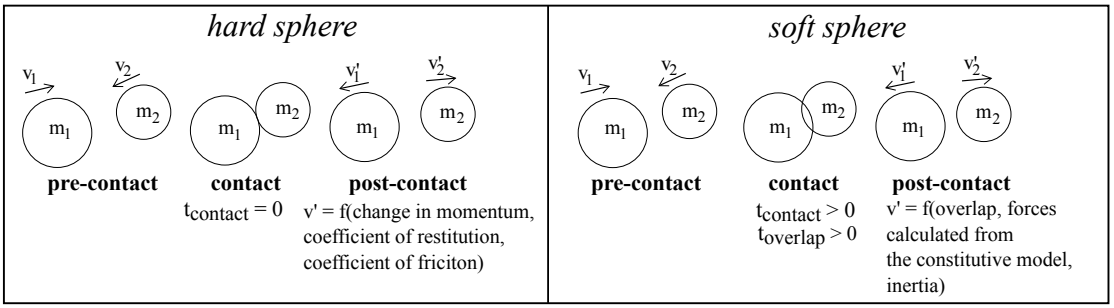

Figure 2: Main differences between the hard sphere and soft sphere models. The displacements in the soft sphere model are exaggerated. The particles can remain overlapped if the contact forces are in equilibrium. Symbols in the figure: m_1 and m_2 are the masses and v_1 and v_2 are the velocities of the particles, $t_{contact}$ and $t_{overlap}$ are the time of contact and time of overlap, respectively, and the superscript $'$ refers the values post-contact.

displacements in increments of discrete time. In contrast to the hard sphere approach, multiple contact forces are solved at each discrete time instant. (O'Sullivan, 2011)

The soft sphere approach can be used when modelling the elastic and failure behaviours of solid materials. In this work, the focus is on a special case of soft sphere particulate DEM where particles are bonded together with springs or beam elements (see Figure 1a). This method is called the bonded particle model (BPM). The first step in a BPM simulation is the generation of the particle coordinates, that define the sphere packing, defining the boundary conditions of the model. After specifying the model parameters, such as bond type, bond stiffness and strength, the simulation is started. The BPM simulation is a transient, or dynamic, process. In quasistatic simulations, this process approaches a state of equilibrium, in which the internal forces acting on particles are balanced. The initial packing of particles can be loaded by the motion of rigid walls or applying external loading to certain particles. These inputs cause disturbances that propagate in the particle assembly by means of particle displacements and interparticle forces. There are two basic calculation sequences that are conducted at discrete times and repeated between time steps (see Figure 3). First, the interparticle forces are calculated with a force-displacement law that depends on the bond type. After obtaining the resultant force for each particle, the incremental displacements and new particle positions are calculated by numerically integrating the Newton's second law. The time intergration in DEM simulation is commonly done with an explicit time integration scheme, such as the central difference method.

The direct results of a DEM simulation are particle properties, such as position, velocity and interparticle forces. Postprocessing procedures are required to obtain continuum-based quantities such as stress or strain. The stress in a particle packing has to be calculated as an average of the particle stresses as stresses cannot exist in the voids between particles. This can be done by integrating boundary forces or calculating stresses at a particle level and taking an average to obtain stresses inside

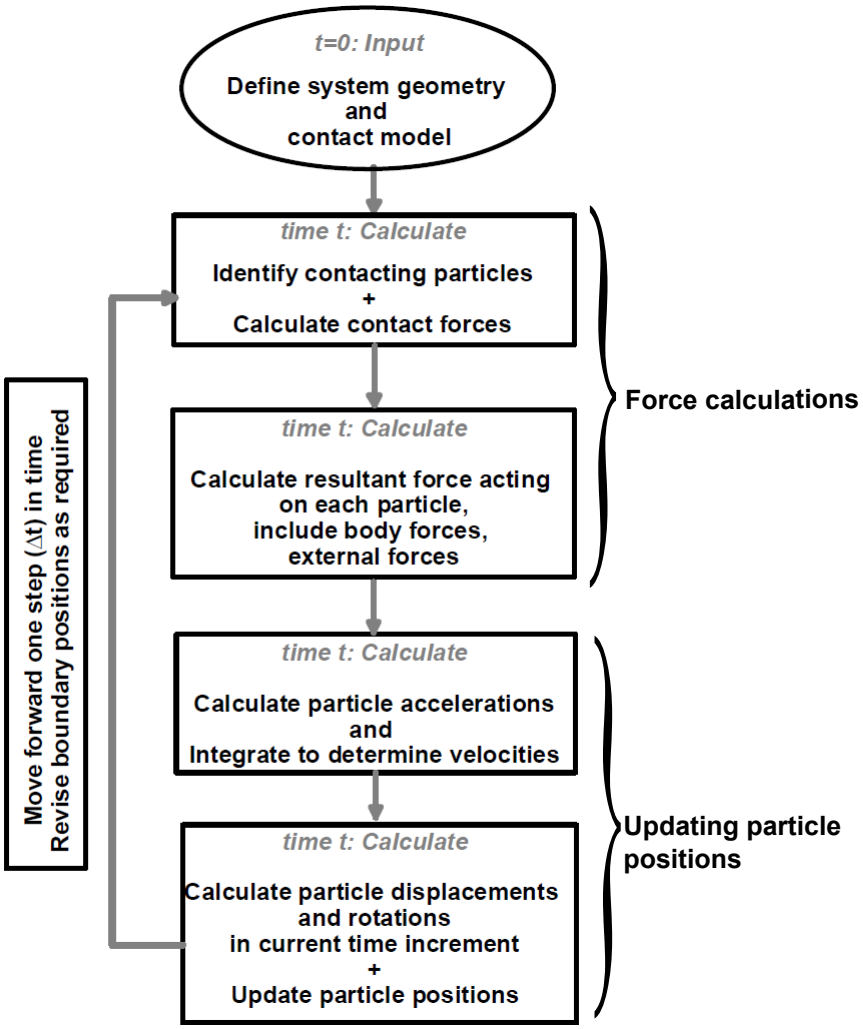

Figure 3: Calculation sequencies in a typical DEM simulation. (O'Sullivan, 2011)

a so-called representative volume element of several particles (Nemat-Nasser, 1999). Unlike stresses, strains cannot exist inside the particles since they are considered as rigid bodies. Similarly to stresses, a representative strain can be calculated from the boundary positions. In addition, the displacements of the particles can be used to fit a curve that can be differentiated to give the deformation gradient and further the strains in the specimen. (O'Sullivan, 2011)

1.2 Objective and scope

The main objective of this study is to develop a three-dimensional bonded particle model (BPM) using the numerical computing software MATLAB (MathWorks, 2017). It is studied how the discretized material behaves in the elastic region of uniaxial and flexural loading. This is done by determining the elastic constants, Young's Modulus and Poisson's ratio, and by studying the stress state inside a deformed material specimen. Two different bond models are implemented in the BPM. Bond

models based on both, linear springs or Timoshenko beams, are used.

Another objective is to study the parameter sensitivity of this model. The sensitivity study is conducted by studying the effects of varying simulation parameters such as particle size, initial packing of particles and the bond model. The three sphere packing methods used in this study are uniform or cubic packing, hexagonal closepacking and random closepacking.

The study is limited to the linear elastic deformation in axial and flexural loading, excluding the analysis of the dynamic and failure behaviour of the model. The interactions between particles are governed by the bond forces. As the bonds are not allowed to break, no contact forces are calculated during the simulations. Furthermore, the particle shape is restricted to spheres and only equally sized particles are considered in the packings.

1.3 Thesis structure

This thesis is divided into four sections. The first section includes a literature survey on previous studies in the field of modelling continuum with discrete element methods. The latter part of the section is arranged based on the different solid materials that have been modelled with DEM. In the second section the mechanics of the bonded particle model that is implemented in MATLAB are accurately described. This includes the main steps of the simulation, the bond modelling, particle kinematics and stress analysis. This section is followed by a description of the simulation setup for different loading cases. In the fourth section, the results of the simulations are presented and analyzed. The thesis is concluded with a summary of the analyzed results and proposals for future work.

2 Discrete element method in continuum modelling

Solid continuum can be modelled with discrete element methods by introducing bonds between initially contacting particles as illustrated in Figure 4. This so-called bonded particle model (BPM) has been further developed to model various materials such as rock, sea ice or fiber reinforced polymer composites. This chapter begins with the description of general features of bonded particle models which is followed by the presentation of previous research on the subject. The latter part of the chapter is structured according to material types that have been modelled using BPM.

2.1 General features of bonded particle models

One of the main features in a BPM is the bond model. Different types of bond models have been developed and they can be divided into two main categories, spring models and beam models. Both of these categories, together with different bond softening and failure criteria, have been succesfully used in bonded particle models. In the simplest BPM the initially contacting particles are bonded together by single linear springs acting between the centers of bonded particles and resisting only translation (Ergenzinger et al., 2011). In more advanced spring models, such as the parallel bond model, the bond is also able to transfer shear forces and moments. The beam models can be either based on Euler-Bernoulli theory, as in the model by André et al. (2012) or Timoshenko beam theory, as in the models by Brown et al. (2014) and Schneider et al. (2010).

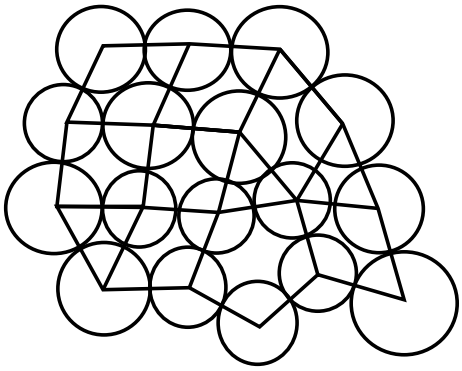

Figure 4: A 2D bonded particle assembly. Black lines represent bonds between contacting disk shaped particles.

Besides the bond model, BPMs can differ in particle shape, particle packing and the amount of dimensions in modelled specimen. Even though the modelled materials are nearly always three-dimensional, two-dimensional DEM studies tend to be more popular than 3D studies. The main advantage in the 2D simulation domain is the decrease in computational effort compared to a 3D domain. The particles have less degrees of freedom and less contacts in 2D simulations. This makes 2D simulations

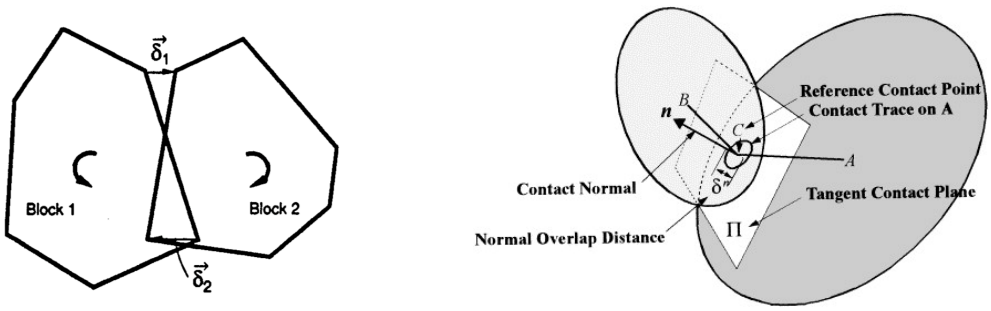

(a) (b)

Figure 5: (a) Polygon shaped particles used to model ice sheets by Hopkins (1992) (b) Overlapping ellipsoids and characteristics of the contact (Ouadfel and Rothenburg, 1999)

run faster than 3D simulations with equivalent amount of particles. (O'Sullivan, 2011)

The particle shape in DEM models is restricted to geometries that can be analytically described. The most common particle geometries used in DEM are disks in 2D and spheres in 3D. The reason for the popularity of these geometries is their simplicity. It is easy to identify contacting particles and the contact point accurately. Furthermore, the calculation of rotations is significantly simpler for spheres as there is no coupling with the translational degrees of freedom. Other types of geometries that are used in DEM simulations are ellipsoids, polygonal or polyhedral shapes and clusters of multiple spheres (see Figure 5). Polygonal particle shapes have been used widely for modelling ice floes and ice blocks. Particle clusters were developed to create more complex particle geometries while keeping the contact detection simple (see Figure 6a). These clusters can be composed of different sized spheres that touch or overlap each other. They are considered as rigid particles and no contact forces are calculated between the clustered spheres even if they overlap. Crushable agglomerates are a type of clustered particles in which contact forces inside the clusters are calculated and the clusters can fragment into smaller pieces. Clumped particles use the same logic as clusters with the difference of restricting rotations of individual particles as shown in Figure 6b. These clumps translate and rotate as one rigid particle and are able to fragment into smaller pieces. Cho et al. (2007) used clumped particles to reduce the particle rotations that were excessive compared to real rock grains.

The initial arrangement, or packing, of particles should attempt to correspond the structural properties of the simulated material (André et al., 2012). These properties can be isotropy, homogeneity, a certain packing density or initial stress state. Random number generation is most commonly used to generate initial coordinates for the particles. Random number generation can also be used to generate the particle size distribution when multiple particle sizes are used. This method leads initially to a low packing density "cloud" of usually non-contacting particles inside a predefined bounding box. There are different algorithms to increase the packing density and

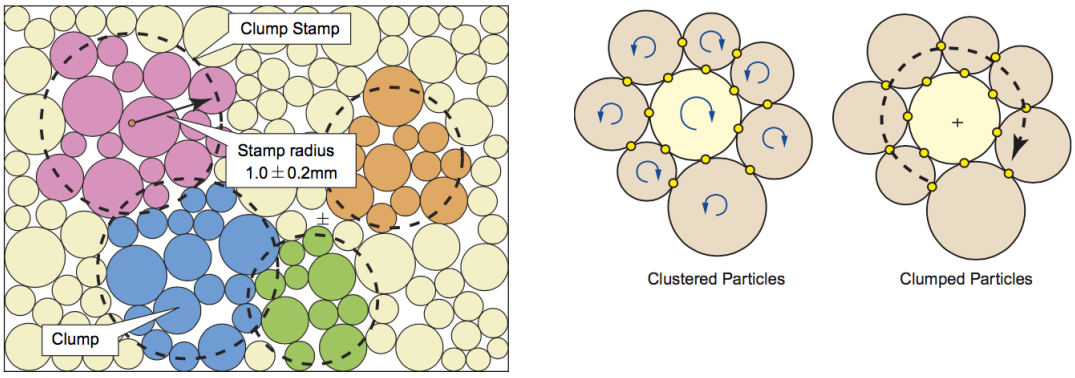

(a) (b)

Figure 6: (a) Example of a stamping logic to create and control the size of clumps. (b) The difference between clusters and clumps. (Cho et al., 2007)

obtain a desired coordination number, which is the number of contacts per particle (Potyondy and Cundall, 2004). The packing algorithms include dynamic methods such as radius expansion of hard spheres, isotropic compression with rigid walls or serial deposition of spheres under gravity (Bagi, 2005). In these dynamic methods, DEM calculation cycles are performed between particle expansion or deposition steps. One example of dynamic packing method is shown in Figure 11. Here, the initial "cloud" of particles is allowed to rearrange under zero friciton inside a rectangular material vessel. This is followed by expanding and moving particles with less than three contacts until a desired packing density is achieved. Another category is the so-called geometrical algorithms where the particle positions are adjusted with respect to geometrical relationships, namely the distances between sphere centers (Labra and Onate, 2009). Geometrical methods also include triangulation approaches where a triangular mesh is generated and particles are either added to the vertices or inside the triangles or tetrahedra (O'Sullivan, 2011). In this study, two regular sphere packing methods are used together with a dynamic random packing scheme. These are described in more details in chapter 4.1.

2.2 Determination of the interparticle spring stiffnesses

One major challenge in spring based bonded particle models is the determination of normal and shear spring stiffnesses and especially the ratio between these stiffnesses. For a general case of arbitrarily packed spheres of different size, these properties must be determined by means of a calibration process to obtain desired macroscopic properties for the material (Potyondy and Cundall, 2004). This process requires time as it has to repeated each time when the particle size is varied or a change in the macroscopic properties is needed. The calibration is usually done with a trial and error approach as in the quasistatic uniaxial compression/traction procedure proposed by Hentz et al. (2004). In the study, Hentz also used a strain energy criterion to scale the spring stiffness values and to obtain lower dispersion between the macroscopic Young's moduli for different random packings. The amount of

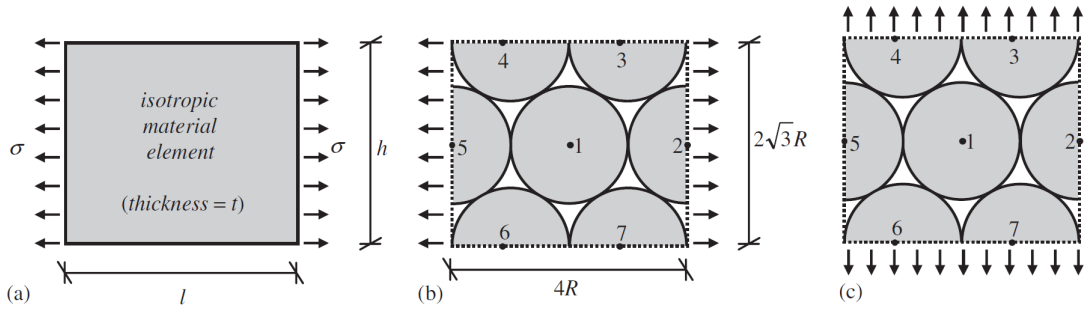

Figure 7: 2-dimensional hexagonal closepacked unit cell under uniaxial loading. (Tavarez and Plesha, 2007)

trials can be reduced by the means of dimensional analysis. Fakhimi and Villegas (2007) used the Buckingham π theorem to obtain relationships between dimensionless parameters and draw calibration curves. The curves were then used to select an appropriate normal to shear stiffness ratio, thus quickening the calibration process.

For certain regular packings such as hexagonal closepacking or face centered cubic packing, theoretical models for calculating the spring stiffnesses have been derived. The derivation has been done by considering a unit cell that is repeated in the packing. Tavarez and Plesha (2007) derived the relationship between the spring stiffnesses and macroscopic elastic parameters for a 2-dimensional hexagonal closepcaking (see. Figure 7). The constitutive equation with the stiffness matrix was formed for the unit cell of 7 nodes and 14 degrees of freedom. By taking into account uniform straining and symmetry of the cell, the relevant displacements could be reduced to the horizontal displacement of node 1 and vertical displacement of node 3, thus giving a problem with two variables and two equations. The following plain stress relationships for the normal and shear spring stiffnesses were obtained

$$k^n = \frac{1}{\sqrt{3}(1-\nu)}Et, \quad k^s = \frac{1-3\nu}{\sqrt{3}(1-\nu^2)}Et, \tag{1}$$

where k^n and k^s are normal and shear spring stiffnesses, respectively, E is the macroscopic Young's modulus, ν is the Poisson's ratio and t is the thickness of the material sample.

Wang and Mora (2008) derived the same relationships for a 3D hexagonal closepacking. The derivation was based on comparing the discrete element model and a corresponding continuum. The continuum model and discrete element model were deformed with equal displacements and the strain energy stored in a unit cell of the hexagonal closepacking (see. Figure 8) was assumed to equal the strain energy stored in a unit cell of the continuum. The strain energy in the HCP-cell was calculated as a sum over all springs. Contrary to the 2D derivation by Tavarez and Plesha (2007), the particle rotations were also taken into account when calculating the shear components in the strain energy. With the relation between the strain energies of the continuum and spring assembly, they were able to write the stiffness matrix in the constitutive stress-strain equation as a function of spring stiffnesses. In this way,

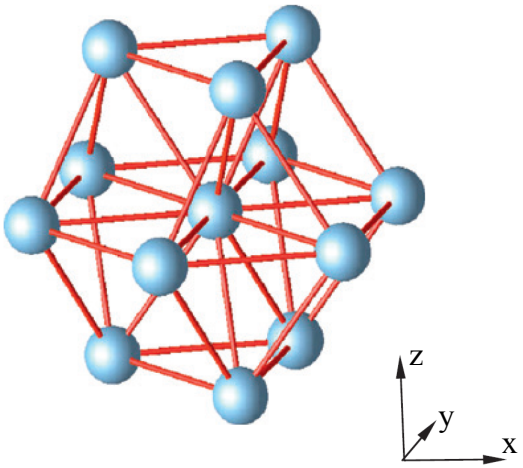

Figure 8: A unit cell of the 3D hexagonal closepacking. The discrete particles (blue spheres) are not contacting each other to better illustrate the geometry. (Wang and Mora, 2008)

the following equations for macroscopic Young's modulus as a function of spring stiffnesses were obtained

$$E_x = E_y = \frac{3\sqrt{2}k^n(k^n + k^s)[3(k^n)^2 + 23(k^s)^2 + 22k^n k^s]}{r_p[18(k^n)^3 + 119(k^n)^2 k^s + 128k^n(k^s)^2 + 23(k^s)^3]}, \tag{2}$$

and

$$E_z = \frac{3\sqrt{2}k^n(k^n + k^s)}{r_p(5k^n + k^s)}. \tag{3}$$

2.3 Modelling elastic continuums with DEM

Although DEM is primarily used to model heterogenous and discontinuous materials, also the mechanical behaviour of homogeneous, isotropic and perfectly elastic materials has been simulated with DEM. Fused silica has been modelled with a 3D spherical BPM model with cohesive beams acting as bonds (André et al., 2012). In this study, cylindrical Euler-Bernoulli beams were introduced between touching particles. The beam ends were fixed to the particle centers and they were considered mass-less in the simulations. In order to calculate the beam deformations after each time step, the global position and orientation of the randomly packed particles were stored.

The microscopic beam properties were calibrated using a numerical quasi-static uniaxial tensile test. First a microscopic radius ratio (ratio between the beam and the average particle radius) was calibrated so that the macroscopic Poisson's ratio corresponded to the one of silica. The result was used to calibrate the microscopic Young's modulus. After calibration numerical samples of silica were tested under tension, bending and torsion. Both quasi-static and dynamic tests were conducted for

the cylindrical specimens. The dynamic tests inlcuded the determination of natural frequencies and the mechanical wave celerity. The results showed good quantitative agreement with analytical strength of material solutions.

The parallel bond model has also been used to conduct tensile test simulations of high carbon steel. In this work, Chen et al. (2016) focused on studying the relationships between DEM parameters, such as particle and bond sizes and the macroscopic properties, such as Young's modulus, ultimate stress and elongation at fracture. Chen et al. (2016) concluded that the particle size and bond size can significantly affect the macroscopic mechanical properties. He argued that the reason was mainly due to the effect that the particle and bond sizes have on the amount or volume of bonds in the specimen.

2.4 Combined discrete element and continuum modelling

Discrete element methods have been coupled with finite element methods to overcome the limitations of FEM in modelling large material deformations and material discontinuities (Potapov et al., 2016). This is the case with concrete and especially in advanced damage states. Potapov combined these two methods in a study of modelling concrete structures reinforced with steel bars (see Figure 9). The concrete was modelled with a conventional DEM based on the work of Hentz et al. (2004). The reinforcing steel bars were modelled with beam-like FEM elements and a steel concrete bond model was developed to appropriately link the DEM particles and beam elements. The links were formed between concrete particles and steel bar nodes having an orthogonal distance inside a predefined interaction limit. The normal and shear force, carried by the two non-linear springs of the link, were independent of each other. These spring forces were then distributed to the finite element nodes in a logical manner depending on the orthogonal projection point of the DEM particle. Two test schemes were conducted to demonstrate the capabilities of the model. First a steel-concrete tie, with one horizontal steel bar, was tested in tension. A realistic distribution of force and damage along the tie was obtained. Secondly a low velocity hard impact test was conducted on a beam with four reinforcing steel bars. The obtained crack pattern and deflection were close to experimental results and the amount of dissipated energy corresponded well to the energy released from the impactor (see Figure 9).

Using DEM to model large structures with a great number of particles requires a lot of computation and can be very time consuming. However, in many cases the studied phenomena is localized in a small part of the model. In these cases it is advantageous to use a coupled discrete and continuum model. Potyondy and Cundall (2004) modelled the excavation of a circular tunnel with a coupled 2D BPM (PFC2D software) and finite difference method (FLAC software). In the finite difference method, the continuum is discretized with a grid and the partial differential equations, governing the deformations, are solved in the grid nodes by approximating the derivatives with finite differences. A portion of the tunnel edge was modelled with BPM and a FLAC grid was used to model rest of the domain and to control the velocities of a layer of boundary particles (see Figure 10). The excavation was

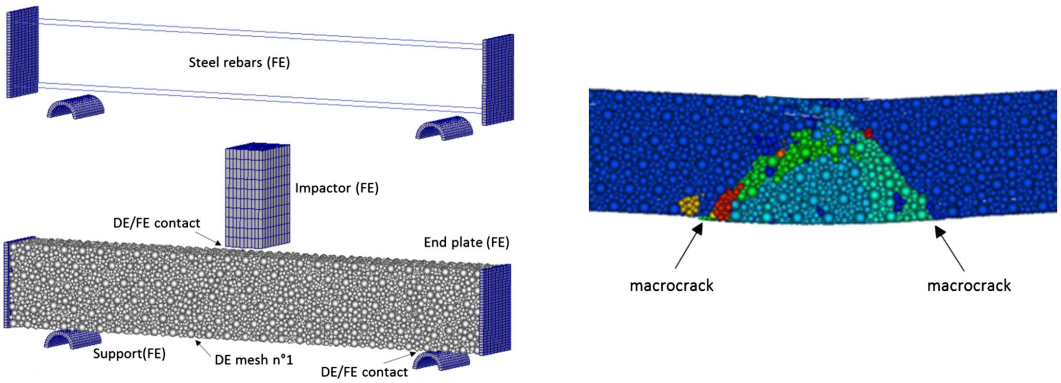

Figure 9: Coupled DEM-FEM model by Potapov et al. (2016). Concrete is modelled with DEM and reinforcing steel bars together with end plates, supports and the impactor are modelled with FEM. The impact test creates a shear plug similar to experimentally obtained failure types.

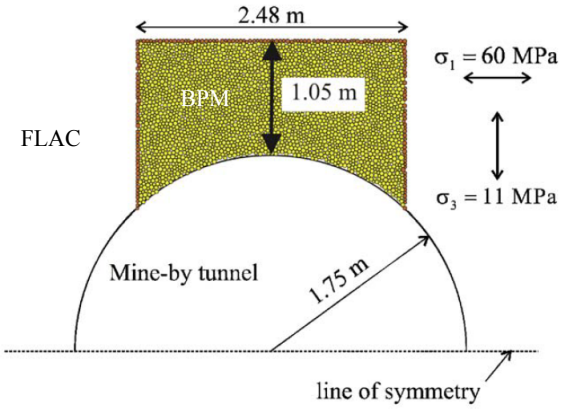

Figure 10: Modelling excavation of a tunnel with a coupled BPM and finite difference model FLAC. Only the potential damage region was modelled with BPM. The FLAC boundaries were at a distance of 10 times the tunnel radius.

then simulated by applying stresses on the outer edges of the FLAC grid and the damage-formation process was investigated in the BPM domain.

Another way of coupling DEM and a continuum method is a bridging scale method (BSM) initially proposed by Wagner and Liu (2003) for computational analysis in nano-material mechanics. The idea was to concurrently couple atomistic and continuum simulations. The displacement field of the material was decomposed into coarse and fine scale. The coarse scale displacements were solved from the finite element nodal displacements. The fine scale then describes the part of the DEM displacements that the coarse scale cannot represent. Li and Wan (2011) developed a BSM for granular materials that combined DEM and a Cosserat continuum based FEM. In this study Li and Wan particularly considered the interfacial condition between the DEM and FEM domains by applying a non-reflecting boundary condition. This was done to avoid spurious reflection of waves generated in the DEM region.

2.5 Modelling rock with DEM

Rock is a heterogenous material that can be modelled as cemented grains. For sedimentary rock such as sandstone this approximation is good as there is a true cement present between the grains. For crystalline rocks, such as granite, this cement can be seen as interlocking between the grains. The mechanical behaviour of rock is then controlled by the force chain fabric that is created between interacting grains and cement. The force chain fabric can be seen as a skeleton of force chains that propagate form one grain to the adjacent grain under a macroscopic load. (Potyondy and Cundall, 2004)

Blocky rock mass and sand was one of the first application of DEM. Cundall and Strack (1979) developed the first DEM computer program called BALL in the early 1970's with a goal to model this kind of granular assemblies. The program was able to simulate the loading of two-dimensional assemblies of disks. No bonds were introduced between the disk shaped particles and the particles would experience forces only when overlapping each other. The model was verified by comparing the numerically obtained contact force plots of a biaxial compression test to corresponding force plots obtained experimentally with photoelastic disks. (Cundall and Strack, 1979)

A more advanced DEM model for rock was developed by Potyondy and Cundall in 2004. This model was called the bonded particle model (BPM) and the term has since been used commonly for DEM models with initially bonded contacts. In this method, rock is modelled as a cemented granular material. The grains are described as non-uniform sized rigid disks or spheres depending on the simulation domain, which is either two- or three dimensional. The mechanical behaviour of the cemented bonds is modelled by elements called parallel bonds. The parallel bond is introduced as two sets, normal and shear, of linear parallel springs between two rigid elements. This spring assembly can transfer normal and shear loads and moments in the directions of torsion and bending. The parallel bond has a finite size and the bond area is specified using a parallel bond radius multiplier alpha. This parameter defines the thickness of the bonds shown in Figure 4 and can be physically related to the amount of cement between particles.

The model also takes into account pure grain to grain contacts as the parallel bonds may break during the simulation. The forces acting on the contact point due to this contact depend on the relative motion of the two particles and the grain microproperties such as normal and shear stiffness and the friction coefficient.

Damage of the material, meaning the formation, growth and coalescence of microcracks, is represented as broken parallel bonds. The maximum stresses in a parallel bond is calculated using beam theory equations for normal and shear stresses. If the stresses exceed critical normal or shear strengths the parallel bond is removed and a microcrack is formed in the material.

Potyondy and Cundall (2004) state in their work that the bonded particle model has many advantages compared to conventional continuum methods for modelling rock. BPM can simulate damage and its progression without any empirical relations to define the changes in the macroscopic material properties. It also produces a

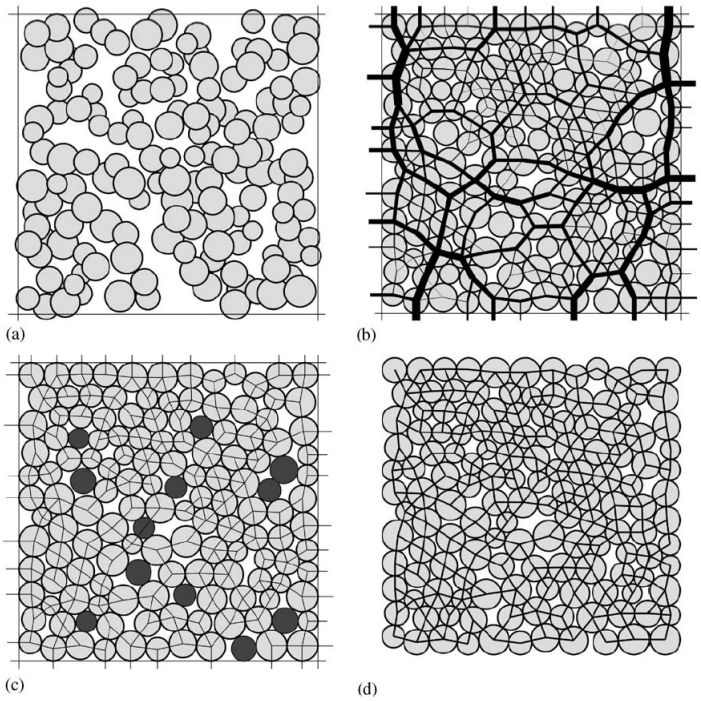

Figure 11: The sphere packing generation used by Potyondy: (a) Initial particle cloud, (b) force chains after rearrangement of particles under zero friction, (c) floater particles with less than 3 contacts: these particles are expanded and moved until they have a sufficient amount of contacts, (d) parallel bond network. (Potyondy and Cundall, 2004)

continuously non-linear stress-strain response that is specific to rock. These properties are emergent features of the model and arise from the microproperties of single bonds and particles.

The main limitations of the BPM in rock modelling are the overestimation of the tensile strength and underestimation of triaxial strengths when the model is calibrated to the uniaxial compression. More recent studies show that these deficiencies are significantly reduced if a clumped-particle geometry is used (Cho et al., 2007). In this study, Cho used different sized clumped particles of glued polydisperse spheres. These clumped particles units acted as one irregular shaped rigid particle in both translations and rotations. In this way the problem of excessive rotations with spherical particles was avoided (O'Sullivan, 2011).

2.6 Modelling composite materials with DEM

Similarly to rock and concrete, composite materials such as fiber reinforced polymers, are heterogenous and have both geometrical and parametric discontinuities. This is why the use of DEM, as a mean to model composite materials, has been studied recently (Yang et al., 2011; Khattak and Khattab, 2013; Wolff et al., 2013).

A usual failure mode for fiber reinforced polymers is the delamination between the fibers and the matrix material or between two laminated plies. Yang et al. (2011)

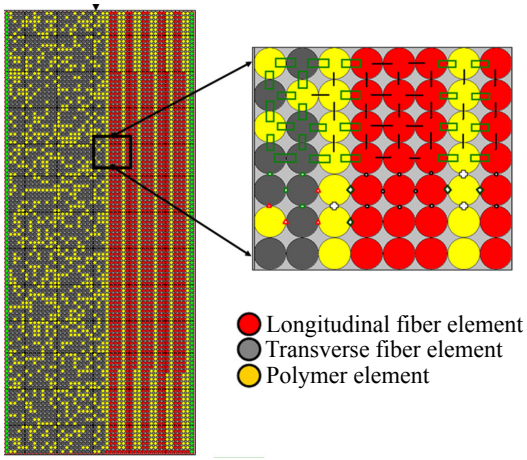

Figure 12: A part of the carbon fiber composite model by Khattak and Khattab (2013). The green box represents a parallel bond and the black line a contact bond. Other symbols between elements describe the different stiffness models.

used 2D DEM to study the progression of delamination in a laminated composite material. A beam specimen was created from two plies which were discretized using equally sized disks. The earlier mentioned parallel bond model was used to model the mechanical behaviour of individual plies. The interface bonds, where delamination takes place, were modelled with a contact softening model. These bonds remained linear elastic until the tensile or shear strength was reached and a linear softening model was applied. The softening model effectively dissipated the fracture energy generated in the breaking process of bonds. When a maximum plastic displacement, related to the fracture energy release rate, was reached the bond was removed and the crack grew.

Khattak modelled the tensile response of a carbon fiber reinforced polymer composite with DEM coupled with high resolution imaging. The polymer and fibers were modelled as clusters of circular DEM particles as shown in Figure 12. The shape and distribution of the polymer and fibers were obtained from a color-coded image of the composite cross section. Circular 2D discrete elements were assigned for a unit cell with areas occupied by longitudinal fibers, transverse fibers or polymer matrix. Parallel bonds were used to model thin polymer coatings around fibers and a simpler contact bond model was used to act between polymer elements. Additionally, a contact stiffness and slip model was activated when particles were compressed against each other. Different contact and bond stiffness were used depending on the contacting particles. These stiffness values were obtained with a calibration scheme, in which virtual tensile tests were conducted individually for each element type. A specimen of approximately 5500 particles was then constructed and loaded in a uniaxial tensile test. As a result of the study, the DEM model gave slightly higher ultimate tensile strength and Young's modulus values than an experimental study conducted before. However, these values were inside the standard deviation of the experimental values.

Wolff modelled a ceramic-polymer composite material using the earlier mentioned

parallel bond model together with the Hertz-Mindlin-Tsuji contact model, described e.g. by Fries et al. (2011). The ceramic material was modelled as rigid spheres and the parallel bond acted as the polymer binding the ceramic particles together. The Hertz-Mindlin-Tsuji contact model was used to calculate the linear elastic contact between two overlapping spheres. The Hertzian contact theory was used to calculate the normal force and stiffness and the tangential constitutive equation was based on the work by Mindlin and Tsuji (Tsuji et al., 1992). The model was validated by constructing a beam of 9500 discrete spheres and conducting three- and four-point flexural tests with different loading speeds and loading pin distances.

2.7 Numerical modelling of sea ice

Sea ice is a quasibrittle heterogenous material with a discontinous microstructure. In addition of solid ice grains, there are brine and gas pockets and solid salt inclusions in sea ice. The microstructure of sea ice depends both on the conditions during ice formation and the history of the environment, such as loading and temperature. The two main types of microstructure are granular and columnar ice. Granular ice is formed by deposition and consolidation of snow on an initial thin ice sheet formed on standing water. Frazil ice with a ganular micostructure is formed in fast moving rivers or windy areas of standing water when the temperature is very low. Granular ice is usually isotropic in macroscale which means that the ice properties do not vary in different directions.

Columnar ice is formed at sea surface when the conditions are calm or beneath a thin initial frazil layer. The columnar ice crystals can grow through the entire ice thickness while the growth direction is parallel to the, usually vertical, heat flow direction. The c-axis of columnar sea ice crystals lies in the horizontal plane. It's direction in the plane can be random leading to isotropic properties in the horizontal plane. The crystal c-axis can also be aligned in one direction. In this case ice is significantly weaker in the direction perpendicular to the c-axis, as the planes of brine inclusions inside crystals are oriented in the same direction.

Because of the heterogenous microstructure the failure of sea is a complicated process that depends highly on the loading condition. Sea ice may fail in a number of modes. Flexural failure can occur in ice ridge formation and bending of ice under icebreaking vessels or against conical offshore structures. Compressive or multi-axial failure can occur in similar situations. Ice can fail under high pressure during ridge formation or it can be crushed against vertical structures. Fracturing of ice has been studied both in laboratory and field conditions.

An extensive review on the mechanical properties of sea ice has been written by Timco and Weeks (2010). They suggest that the strength properties differ significantly between the vertical growth direction of columnar ice and horizontal direction. Tensile strength is about three times higher and compressive strength about four times higher in the direction of the columns. Compressive strength also depends highly on the strain rate. The strength increases as strain rate increases until the onset of the "ductile-to-brittle" transition is achieved. In the brittle zone the ice sample breaks into small pieces in a catastrophic manner. In tensile or flexural failure there is no

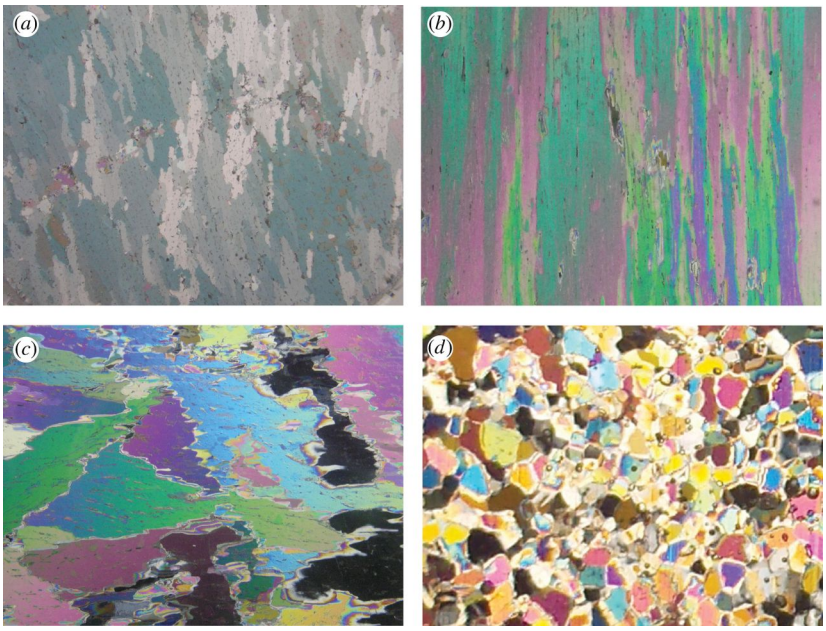

Figure 13: Different sea ice microstructures: (a,b) columnar sea ice from Antarctica, (c) platelet ice from the Ross Sea, (d) granular ice from the Bellingshausen sea. (Gully et al., 2015)

strong dependence on the loading rate.

Multi-axial loading tests have been performed to obtain the whole failure envelope of several ice types, meaning all the combinations of compressive and tensile stresses when ice starts to yield. These tests are usually done by loading in one direction and confining the sample in other directions. The confinement pressure is shown to have an effect on both the failure stress and failure mode. When the sample is loaded parallel to the columnar direction the failure mode changes when the confining pressure is increased. With no confinement there is axial splitting along the columns. Coulombic shear failure in an inclined plane occurs with moderate confinement and finally horizontal splitting across the columns occurs with high confinement. (Timco and Weeks, 2010)

DEM has not yet been extensively used to model fracture of ice. A few studies, treating ice at a larger scale (floes or fragments with sizes from 0.2-1200 meters), have been conducted (Jirásek and Bažant, 1995; Selvadurai and Sepehr, 1999; Paavilainen et al., 2011). Most of these studies are two dimensional, viewing ice sheets either from the side or top perspective.

Jirazek and Bazant (1995) studied the use of DEM in quasibrittle fracture of large ice floes (from 100 x 100 m to 1200 x 1200 m). They developed a 2D bonded particle model with both regular and random lattice structures. In the regular lattice the ice floe was modelled using a unit cell repeated regularly in a square pattern (see Figure 14). The square unit cell consisted of four corner particles that were connected by primary links and diagonal links crossing the square. The size of the particles were chosen to match the average distance between large-scale inhomogneities, such as thermal cracks, in sea ice. These links acted as linear springs with a linear softening

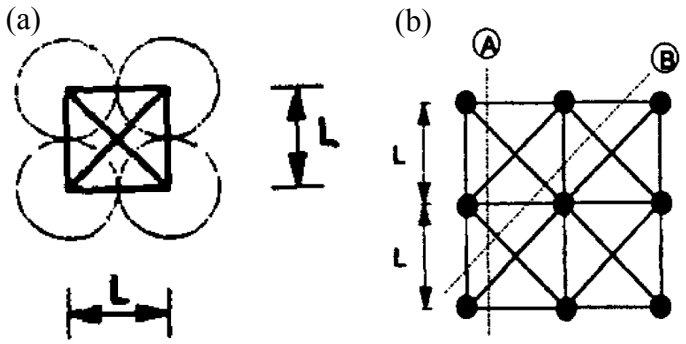

Figure 14: The 2D DEM model of Jirásek and Bažant (1995) (a) The unit cell of four particles connected by primary and diagonal links. (b) The fracture energy needed to break links along lines A and B were calibrated to equal each other in order to reduce the directional bias in crack growth.

after a certain tensile threshold force was achieved. The compressive behaviour of the links was brittle. The spring stiffness values were derived using the relation between the strain energy of a unit cell and that of an equally deformed continuum square. In addition, the directional bias of the crack growth was minimized by calibrating the fracture energy per unit link length to match in the principal and diagonal directions as illustrated in Figure 14. The random lattice was generated with a uniform probability density over the floe area and the links were formed between particles closer to each other than a maximum interaction distance. (Jirásek and Bažant, 1995)

In the simulations of Jirásek and Bažant (1995), a large ice floe with the size ranging from 400 to 57600 particles with one particle representing 25 m^2 of the floe surface, hit an cylindrical obstacle with a velocity of 1 m/s. As result of the simulation the contact force and crack patterns were recorded. The crack pattern of the regular lattice had a strong directional bias and did not represent fracture behaviour of an isotropic material realistically. However, the random particle method approximated the fracture properties well. The cracking patterns were realistic and the strain-softening behaviour of quasibrittle materials was reproduced. (Jirásek and Bažant, 1995)

Selvadurai and Sepehr (1999) used DEM to model the interaction of a 2D level ice sheet and a flexible stationary vertical structure. The level ice sheet was modelled as an elastic-viscoplastic material. In the model the ice was initially intact and it fragmented into smaller pieces during the interaction (see Figure 15a). Two fragmentation initiation criteria were used. For compression the Mohr-Coulomb criterion was used and for tension the fragmentation was initiated when the minimum principal stress reached the tensial strength of the material. The inclination of the fracture plane and thus the shape of the fragment was governed by the principal stresses and the angle of internal friction. The viscoplastic constitutive behaviour was taken into account when both principal stresses were purely compressive and the Mohr-Coulomb criterion was attained. In this case a viscoplastic flow region is

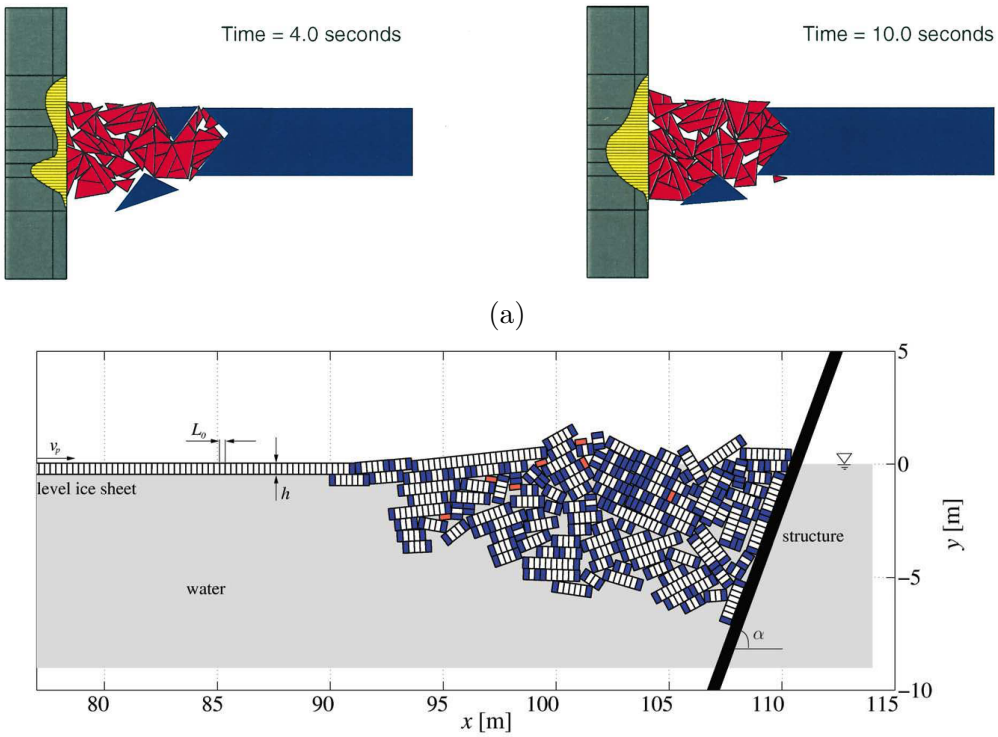

Figure 15: Different methods of modelling interaction between ice floes and a rigid structure: (a) Model by Selvadurai and Sepehr (1999) were fragmentation is governed by the direction of principal stresses. (b) Model by Paavilainen et al. (2011) were fragmentation is governed by a cohesive crack model applied to a Timoshenko beam connecting discrete elements.

developed in the material instead of brittle fracture. The intact ice sheet was meshed with either four-noded quadrilateral or three-noded triangular solid two-dimensional plane elements, in which the stress state was evaluated. The model also accounted for size-dependency of the strength of polycrystalline materials such as ice. The tensile strength was increased as the edge length of the fragment decreased until a limit value of 0.2 m was achieved. In the simulations, the average contact stress at the ice-structure interaction was measured. The time-dependent average contact stress exhibited a behaviour of accumulation and shedding, which is typically observed in ice-structure interaction. (Selvadurai and Sepehr, 1999)

Paavilainen et al. (2011) used a combined discrete-finite element model to study the ice loads generated during the rubbling process of ice sheets. A non-linear Timoshenko beam model was used to simulate the stresses and deformations of intact ice sheets and ice blocks broken from the initial sheet (see Figure 15b). The finite element nodes corresponded to the centroids of the discrete elements. In this way the deformation and stress state of the beam was governed by the motion of the discrete elements. The fracture of the ice sheet was modelled with the cohesive crack model. The model assumes that a crack is initiated when the stress exceeds a critical value and after initiation the stress transferred through the crack depends on the crack

opening displacement. The interaction between the separated ice blocks and the inclined wall that formed the rubble pile, was then modelled with two-dimensional DEM.

Recently, a DEM study on modelling sea ice using smaller spherical particles of 16-20 mm in diameter, was conducted by Ji et al. (2016). In this study, the 20 to 50 cm long ice specimens were discretized by packing spheres in a hexagonal closepacking pattern. The parallel bond model was used to model the interaction between contacting particles. A failure criteria based on the beam theory was used together with a linear softening law to model the fracture of bonds. Two simulated specimens of 375 and 1075 particles were generated for compressive and flexural testing, respectively. The focus in this study was to examine the influence of microproperties such as bond strength and coefficient of friction to the macroscopic failure characteristics. The macrscopic strength was found to be directly proportional to the bond strength and similarly increasing the coefficient of friction increased linearly the macroscopic compressive strength. However, the cofficient of friction had no effect on the macroscopic flexural strength. (Ji et al., 2016)

3 Mechanics of the bonded particle model

This section presents the principles of the bonded particle model (BPM) that is implemented as a MATLAB script in this work (see Appendix A). First, the main steps of the algorithm are described. Next, the bond mechanics and particle kinematics are explained in more details. The energy components of the system and the conservation of energy are discussed and lastly, a method for obtaining the stresses inside the specimen is described.

3.1 Main steps of a BPM simulation

Before starting the simulation, the model is initialized. This means that the sphere packing is generated and one contact detection cycle is performed to find out contacting spheres. The contacts are detected by comparing distances between sphere centroids. Next the bonds are generated between contacting spheres and a list of bonded sphere pairs is stored. After these steps the simulation is started and the following two steps are executed repeatedly:

1. **Calculation of bond forces.** The contact forces are calculated in an incremental manner based on the current velocities of the particles with respect to each other. This thesis studies two different bond models, the parallel bond model and Timoshenko beam model.

2. **Updating particle positions.** An explicit time integration method is used to solve the displacements of particles during one time increment. The acceleration of each particle is solved from the Newton's second law. In this study, the position Verlet time integration scheme is used to determine the positions of the particles at the end of one time increment.

The simulation is terminated when a predefined time limit is achieved. In this study, no contact detection is needed during the iteration loop as the bonds have no failure criteria at this stage of the model development. Therefore, no new bonds or contacts are generated or old bonds deleted during the simulation.

3.2 Bond modelling

The modelling of interactions between particles is an essential part of discrete element methods. In this thesis, the interactions are modelled by springs or Timoshenko beam elements acting as bonds between particles. The spring model used in this work is the called parallel bond model and it is described in chapter 3.2.2. Depending on the sphere packing method, the bonds can be oriented irregularly inside the specimen. Therefore, local coordinate systems are used and stored for each bond and coordinate transformations are needed between the global and local coordinate systems (see Figure 16).

3.2.1 Coordinate transformations

The transition from global to local coordinates is done by multiplying the variable in vector form with a transformation matrix T_{ij}. The transformation matrix consists of nine directional cosines representing the angles between the six basis vectors of the global (x_i, y_i, z_i) and local $(\hat{x}_i, \hat{y}_i, \hat{z}_i)$ coordinate systems. The matrix is given by

$$T_{ij} = \begin{bmatrix} \hat{x}_x & \hat{x}_y & \hat{x}_z \\ \hat{y}_x & \hat{y}_y & \hat{y}_z \\ \hat{z}_x & \hat{z}_y & \hat{z}_z \end{bmatrix} = \begin{bmatrix} \hat{x}_i \\ \hat{y}_i \\ \hat{z}_i \end{bmatrix}, \tag{4}$$

As figure 16 illustrates the local $\hat{x}$-axis follows the bond centerline joining the particle centroids. It is given by

$$\hat{x}_i = \frac{x_i^{(B)} - x_i^{(A)}}{L_b}, \tag{5}$$

where $x_i^{(A)}$ and $x_i^{(B)}$ are the position vectors in the global coordinates of particles A and B respectively. The vector $\hat{x}_i$ is normalized by dividing with the bond length L_b.

The normalized local y-axis is given by the cross product of the local x-axis vector and a unit vector into the direction of the global z-axis as

$$\hat{y}_i = \frac{e_{ijk}\hat{x}_i z_i}{||e_{ijk}\hat{x}_i z_i||}, \tag{6}$$

In the case $\hat{x}_i$ and z_i are collinear the previous equation cannot be solved and the local y-axis is defined as

$$\hat{y}_i = \begin{bmatrix} 0 & 1 & 0 \end{bmatrix}^T, \tag{7}$$

Knowing the vectors into the direction of local x- and y-axis, the z-axis can be obtained as a cross product of these two vectors.

$$\hat{z}_i = \frac{e_{ijk}\hat{x}_i \hat{y}_i}{||e_{ijk}\hat{x}_i \hat{y}_i||}, \tag{8}$$

In the Timoshenko beam model, the transformation between global and local coordinates is done twice during one time step. First, the displacements are brought to local coordinates and after applying Equation 23 the force increments have to be transformed back to the global coordinates before they are added to the resultant force or moment vector of the particle. In the parallel bond model this is not necessary as the all the displacement and force increment vectors are written in the global coordinate system. The local coordinate system is only used to define the contact plane in the parallel bond model.

3.2.2 Parallel bond model

The parallel bond can be described as a group of elastic springs distributed uniformly between the contacting particles (Potyondy and Cundall, 2004). In Figure 17 the parallel bond is drawn as two springs working in parallel with the contact spring

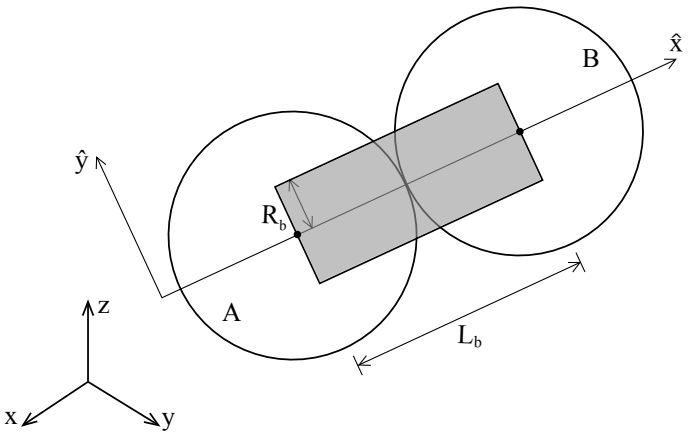

Figure 16: A bond joining a randomly oriented particle pair (A and B). L_b is the length of the bond and R_b is the radius of the bond. The global coordinate system is shown in the left bottom corner.

resisting only overlap of spheres. The values related to the parallel bond are hereby marked with a superscript pb and the values related to the contact spring are marked with a superscript c. The parallel bond, illustrated by the two pairs of springs, has a finite size and its cross sectional area is circular. The area is given by

$$A^{pb} = \pi R_b^2, \tag{9}$$

where R_b is the bond radius that is given by $R_b = \alpha r_{min}$, where r_{min} is the radius of the smaller contacting particle and α is the parallel bond radius multiplier that can get values from $0 \leq \alpha \leq 1$. When α is 0 the springs are inactive and they cannot transfer loads. In this work a multiplier of 1 is used for all the bonds.

The forces carried by parallel bonds are calculated in an incremental fashion starting from the beginning of the simulation when the forces are set to zero. As relative displacements occur between particles the incremental bond forces between time steps of the simulation are calculated from (see Figure 17)

$$\Delta F_i^{n(pb)} = \bar{k}^n A^{pb} \Delta u_i^n, \tag{10}$$

$$\Delta F_i^{s(pb)} = \bar{k}^s A^{pb} \Delta u_i^s, \tag{11}$$

where ΔF_i^n and ΔF_i^s are the normal and tangential force increments with respect to the contact plane and Δu_i^n and Δu_i^n are the normal and shear components of the displacement increment, respectively. The force increments in Equations 10 and 11 represent the action of the bond on particle A. The forces acting on particle B are of the same magnitude but in opposite direction. As shown in Figure 17 the parameters $\bar{k}^n$ and $\bar{k}^s$ are the bond normal and shear stiffness respectively and in the case of parallel bonds their units are given in stress/displacement or Pa/m.

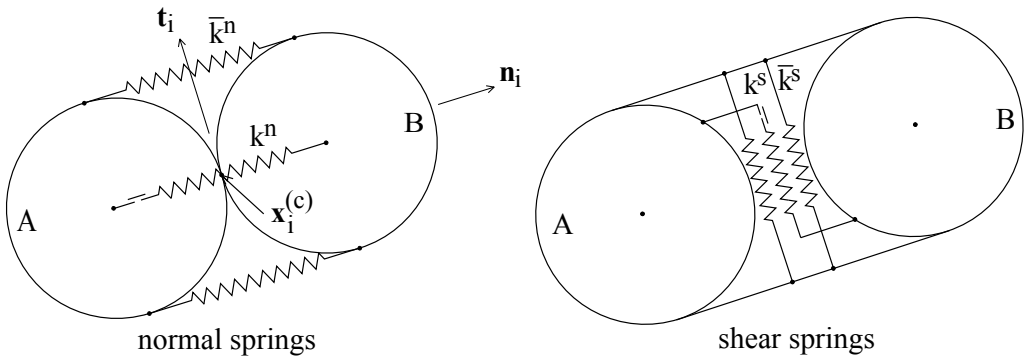

Figure 17: Parallel bond joining a pair of particles (A and B). The parallel bond part, resisting both relative displacements and rotations, is represented by four linear springs with stiffness $\bar{k}^n$ and $\bar{k}^s$ in normal and shear directions respectively. The contact part consists of two linear springs k^n and k^s resisting the relative displacements when the bond is broken and particles overlap. The normal vector n_i and tangent vector t_i define the contact plane together with the contact point $x_i^{(c)}$. In this figure the parallel bond radius is $\alpha = 1$.

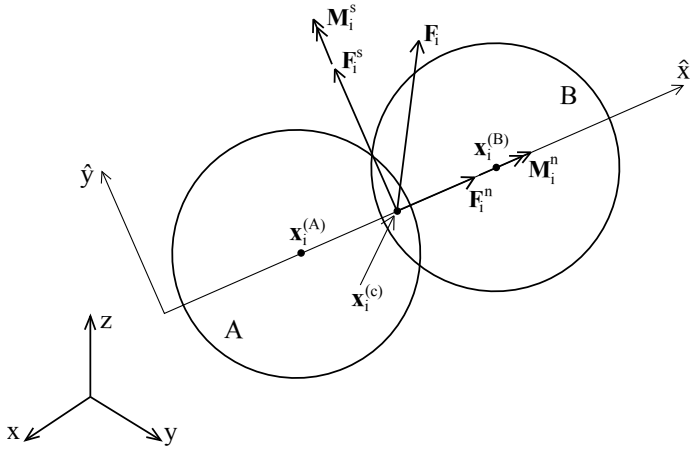

Figure 18: The forces and moments acting on the contact plane of two particles in compression connected by a parallel bond.

The contact spring resisting overlap is only activated when the bond is broken and the spheres are overlapping. This model is implemented in the code but not used when modelling elastic behaviour. Normal and shear forces are carried by the contact. These force increments are given by

$$\Delta F_i^{n(c)} = k^n \Delta u_i^n, \tag{12}$$

$$\Delta F_i^{s(c)} = k^s \Delta u_i^s, \tag{13}$$

where k^n and k^s are the contact stiffness. The Coulomb friction acts as the upper limit of the tangential shear force carried by the contact $||F_i^{s(c)}|| > \mu ||F_i^{n(c)}||$. If this

limit is achieved, slippage occurs between the particles.

The displacement increment between two particles during one time step is given by $\Delta u_i = v_i \Delta t$, where Δt is the length of one time increment and v_i is the relative velocity between particles A and B and it is given by

$$v_i = (\dot{x}_i^{(A)} + e_{ijk}\omega_j^{(A)}(x_k^{(c)} - x_k^{(A)})) - (\dot{x}_i^{(B)} + e_{ijk}\omega_j^{(B)}(x_k^{(c)} - x_k^{(B)})), \tag{14}$$

where $\dot{x}_i$ and ω_j are translational and rotational velocities, respectively, and e_{ijk} is the permutation symbol. The normal component of the relative velocity is given by $v_i^n = v_j n_j n_i$, where n_i is the unit normal of the contact plane (see Figure 17). The tangential velocity is then obtained by subtracting the normal component from the total velocity, $v_i^s = v_i - v_i^n$.

The parallel bond can also carry moments in two directions, bending and twisting. Bending is caused by the tangential component and twisting by the normal component of the relative rotation increment vector, which is given by

$$\Delta\theta_i = (\omega_i^{(A)} - \omega_i^{(B)})\Delta t, \tag{15}$$

The moment increments are then given by

$$\Delta M_i^{n(pb)} = \bar{k}^s J^{pb} \Delta\theta_i^n, \tag{16}$$

$$\Delta M_i^{s(pb)} = \bar{k}^n I^{pb} \Delta\theta_i^s, \tag{17}$$

where ΔM_i^n is the twisting moment around the contact normal n_i and ΔM_i^s is the bending moment around the contact tangent t_i. I^{pb} and J^{pb} are the moment of inertia and polar moment of inertia of the bond cross section, respectively. They are calculated from

$$I^{pb} = \frac{1}{4}\pi R_b^4, \tag{18}$$

$$J^{pb} = \frac{1}{2}\pi R_b^4, \tag{19}$$

An additional contribution to the moment is given by the cross product of the shear force increment and the vector from the contact to the particle centroid. (see Figure 18)

$$\Delta M_i^s = e_{ijk}\Delta F_i^s (x_i^{(A)} - x_i^{(c)}) \tag{20}$$

The force and moment increments are summed for each particle to form a resultant force and moment acting on the centroid of the particle. These resulant force and moment vectors are given by

$$F_r^t = F_r^{t-\Delta t} + \Delta F_i^{pb} + \Delta F_i^c \tag{21}$$

$$M_r^t = M_r^{t-\Delta t} + \Delta M_i^{pb} + \Delta M_i^s, \tag{22}$$

where ΔF_i^{pb}, ΔF_i^c and ΔM_i^{pb} are the sums of the normal and shear components. These vectors are then used to update the positions of the particles.

3.2.3 Timoshenko beam model

The Timoshenko beam model is an alternative bond model that is based on placing cylindrical Timoshenko beam elements between particle centroids. The beams are considered massless in the simulation. The beam ends share the same six degrees of freedom as the particles and the beam can transfer both normal and shear loads as well as bending and twisting moments. The Timoshenko beam theory is well suited for beams with larger thickness to length ratio. It takes into account first order shear deformations by assuming that cross sections, initially normal to the neutral axis, do not necessarily remain normal after deformation (Timoshenko and Gere, 1972).

The same incremental displacements used in the parallel bond model are also used to determine the load increments at beam ends. According to the Timoshenko beam theory, the incremental forces after one time step are given by the constitutive equation (Brown et al., 2014)

$$\Delta F_i^l = K_{ij} \Delta u_i^l, \tag{23}$$

where ΔF_i^l is the combined incremental force and moment vector, K_{ij} is the tangential stiffness matrix and Δu_i^l is the combined displacement and rotation increment vector. The superscript l stands for the local coordinate system of the bond. The load vector has six components for both beam ends (Figure 19) and it is given by

$$\begin{aligned} \Delta F_i^l = [&\Delta F_x^A \ \Delta F_y^A \ \Delta F_z^A \ \Delta M_x^A \ \Delta M_y^A \ \Delta M_z^A \\ &\Delta F_x^B \ \Delta F_y^B \ \Delta F_z^B \ \Delta M_x^B \ \Delta M_y^B \ \Delta M_z^B]^T. \end{aligned} \tag{24}$$

Similarly the combined displacement and rotation increment vector has in total 12 components

$$\begin{aligned} \Delta u_i^l = [&\Delta u_x^A \ \Delta u_y^A \ \Delta u_z^A \ \Delta \theta_x^A \ \Delta \theta_y^A \ \Delta \theta_z^A \\ &\Delta u_x^B \ \Delta u_y^B \ \Delta u_z^B \ \Delta \theta_x^B \ \Delta \theta_y^B \ \Delta \theta_z^B]^T. \end{aligned} \tag{25}$$

The tangential stiffness matrix K_{ij} is of size 12 x 12. The bonds are linear elastic and their deformations are assumed to be small during the simulation. Therefore, the stiffness matrix remains constant until failure and its general form can be derived from four differential beam equations for axial displacement, twist, deflection due to shear and deflection due to bending. The stiffness matrix has been derived by Przemieniecki (1968) and it can be presented with four 3 x 3 submatrices K_1, K_2, K_3 and K_4 as

$$K_{ij} = \begin{bmatrix} K_1 & -K_2 & -K_1 & -K_2 \\ K_2 & K_3 & -K_2 & K_4 \\ -K_1 & K_2 & K_1 & K_2 \\ K_2 & K_4 & -K_2 & K_3 \end{bmatrix}, \tag{26}$$

where

$$K_1 = \begin{bmatrix} \frac{E_b A_b}{L_b} & 0 & 0 \\ 0 & \frac{12 E_b I_b}{L_b^3 (1+\Phi)} & 0 \\ 0 & 0 & \frac{12 E_b I_b}{L_b^3 (1+\Phi)} \end{bmatrix}, \tag{27}$$

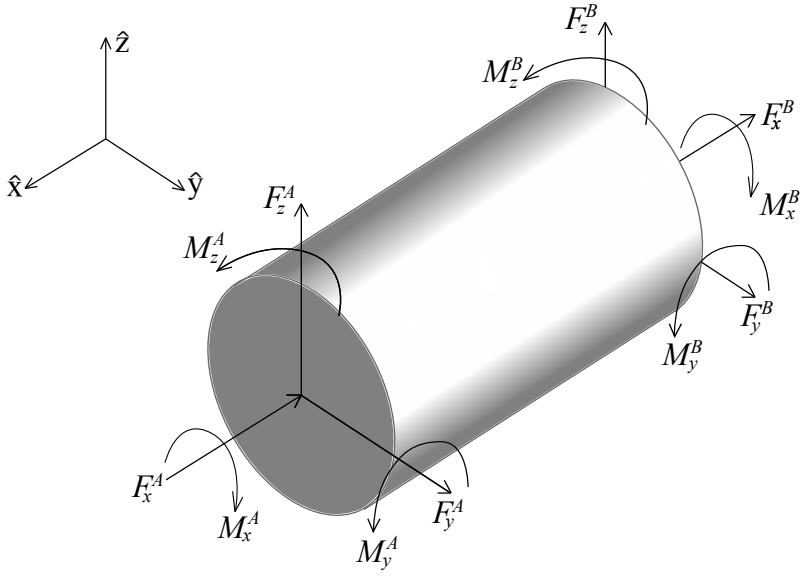

Figure 19: Force and moment components in the local coordinate system acting at the ends of the Timoshenko beam.

$$K_2 = \begin{bmatrix} 0 & 0 & 0 \\ 0 & 0 & \frac{-6E_bI_b}{L_b^2(1+\Phi)} \\ 0 & \frac{6E_bI_b}{L_b^2(1+\Phi)} & 0 \end{bmatrix}, \tag{28}$$

$$K_3 = \begin{bmatrix} \frac{E_bI_b}{L_b(1+\nu_b)} & 0 & 0 \\ 0 & \frac{E_bI_b(4+\Phi)}{L_b(1+\Phi)} & 0 \\ 0 & 0 & \frac{E_bI_b(4+\Phi)}{L_b(1+\Phi)} \end{bmatrix}, \tag{29}$$

$$K_4 = \begin{bmatrix} \frac{-E_bI_b}{L_b(1+\nu_b)} & 0 & 0 \\ 0 & \frac{E_bI_b(2-\Phi)}{L_b(1+\Phi)} & 0 \\ 0 & 0 & \frac{E_bI_b(2-\Phi)}{L_b(1+\Phi)} \end{bmatrix}. \tag{30}$$

Above, E_b is the beam Young's modulus, A_b is the cross sectional area, L_b is the beam length, I_b is the moment of inertia of the cross section, ν_b is the beam Poisson's ratio and Φ is the Timoshenko shear coefficient. The cross sectional quantities A_b and I_b are be obtained using equations 9 and 18, respectively. The Timoshenko shear coefficient is given by

$$\Phi = \frac{f_s 12 E_b I_b}{G_b A_b L_b^2} = \frac{20 r_b^2 (1+\nu_b)}{3 L_b^2}, \tag{31}$$

where G_b is the beam shear modulus and f_s is the form factor, which is 10/9 for a circular cross section (Timoshenko and Gere, 1972). Similar to the parallel bond, the radius of the beam r_b is chosen to equal the particle radius in this study.

The global displacement increments are calculated by multiplying the velocities, obtained by the explicit time integration, with the time step Δt. In order to calculate the force increments at the beam ends these displacements need to be rotated to local coordinate systems, that are stored separately for each bond. This is done by multiplying with the transformation matrix T_{ij}, so that

$$\Delta u_i^l = \begin{bmatrix} T_{ij} & & & \\ & T_{ij} & & \\ & & T_{ij} & \\ & & & T_{ij} \end{bmatrix} \Delta u_i. \tag{32}$$

The local force and moment increments are obtained using Equation 23. After rotating these load increments back to the global coordinates they are added to the resultant forces and moments of each particle. For particle A these forces are given by

$$F_r^t = F_r^{t-\Delta t} + T_{ij}^{-1} \Delta F_{i=1,2,3}^l, \tag{33}$$

$$M_r^t = M_r^{t-\Delta t} + T_{ij}^{-1} \Delta F_{i=4,5,6}^l, \tag{34}$$

where $\Delta F_{i=1,2,3}^l$ represents the first three components of the local load increment vector, meaning the forces acting on particle A.

3.2.4 Viscous damping

The bond model is constructed of linear springs or linear elastic beams, which means that there is no energy dissipation during deformation. This is physically unrealistic as it causes the particles to vibrate permanently after the initial load or velocity is introduced to the system. To avoid this, damping has to be used. The damping can be viscous or non-visous. Cundall and Strack (1979) proposed a global viscous damping proportional to the particle mass envisioned as dashpots connected to the ground. Later Cundall (1987) used a local non-viscous damping, that was directly proportional to the non-zero resultant force acting on a particle. In this work, a local viscous dashpot is introduced between every bonded particle pair. The damping force created by this dashpot and acting on particle A is given by

$$F_i^d = -cv_i, \tag{35}$$

where c is the damping coefficient of translational motion and v_i is the relative velocity between the particles A and B. The damping forces are added to the particles resultant force and reseted to zero after every time step, and thus are not incremental.

A bonded pair of particles can be approximated as a two-body problem with a spring and viscous damper between the particles. The critical damping coefficient of this system is (Ergenzinger et al., 2011)

$$c_{cr} = 2\sqrt{k m_{red}}, \tag{36}$$

where k is the average spring constant of the parallel bond or in the Timoshenko beam model it is given by $k = EA_b/L_b$. The reduced mass is equal to $m_{red} = (m_1 m_2)/(m_1 + m_2)$ and for equally sized particles it is reduced to $m_{red} = m_p/2$.

In this work the particles share multiple bonds, which should be taken into account when calculating the damping coefficient. Ergenzinger propose a heuristic approach to the problem by stating that the damping is proportional to the square root of number of bonds in one direction as the spring stiffnesses of bonds in the same direction can be summed up. By dividing the three-dimensional space into three direction and allocating bonds equally to each direction, the damping coefficient is scaled by the square root of one third of the average coordination number

$$c = \frac{\xi c_{cr}}{\sqrt{\hat{C}_n/3}}, \tag{37}$$

where ξ is the damping ratio and $\hat{C}_n$ is the coordination number, which is equal to the number of bonds connected to the particle.

3.3 Updating particle positions

The total force vector acting on a particle is equal to the sum of the damping force, external force and all forces produced by the deformed bonds connected to this particle. Knowing this resultant force vector the acceleration of a particle at time t can be calculated from the dynamic equation of motion, also known as the Newton's second law. For translational motion the equation is

$$F_i^t = m_p a_i^t, \tag{38}$$

where F_i^t is the total force vector at time t, m_p is the particle mass and a_i^t the acceleration vector at time t. An explicit time integration scheme is then used to obtain the velocities and positions at times $t + \Delta t/2$ and $t + \Delta t$. The method used in this work is similar to the central-difference method and it is referred as the position Verlet time integration scheme (O'Sullivan, 2011). The relation between the acceleration and velocity vectors is given by

$$a_i^t = \frac{1}{\Delta t}(v_i^{t+\Delta t/2} - v_i^{t-\Delta t/2}). \tag{39}$$

By combining equations 38 and 39 the velocity vector at time $t + \Delta t/2$ can be calculated

$$v_i^{t+\Delta t/2} = v_i^{t-\Delta t/2} + \Delta t m_p^{-1} F_i^t. \tag{40}$$

This velocity is considered to equal the average velocity over the time increment from t to $t + \Delta t$. The updated particle position $x_i^{t+\Delta t}$ can then be calculated as

$$x_i^{t+\Delta t} = x_i^t + \Delta t v_i^{t+\Delta t/2}. \tag{41}$$

It is important to notice that using this time integration scheme there is a lag of $\Delta t/2$ between the calculation of updated velocities and positions.

The calculation of the rotational motion in 3D is significantly more complex than calculation of translational motion as there can be coupling between the translational and rotational degrees of freedom and between the three rotational degrees of freedom (O'Sullivan, 2011). However, if the local coordinate frame, about which the rotations are analyzed, coincides with the particles center of mass these couplings are eliminated. When spherical particles are used, also the coupling between each three rotational degrees of freedom can be eliminated as the inertia tensor becomes diagonal. The same can be done with arbitrary shaped particles if the local coordinate frame is rotated to coincide with the principal axes of inertia. The details of this are, however, not treated in this work. The diagonal inertia tensor is given by

$$I_{ij} = \begin{bmatrix} I_{xx} & 0 & 0 \\ 0 & I_{yy} & 0 \\ 0 & 0 & I_{zz} \end{bmatrix}, \tag{42}$$

where moments of inertia for a sphere are $I_{xx} = I_{yy} = I_{zz} = \frac{2}{5} m_p r_p^2$. Knowing the resultant moment acting on a particle, the angular position in the local coordinate frame of the particle can be updated using the position Verlet time integration scheme described above. The local coordinate frame has its origin in the center of mass of the particle and the axes are parallel to the global coordinate system. The dynamic rotational equation of motion is

$$M_i^t = I_{ij} \dot{\omega}_i^t, \tag{43}$$

where M_i^t is the resultant moment vector and $\dot{\omega}_i^t$ is the angular acceleration of the particle at time t. The angular velocity vector at time $t + \Delta t/2$ and the angular orientation at time $t + \Delta t$ are then calculated with the following equations

$$\omega_i^{t+\Delta t/2} = \omega_i^{t-\Delta t/2} + \Delta t I_{ij}^{-1} M_i^t, \tag{44}$$

$$\theta_i^{t+\Delta t} = \theta_i^t + \Delta t \omega_i^{t+\Delta t/2}, \tag{45}$$

where $\theta_i^{t+\Delta t}$ is the angular orientation vector of the particle at the end of the time step.

3.4 Selecting the time step

According to O'Sullivan and Bray (2004) it can be shown, using linear stability analysis, that the central time difference method is conditionally stable and a critical time step required for stable simulations can be calculated. For a linear undamped system of connected springs and masses the critical time step is governed by the maximum frequency in the following manner

$$\Delta t_{crit} = \frac{2}{\omega_{max}} = \frac{2}{\sqrt{\lambda_{max}}}. \tag{46}$$

The maximum frequency ω_{max} is related to the eigenvalue λ_{max} of the $M_{ij}^{-1} K_{ij}$ mass-stiffness matrix, where M_{ij} is the mass matrix and K_{ij} is the stiffness matrix of the

system. For a large system of connected particles this matrix becomes complicated to formulate and solving of the eigenvalues is also time consuming. The maximum eigenvalue of the mass-stiffness matrix of a single element can be used to estimate the eigenvalue of the entire system according the following relationship

$$\lambda_{max} \leq \lambda^{e}_{max}, \tag{47}$$

where λ_{max} is the eigenvalue of the global $M^{-1}_{ij}K_{ij}$ matrix and λ^{e}_{max} is the eigenvalue of the $M^{e-1}_{ij}K^{e}_{ij}$ matrix for a single spring element. In the study, O'Sullivan derived the stiffness matrix for a spring element with one normal and shear spring connecting equally sized spheres. This matrix was applied to a unit cell of a hexagonal closepacking and the mass matrix was derived by allocating the masses of the particles to the spring elements equally according to the geometry of the unit cell (see Figure 20). By calculating the eigenvalues of the mass-stiffness matrix and further assuming that the normal and shear spring stiffness are equal, the following relationship was obtained (O'Sullivan and Bray, 2004)

$$\Delta t_{crit} \leq 0.22\sqrt{\frac{m_p}{k}}, \tag{48}$$

where m_p is the mass of a single particle and k is the stiffness of both normal and shear springs. This equation is used to estimate an appropriate time step used in the simulations that are performed in this thesis. The normal stiffness of a parallel bond is used as the stiffness value in Equation 48. The case of hexagonal closepacking is a more restrictive case regarding the critical time step. Thus, this equation can also be used to estimate the time step for random packing simulations.

3.5 Energy balance

One way to monitor the numerical stability of the explicit simulation is to calculate the energy balance of the system. Numerical instability in a simulation leads to an erronous distribution of energy which can be detected as violations in the conservation of energy (O'Sullivan and Bray, 2004). The total energy of the system can be broken down into four components, kinetic energy W_{kin}, internal energy W_{int}, external energy W_{ext} and dissipated energy W_{dis}. The kinetic energy of the system is the sum of all the kinetic energies stored in the particles motion

$$W_{kin} = \frac{1}{2}\sum_{p=1}^{N_p} v_i^T m_p v_i + \frac{1}{2}\sum_{p=1}^{N_p} \omega_i^T I_{ij} \omega_i, \tag{49}$$

where p stands for particle. During the simulation energy can be stored in the bonds as strain energy, which is considered as internal energy. The strain energy stored in normal and shear springs, when a linear force-displacement or moment-rotation relations are used, is given as a sum of strain energies over the number of bonds (O'Sullivan, 2011)

$$W_{strain} = \sum_{c=1}^{N_c} \left(\frac{\|F_i^n\|^2}{2\bar{k}^n A_{pb}} + \frac{\|F_i^s\|^2}{2\bar{k}^s A_{pb}} + \frac{\|M_i^n\|^2}{2\bar{k}^s J_{pb}} + \frac{\|M_i^s\|^2}{2\bar{k}^n I_{pb}} \right), \tag{50}$$

where c stands for contact or bond.

Energy can be dissipated by multiple means during a simulation. The energy dissipative mechanisms can be damping, friction or fracturing. The energy dissipated by the viscous dashpots between two bonded particles is proportional to the relative velocity of these particles. It is assumed that the damping force given by equation 35 stays constant during one time increment. The dissipated energy during one time increment is the sum over all dashpots and over the entire simulation, and at time t it is

$$W_d^t = W_d^{t-\Delta t} + \sum_{c=1}^{N_c} F_i^d v_{i_{rel}}^t \Delta t. \tag{51}$$

External energy can be brought to the system by different means. Usually external energy is the work done by an applied force at a certain particle, work done by moving rigid boundary walls or work done by gravity. The work done by external forces acting on specific particles is

$$W_{ext}^t = W_{ext}^{t-\Delta t} + \sum_{p=1}^{N_p} F_i^{ext} v_i^t \Delta t. \tag{52}$$

According to Belytschko et al. (2000) the energy balance requirement for a stable simulation is given by

$$(|W_{kin} + W_{int} + W_{dis} - W_{ext}|) \leq \varepsilon \max(W_{kin}, W_{int}, W_{ext}, W_{dis}), \tag{53}$$

where ε is a constant generally on the order of 10^{-2}. This means that an error with a magnitude of 1 % of the largest energy component is allowed. The energy breakdown of the total energy during simulations can be found from Appendix C.

3.6 Calculating stresses in the specimen

Stress is a continuum quantity and for a discrete assembly of particles it cannot be directly obtained from the external loading condition. Stress can only exist in the particles as voids between particles cannot transfer loads. The average stress in a representative volume element (RVE) in the specimen can be calculated using average values of these individual particles. A detailed derivation of the RVE stress is done by Potyondy and Cundall (2004). The main steps in the derivation are presented here. The average stress in the RVE element is given by

$$\bar{\sigma}_{ij} = \frac{1}{V} \sum_{N_p} \bar{\sigma}_{ij}^{(p)} V^{(p)}, \tag{54}$$

where $\bar{\sigma}_{ij}$ is the average stress tensor for the RVE, V is the volume of the RVE, N_p is the number of particles having centroids inside the RVE, $\bar{\sigma}_{ij}^{(p)}$ is the average stress tensor and $V^{(p)}$ is the volume of particle p. The average stress of particle p is defined as an integral over the particle volume and divided by the volume as follows

$$\bar{\sigma}_{ij}^{(p)} = \frac{1}{V^{(p)}} \int_{V^{(p)}} \sigma_{ij}^{(p)} dV^{(p)}, \tag{55}$$

Any tensor notation can be decomposed such that

$$S_{ij} = \delta_{ik} S_{kj} = x_{i,k} S_{kj} = (x_i S_{kj})_{,k} - x_i S_{kj,k}, \tag{56}$$

where δ_{ik} is the Kronecker delta and $x_{i,k}$ is the partial derivative of the position vector components. Applying the identity of Equation 56, the average stress in a particle can be written

$$\bar{\sigma}_{ij}^{(p)} = \frac{1}{V_{(p)}} \int_{V^{(p)}} [(x_i \sigma_{kj}^{(p)})_{,k} - x_i \sigma_{kj,k}^{(p)}] dV^{(p)}. \tag{57}$$

When evaluating the stress, each particle is assumed to be in equilibrium and the stresses are assumed to be continuous inside the particle. Further in the absence of body forces, this leads to the equilibrium condition $\sigma_{ij,i} = 0$ and the second term in equation 57 vanishes. By applying the Gauss divergence theorem, the rest of the volume integral can be written as a surface integral over the particle surface $S^{(p)}$

$$\begin{aligned} \bar{\sigma}_{ij}^{(p)} =& \frac{1}{V_{(p)}} \int_{S^{(p)}} (x_i \sigma_{kj}^{(p)}) n_k dS^{(p)} \\ =& \frac{1}{V_{(p)}} \int_{S^{(p)}} x_i t_j^{(p)} dS^{(p)}, \end{aligned} \tag{58}$$

where n_k is the outward unit normal to the surface and $t_j^{(p)}$ is the traction vector acting on the particle surface. In this derivation the moments acting on particle are assumed to be small compared to the point forces and they are neglected. The point forces are acting at discrete contact locations. Therefore, the surface integral of tractions can be replaced by a sum over the contacts such that

$$\bar{\sigma}_{ij}^{(p)} = -\frac{1}{V^{(p)}} \sum_{N_c} x_i^{(c)} F_j^{(c)}, \tag{59}$$

where $x_i^{(c)}$ is the contact location and $F_j^{(c)}$ is the force acting at the contact. The negative sign is added to produce negative stresses with compressive forces. By writing the contact point as a sum of two vectors

$$x_i^{(c)} = x_i^{(p)} + |x_i^{(c)} - x_i^{(p)}| n_i^{c,p}, \tag{60}$$

which are the position vector of the particle and the vector directed from the particle centroid to the contact, and noting that

$$\sum_{N_c} F_j^{(c)} = 0, \tag{61}$$

for a particle in equilibrium, the following equation is obtained

$$\bar{\sigma}_{ij}^{(p)} = -\frac{1}{V^{(p)}} \sum_{N_c} |x_i^{(c)} - x_i^{(p)}| n_i^{c,p} F_j^{(c)}. \tag{62}$$

This expression for average stress in the particle can be subsituted in Equation 54 to get the stress tensor in the RVE.

4 Simulation setup

This chapter presents the simulations of this work. The chapter starts with a description and short analysis of the three packing methods used to discretize the test specimens. This is followed by a description of the input parameters and the varied parameters of the simulations. Lastly, the loading methods and the application of boundary conditions in uniaxial and flexural loading setups are presented. Table 1 shows the simulation matrix, which presents all the simulated setups.

Table 1: Simulation matrix, which shows the number of simulations for each setup. In total 207 simulations were conducted. Five different random packings were used for each particle size in order to see the magnitude of deviations in the elastic constants. The abbreviations in the table are PB meaning parallel bond, Tim. Timoshenko beam, HCP hexagonal closepacking and RCP random closepacking.

		Number of simulations									
	r_p (mm)	2.5		5.0		7.5		10.0		12.5	
	Bond	PB	Tim.	PB	Tim.	PB	Tim.	PB	Tim.	PB	Tim.
Tensile	Uniform	1	1	1	1	1	1	1	1	1	1
	HCP	1	1	1	1	1	1	1	1	1	1
	RCP	5	5	5	5	5	5	5	5	5	5
Compressive	Uniform	1	1	1	1	1	1	1	1	1	1
	HCP	1	1	1	1	1	1	1	1	1	1
	RCP	5	5	5	5	5	5	5	5	5	5
Flexural test	Uniform	1	0	1	1	1	1	1	1	1	1
	HCP	1	0	1	1	1	1	1	1	1	1
	RCP	5	0	5	5	5	5	5	5	5	5

4.1 Discretization of the test specimen

The test specimen of continous material is here discretized by generating a sphere packing inside the rectangular cuboid specimens. The dimensions of the specimens are chosen to be $0.25 \times 0.1 \times 0.1$ m, according to a typical ice sample used in compressive tests (Timco and Weeks, 2010). A sphere packing of monodisperse spheres is characterized by its porosity, average coordination number $\hat{C}_n$ and order parameters describing how ordered or disordered the packing is (Ergenzinger et al., 2011). The average coordination number is the average number of contacts, or at the same time bonds, per particle. Three different packing methods with different characteristics are used in this study:

1. Uniform packing. Spheres are arranged in a simple cubic lattice.

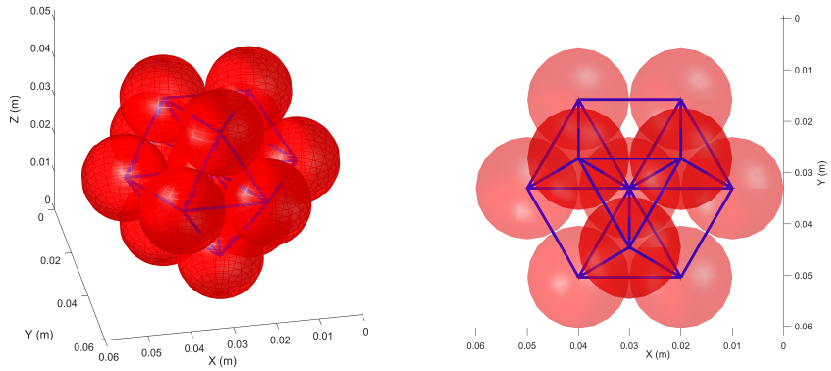

Figure 20: A unit cell in the hexagonal closepacking.

2. Hexagonal close packing. Unit cells of 13 spheres described in Figure 20 are repeated regularly. It is the densest packing method of equally sized spheres.

3. Random close packing. A radius expansion algorithm is used to generate a dense packing from initially randomly positioned spheres. (Labra and Onate, 2009)

The random close packing here is generated with a sphere mesher tool included in the software GiD 13.0 (GiD, 2016). The packing algorithm generates first a high porosity packing with a predefined level of randomness in the sphere locations. Next, it starts an iterative process of increasing the particle radius and correcting positions to avoid overlaps. The iteration is terminated when the value of the distance function being minimized is under a tolerance value defined by the user. The sphere centroid coordinates are then exported as a text-file, which is read by the MATLAB script. Examples of these three packing methods are compared in table 2 and figure 22. Furthermore, typical distributions of coordination numbers in random packings are presented in Figure 21.

The theoretical porosity and average coordination number for hexagonal closepackings are $p = 0.26$ and $\hat{C}_n = 12$, respectively. For random packings of monodisperse spheres the generally obtained values for the same parameters are $p \approx 0.36$ and $\hat{C}_n \approx 6.0$ (Ergenzinger et al., 2011). These theoretical values for porosity are lower

Table 2: Comparison between packings inside a polygon of $0.25 \times 0.1 \times 0.1$ meters. Spheres are equally sized in each packing with a radius $r_p = 5$ mm. N_p is the number of particles, p is the porosity and $\hat{C}_n$ is the average coordination number.

	Dimensions (m)	N_p	p	$\hat{C}_n$
Uniform	$0.25 \times 0.1 \times 0.1$	2500	0.48	5.52
HCP	$0.255 \times 0.0995 \times 0.0998$	3300	0.32	10.74
RCP	$0.25 \times 0.1 \times 0.1$	2855-2903	0.39-0.40	6.93-7.17

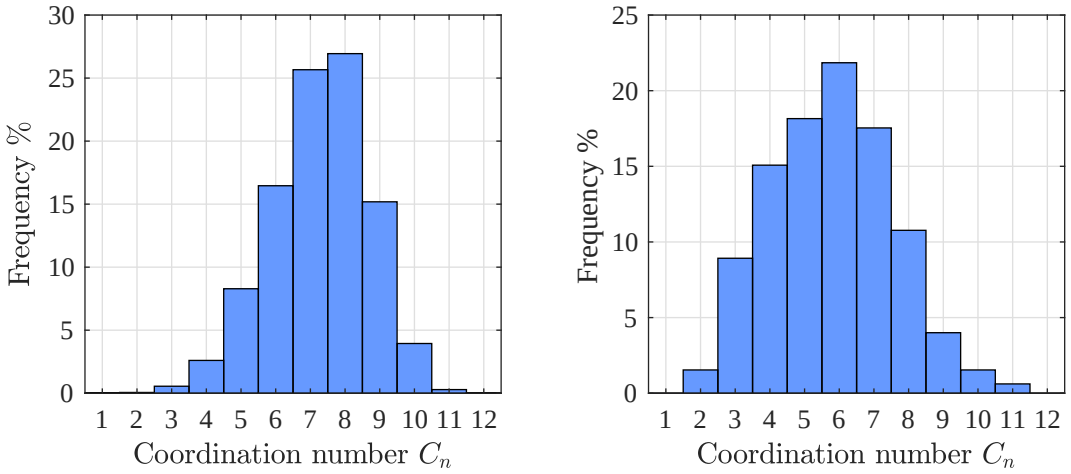

(a) $r_p = 10$mm. (b) $r_p = 2.5$mm.

Figure 21: The distribution of the particle coordination number in two random packings.

compared to the values of the packings used in this study listed in table 2. Also, the theoretical coordination number of the HCP is higher compared to the value in the simulated packings. The difference in the porosity is at least partly due to the boundary effects at polygon sides. A perfect packing cannot be produced against the planar walls bounding the specimens. This leads to a high porosity in the boundaries. By decreasing the particle radius this effect is reduced.

The porosity of the specimen is reasonably high with all packing methods. To keep the mass of the specimen equivalent to the mass of a similar continuum volume, the density of the particles have to be scaled. This is done in the following manner

$$\rho_p = \frac{\rho}{1-p}, \tag{63}$$

where ρ_p is the density of the particles, ρ is the density of the modelled continuum and p is the porosity of the packing. The masses of the particles are important if the inertia effects are significant or if dynamic similarity between simulations is required. In this work, the desired results do not depend on the dynamic behaviour of the model, in which case the inertia effects are not of great importance and the effect of the density-scaling is minimal.

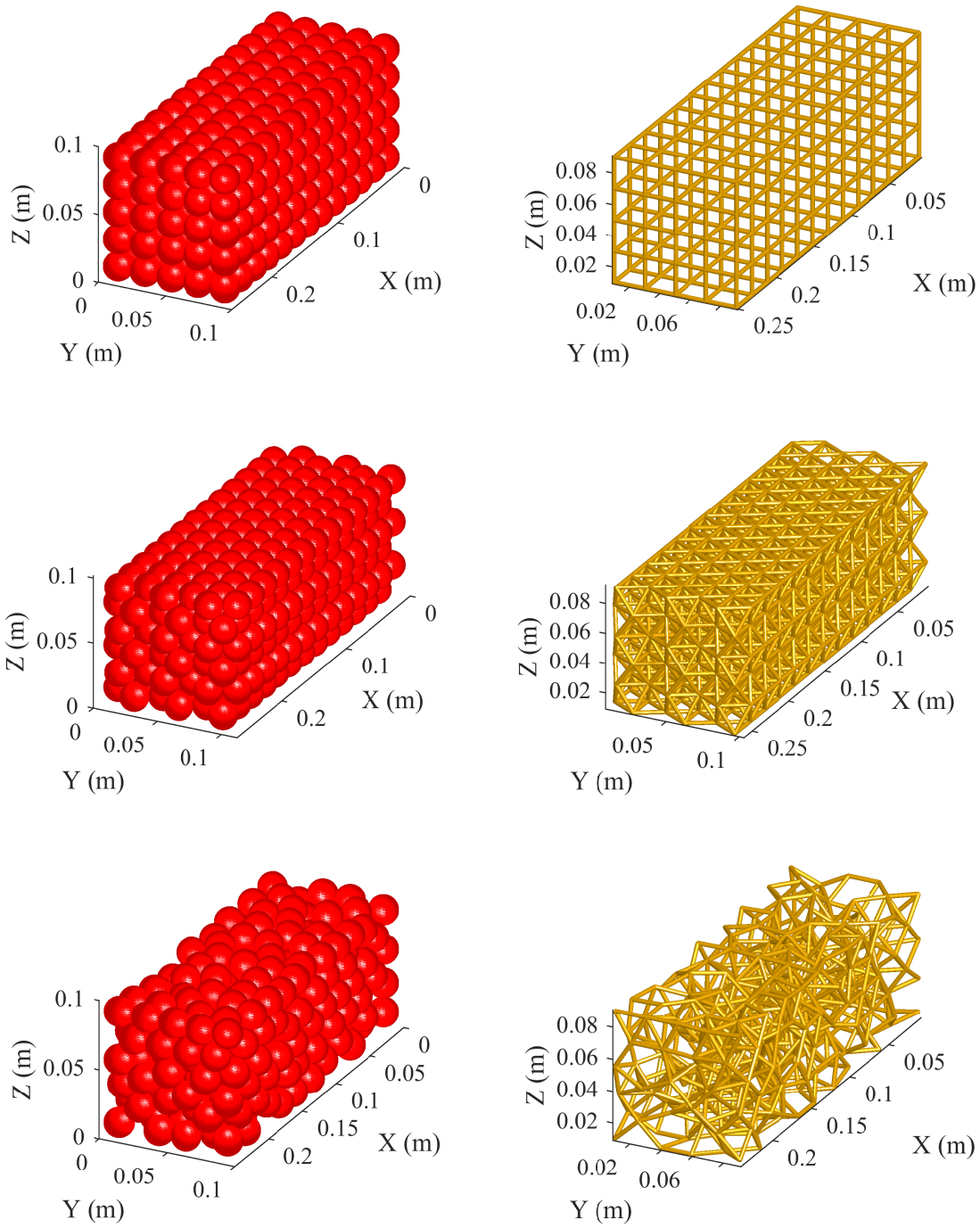

Figure 22: Examples of the three particle packing methods and illustration of the bond networks inside the packings. From top to bottom: uniform, hexagonal closepacking (HCP) and random closepacking (RCP). All particles have a radius of $r_p = 10$ mm.

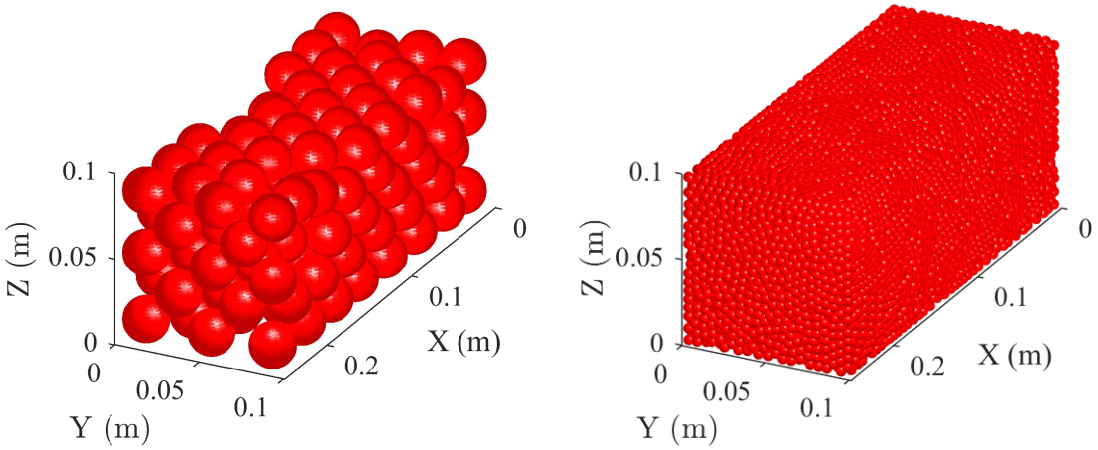

(a) $r_p = 12.5$mm. (b) $r_p = 2.5$mm.

Figure 23: Comparison between random packings with the largest and smallest particle size.

4.2 Simulation parameters

There is a large set of parameters that have to be determined and can be varied in a DEM simulation. In this study, the micromechanical parameters such as bond stiffness and Poisson's ratio are kept constant. The micromechanical parameters are chosen to correspond to the mechanical properties of sea ice in macroscale and they are based on the review by Timco and Weeks (2010). The parallel bond normal spring stiffness is determined, so that the normal spring stiffness is equal to the axial stiffness of a same size beam $K = EA/L$ (Potyondy and Cundall, 2004). As the stiffness of the parallel bond is defined per unit area and the length of the parallel bond is two times the particle radius, the normal stiffness is obtained by dividing the microscopic Young's modulus by two times the particle radius $\bar{k}^n = E_b/2r_p$.

The normal to shear stiffness ratio of the parallel bond is obtained by calibrating the model against the Timoshenko beam model. The calibration is done with the uniaxial compressive test so that the two bond models produce similar macroscopic Young's moduli for a random closepacking with particle radius $r_p = 10$ mm. The stiffness ratio is iterated with a trial and error method. The varied parameters in this study are the particle radius together with the packing geometry. The density of the particles and the damping coefficient are scaled according to Equations 63 and 37, respectively.

4.3 Uniaxial tensile and compressive tests

Solid materials that are homogenous, isotropic and elastic are characterized by two material constants, Young's moudulus and Poisson's ratio. These constants are usually determined by conducting quasi-static tensile or compressive tests. For real materials the tests are usually performed with hydraulic test machines, but the same

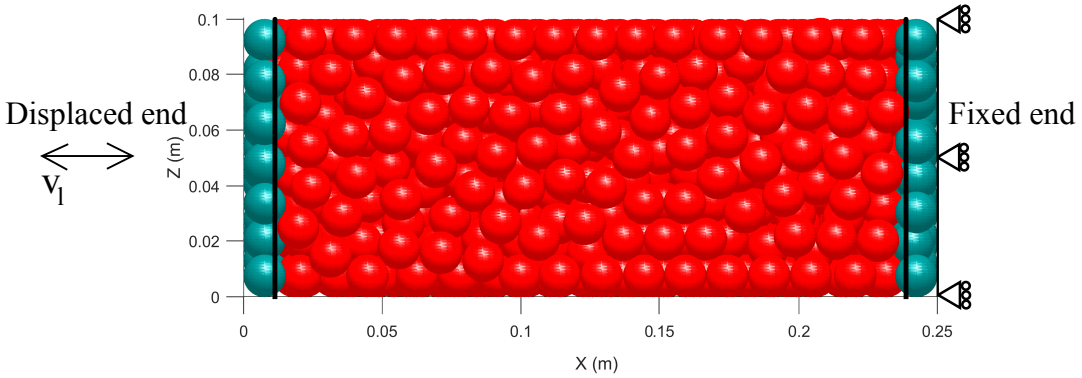

Figure 24: Tensile and compression test setup. Black vertical lines mark the limits of the end particles zone. The right side of the test specimen is fixed in x-direction but the particles are allowed to slide in the yz-plane.

process can be simulated with the bonded particle model. In this study, the tensile and compressive tests are strain-controlled tests, which means that the end of the specimen is displaced with a constant velocity and strain rate.

In an uniaxial test, a set of particles defined as end particles, is selected form the discretized test specimen as described in Figure 24. A particle is assigned as end particle if the centroid of the particle is inside a limit of $1.5 \times r_p$ from the specimen boundary. An initial linearly ramped loading velocity is assigned to the particles so that the left side end particles have a loading velocity $v_l = 0.01$ mm/s and the right side end particles are at rest $v_l = 0$ mm/s. By doing this, a sudden load peak in the left end in the beginning of the simulation is avoided. The boundary conditions were applied such that during the simulation the x-direction velocities of the end particles

Table 3: Properties of the bonds and particles used in the simulations.

Simulation parameters	Values
Parallel bond	
Normal spring stiffness $\bar{k}^n$ (GPa/m)	$E_b/2r_p$
Normal to shear stiffness ratio ($\bar{k}^n/\bar{k}^s$)	4.2
Timoshenko beam	
Young's modulus E_b (GPa)	4.0
Poisson's ratio ν_b	0.3
Form factor f_s	10/9
Particle	
Radius (mm)	2.5, 5, 7.5, 10, 12.5
Sea ice density (kg/m^3)	925

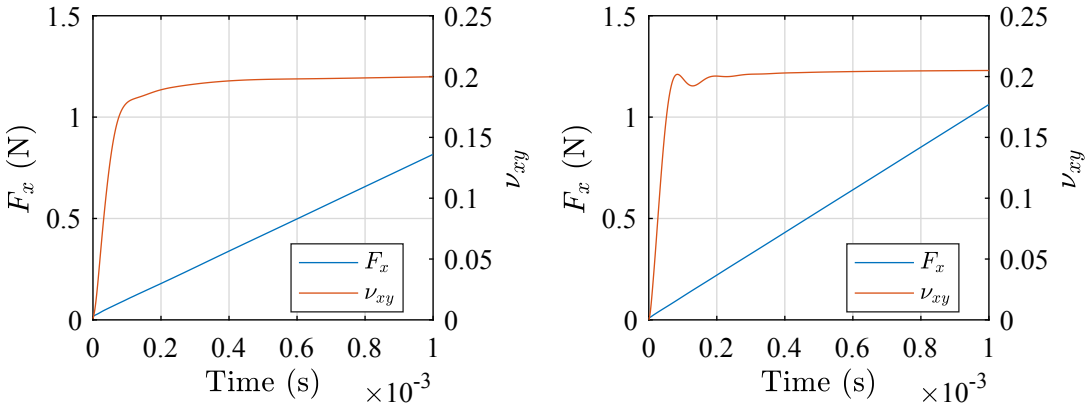

(a) $r_p = 10$ mm. (b) $r_p = 5$ mm.

Figure 25: Loading curves of two RCP specimens in compression. Dynamic effects can be seen in the behaviour of the Poisson's ratio in the beginning of the simulation.

are kept constant and the motion in yz-plane is not restricted. Other particles are allowed to move freely governed by the bond forces.

The force and displacement of the loaded end are recorded and plotted. By assuming small strains the following relationship is then used to calculate the Young's modulus

$$E_x = \sigma\varepsilon^{-1} = \frac{F_x}{A}\frac{L_0}{\Delta L}, \tag{64}$$

where E_x is the Young's modulus, σ is the normal stress and ε the strain in the loading direction, F_x is the recorded load in x-direction, A is the cross sectional area, L_0 is the initial length of the specimen and ΔL is the displacement of the loaded end. The ratio $F_x/\Delta L$ is obtained from the force-displacement curve of the simulation.

The Poisson's ratio is calulated both in y- and z-directions. The strains in these directions are obtained from the average displacements of the bounding particles shown in Figure 26. The Poisson's ratios are then given by

$$\nu_{xy} = -\frac{\varepsilon_x}{\varepsilon_y} = -\frac{\Delta L}{L_0}\frac{w_0}{\Delta w_{avg}}, \quad \nu_{xz} = -\frac{\varepsilon_x}{\varepsilon_z} = -\frac{\Delta L}{L_0}\frac{h_0}{\Delta h_{avg}}, \tag{65}$$

where ε_x, ε_y and ε_z are the strain components, Δw_{avg}, Δh_{avg}, w_0 and h_0 are the change and initial values of width and height, respectively.

Table 4: Simulation parameters. The time step of 0.7 μs is used with $r_p = 5$ mm and 0.2 μs is used with smallest particle size of $r_p = 2.5$ mm.

Parameter	Value
Loading velocity v_l (mm/s)	0.01
Time step Δt (μs)	1.0, 0.7, 0.2

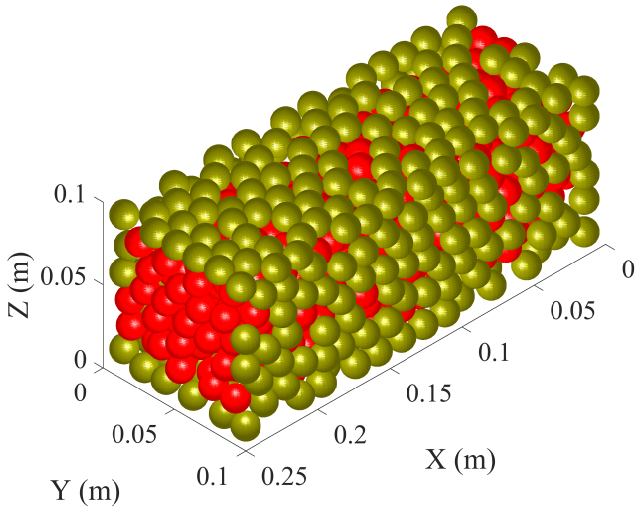

Figure 26: Bounding particles used to calculate the Poisson's ratio of the specimen.

4.4 Three point flexural test

The three point flexural test is a classical experiment in mechanics, used to measure the flexural modulus E_f of a material. It is also used in fracture mechanics to obtain fracture toughness of single edge notch specimens or to study the shear fracture in composite specimens. In this study, it used to determine the flexural stiffness of the discrete element specimens. Before the flexural tests are conducted for full scale specimens, the timoshenko beam model is verified against analytical deflection and natural frequency results. This verification procedure and the results are presented in Appendix B.

A similar setup is created for the full scale specimens, as for the verification beams. Boundary conditions are applied to the bottom corner particles as shown in Figure 28. The external load is linearly increased to 1 kN and it is applied as a distributed load to several particles so that the load is equally divided to particles with centroids in a range of $1.5 \times r_p$ from the midspan. The length of the loading ramp is 5000 time steps for the three largest particle sizes, 10000 steps for $r_p = 5$ mm and 40000 steps for $r_p = 2.5$ mm. After the total load has reached 1 kN the vibration are allowed to dampen as shown in Figure 27. The deflection is calculated from the average displacement of the loaded particles and the particles in the same range from the midspan but on the bottom surface of the beam.

For the smallest particle size of $r_p = 2.5$ mm, a slightly modified simulation is used to obtain a faster convergence toward the state of equilibrium. The vibrations occuring after the loading sequence are reduced by setting the velocities of all particles to zero at the end of the loading ramp. It is verified with a specimen with a larger particle size, that the forced stop does not to affect the final deflection. Regardless of the forced stop, a small vibration with an amplitude of approximately 0.8 % of the deflection remains at the end of the simulation. Therefore, the deflections for the beams with particle radius $r_p = 2.5$ mm are calculated as an average of all the

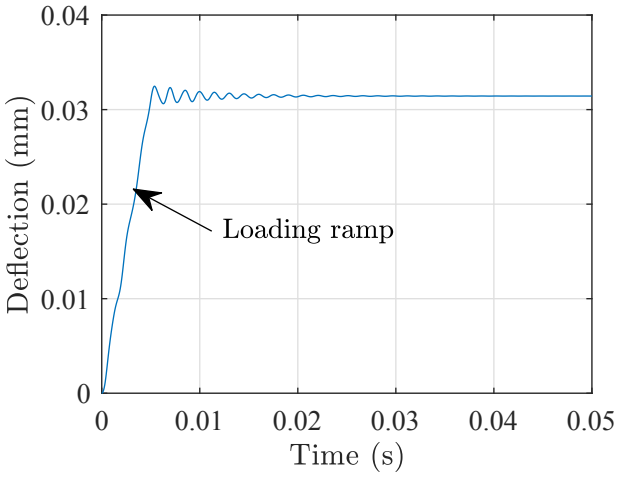

Figure 27: The deflection of a RCP specimen as a function of time. Particle radius $r_p = 7.5$ mm. The load is increased linearly from 0 to 1 kN during 5000 time steps.

deflection values after the loading ramp.

The analytical form for the deflection of a simply supported Timoshenko beam under a central load is given by (Brown et al., 2014)

$$\delta = \frac{FL_e^3}{48E_fI} + \frac{FL_ef_s}{4GA}, \tag{66}$$

where F is the load, L_e is the length between the two supports, E_f is the flexural modulus, I is the moment of inertia of the cross section, f_s is the Timoshenko form factor, G is the shear modulus and A is the area of the cross section. The first term in Equation 66 is the solution for an Euler-Bernoulli beam and the second term takes into account the transverse shear deformation.

The flexural modulus is solved as a function of deflection from Equation 66. The shear modulus G is approximated with the following relationship for isotropic materials $G = E_f/2(1+\nu)$, where ν is the average of ν_{xy} and ν_{xz}, that are obtained from the uniaxial tests. The flexural modulus E_f is then given by

$$E_f = \frac{F}{2\delta}\left[\frac{L_e^3}{24I} + \frac{L_ef_s(1+\nu)}{A}\right]. \tag{67}$$

Equation 67 assumes that the central load is a pure point load. However, in the RCP, HCP and some uniform specimens the load is slightly distributed along the x-axis (see Figure 28). This can be taken into account when deriving the equation for deflection of a Timoshenko beam. For a central load distributed symmetrically around the midspan and over the length b, the deflection is given by the following equation, which is derived based on the paper by Wang (1995)

$$\delta = \frac{F(8L_e^3 - 4b^2L_e + b^3)}{384E_fI} + \frac{(FL_e - Fb)f_s}{4GA}, \tag{68}$$

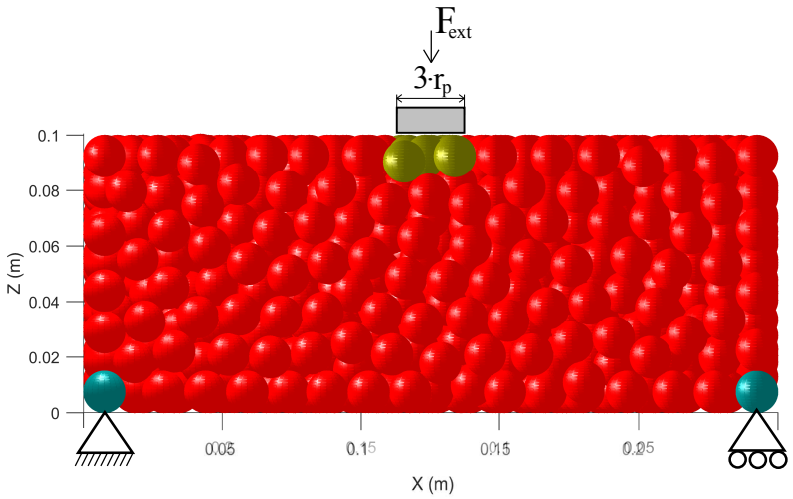

Figure 28: Flexural loading setup: Particles in yellow are assigned with an external load. Left corner particles in blue are constrained in all directions except rotations around y-axis. Right corner particles are allowed to translate in x-direction and rotate around y-axis.

where $F = wb$ and w is the magnitude of the uniformly distributed load with units given in N/m. In the case of a point load, the length b goes to zero and Equation 68 is reduced to Equation 66. The flexural modulus can be solved from Equation 68, thus giving the following relationship

$$E_f = \frac{F}{2\delta}\left[\frac{8L_e^3 - 4b^2L_e + b^3}{192I} + \frac{f_s(L_e - b)(1+\nu)}{A}\right]. \tag{69}$$

The flexural moduli obtained with Equations 67 and 69 are analyzed and compared in the results chapter. The flexural moduli is also compared to the Young's moduli obtained from the uniaxial tests.

5 Results and analysis

The simulation results are presented in this section. Elastic properties of the specimens obtained from the uniaxial and flexural tests are presented. Furthermore, the influence of particle size, particle packing and bond type is analyzed. Finally, the stress state of loaded specimens are presented and analyzed.

5.1 Uniaxial tests

Uniaxial compressive and tensile tests were carried out for 35 specimens with different particle sizes and sphere packings. Identical results were obtained in both compression and tension. The uniform packings produced a constant stiffness value of $E_x = 3.14$ GPa for all particle sizes. Furthermore, the uniform packings did not deform laterally, thus giving a Poisson's ratio of zero.

Figure 29 shows the Young's modulus obtained for random closepacked specimens. The modulus E_x is plotted as a function of particle radius, number of particles and porosity of the specimen. Linear fits are plotted in Figures 29a and 29c. The linear fits approximate well the behaviour of the Young's modulus and suggest that the modulus increases as both particle radius and packing porosity decreases. However, it can be argued that the particle radius and packing porosity are connected to each other. With increasing particle radius the sphere packing in the boundaries of the specimens becomes looser and increases porosity. Earlier studies by André et al. (2012) and Fakhimi and Villegas (2007) suggest that the particle radius does not affect the macroscopic properties of the specimen as long as the particle radius to specimen size ratio is small enough (0.013 in the study by Fakhimi and Villegas (2007)). However, the effect of porosity is not analyzed in these studies. In addition, polydisperse spheres were used, which makes it easier to produce packings with low porosity and less deviation in porosity.

Figure 29b shows the Young's modulus as a function of number of particles. The shape of the curve indicates that the modulus may converge to a specific value as the number of particles increases. More results of specimens with particle radius 2.5 mm$> r_p >$ 5 mm and $r_p <$ 2.5 mm are required for a conclusion and to obtain the value of convergence, which is an upper limit to the Young's modulus. However, the idea of an upper limit is realistic as the minimum theoretical porosity of randomly closepacked equal spheres can be seen to act as a limit to the linear increase of Young's modulus in Figure 29c. The minimum achieved porosity of a random closepacking of equally sized spheres is approximately $p \approx 0.363$ (Torquato et al., 2000). If the linear fit in Figure 29c is extrapolated to this value, it means that the maximum Young's modulus would be approximately $E_x = 2.93$ GPa.

The elastic constants of hexagonal closepacked specimens are presented in Figure 30. The Young's modulus of HCP specimens behaves linearly with respect to particle radius and porosity. The results can be compared to the theoretical value of Young's modulus derived by Wang and Mora (2008). The value calculated with Equation 2 is independent of the particle radius as both the normal and shear parallel bond spring stiffnesses are functions of r_p^3. The obtained theoretical value is $E_x = 5.843$ GPa and

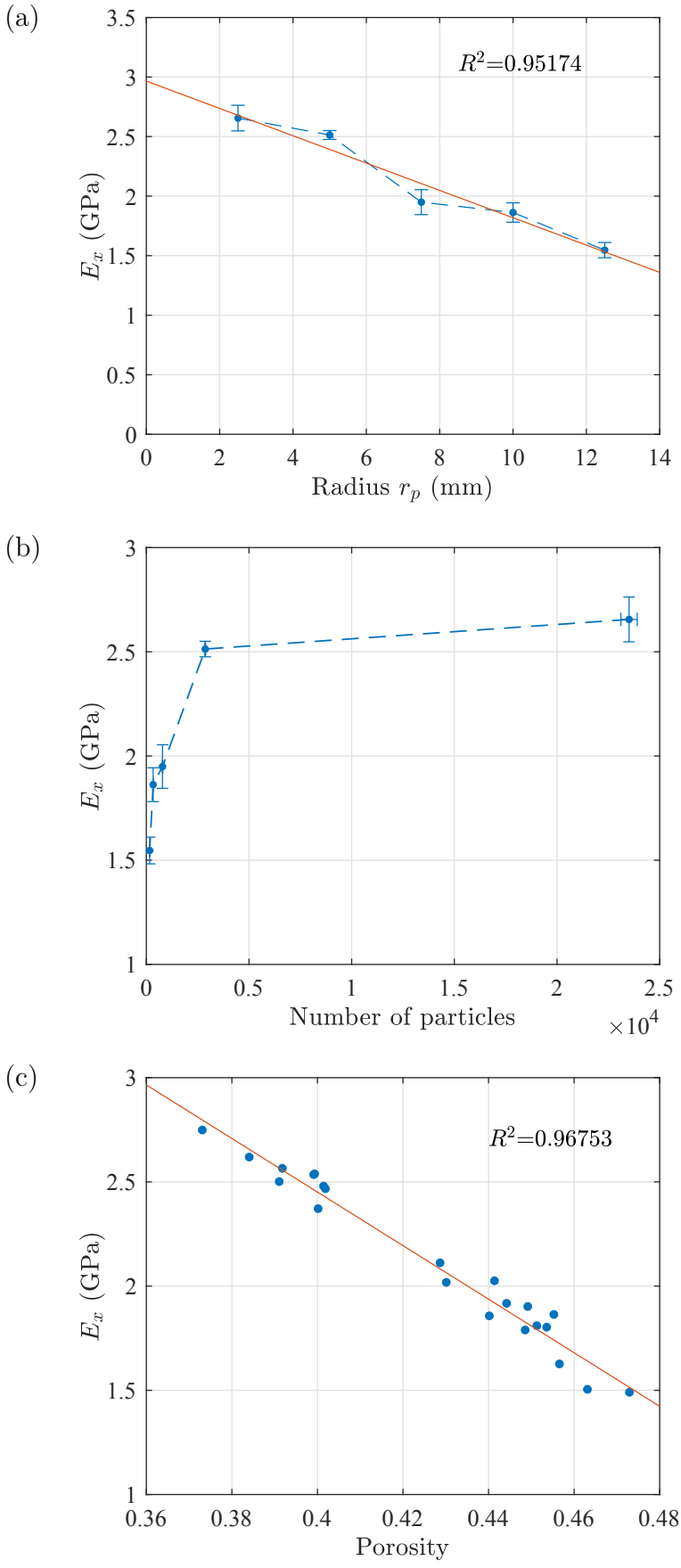

Figure 29: The Young's modulus E_x of random packings (RCP) plotted as a function of (a) particle radius, (b) number of particles and (c) specimen porosity.

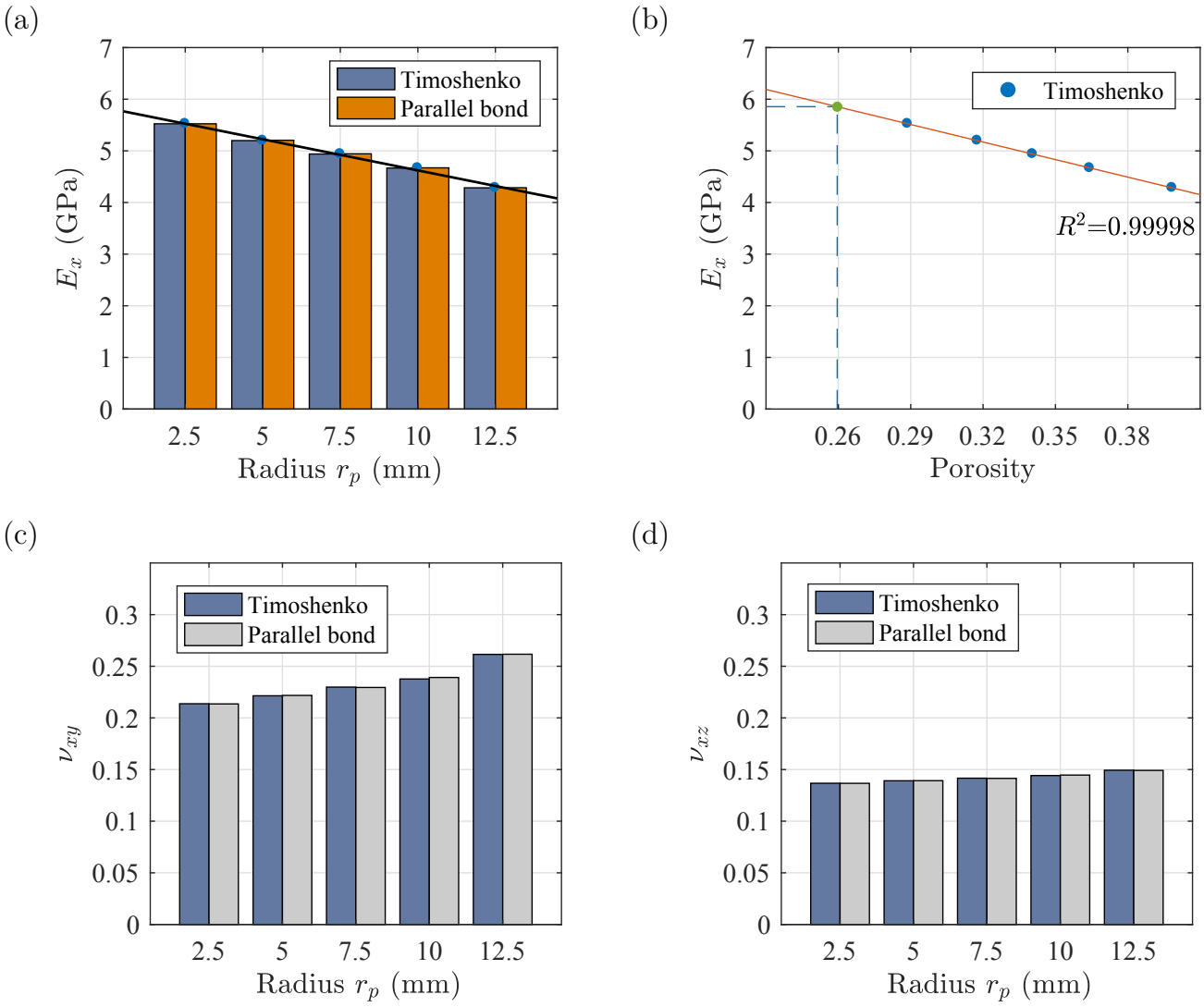

Figure 30: Results of uniaxial tests with HCP specimens. (a)-(b) Young's modulus as a function of particle radius and porosity. (c)-(d) Poisson's ratios ν_{xy} and ν_{xz} as a function of particle radius.

corresponds to a perfect hexagonal closepacking with the porosity of $p = 0.25952$. The porosity of the HCP specimens used in this study are slightly higher due to additional porosity at the specimen boundaries. If the linear fit in Figure 30b is extrapolated, the theoretical value of porosity gives a Young's modulus of $E_x = 5.855$ GPa, which is close to the result by Wang and Mora (2008) differing only by 0.21 %. In addition to the Young's modulus, the Poisson's ratios ν_{xy} and ν_{xz} of the HCP specimens with $r_p = 2.5$ mm are in good accordance with the analytical and numerical results proposed by Wang and Mora (2008).

Figure 31 shows the Poisson's ratios of RCP specimens as a function of particle radius. It can be seen that the Poisson's ratios decrease and show a converging behaviour towards a value of slightly below 0.2 as the particle radius decreases. Furthermore, the difference between ν_{xy} and ν_{xz} vanishes and the deviation between

different packings gets smaller. In other words the macroscopic behaviour of the specimens becomes more isotropic as the radius decreases and the number of particles increase.

Figures 32 and 33 show a comparison between the three packing methods. The random packings are clearly less stiff than the regular packings. Young's moduli of both RCP and HCP specimens increase linearly as the porosity decreases. The slopes of increase are roughly similar and the HCP specimens give slightly under 2 GPa stiffer moduli. The stiffness increasing effect of a HCP packing is significant. This is probably due to the higher connectivity, or average amount of bonds, per particle. It would be interesting to study the behaviour of the HCP modulus when disorder is gradually introduced to the packings. The effect of disorder or irregularity has been studied in regular 2D lattice structures (Zhu et al., 2001; Romijn and Fleck, 2007). In some lattices, such as the 2D uniform or triangular lattice, the irregularity indeed decreases significantly the Young's modulus even as the connectivity remains equal.

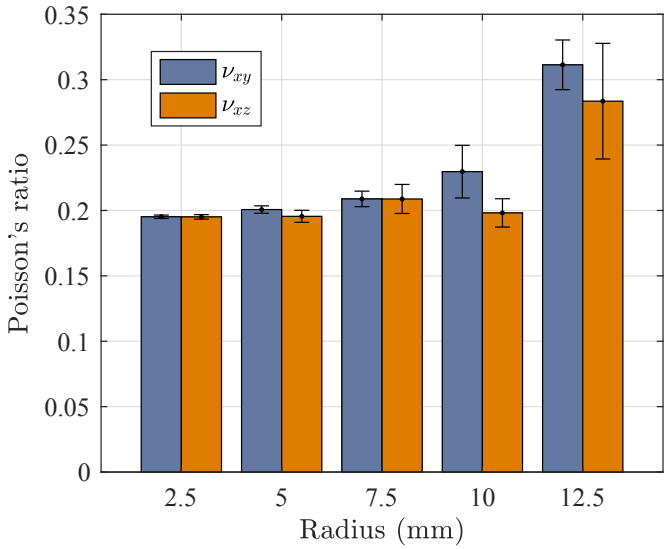

Figure 31: The Poisson's ratio of random packing specimens as a function of particle radius.

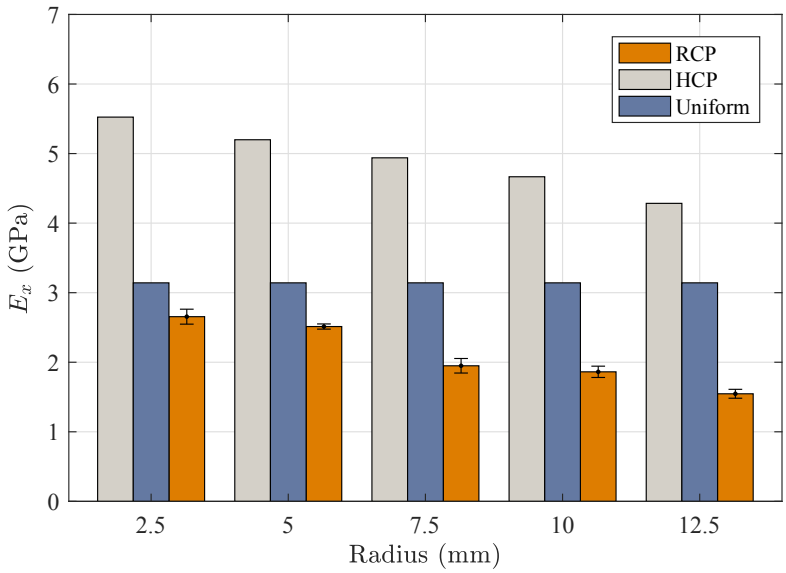

Figure 32: Comparison of Young's modulus values between different packings. Random closepacking (RCP) in orange, hexagonal closepacking (HCP) in grey and uniform packing in blue.

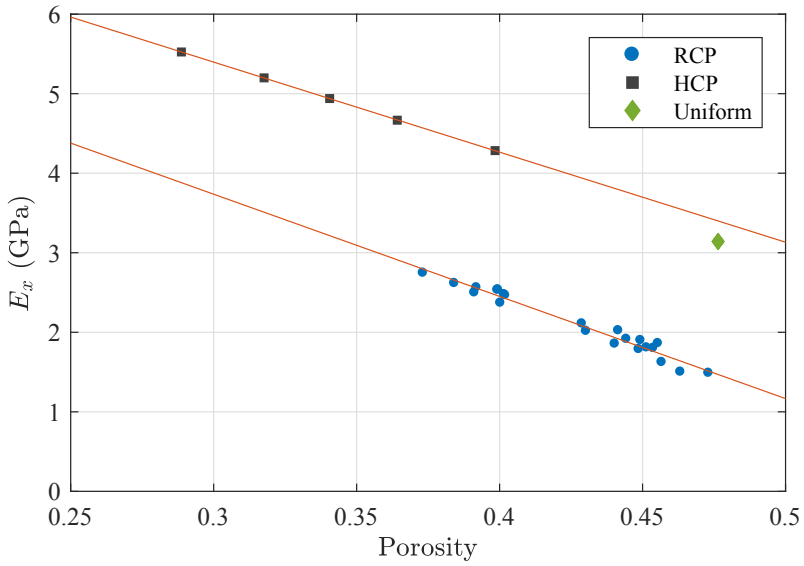

Figure 33: Young's modulus of all packings plotted as a function of porosity. The porosity of the uniform packings is constant, thus producing only one point in the plot.

5.2 Flexural tests

Three point flexural tests were carried out for the same 35 specimens that were loaded uniaxially. The results of flexural tests are presented in Figures 35 and 34. The flexural moduli obtained with Equations 67 and 69 are overall lower than the Young's modulus obtained from the uniaxial tests. The difference is emphasized especially with the uniform and hexagonal closepackings. Furthermore, there is no similar linearly decreasing trends as in the uniaxial stiffness of RCP and HCP specimens. The flexural modulus of uniform packings does not remain constant as in the uniaxial case. There is a slight decrease in the modulus as particle size decreases, which could be explained by the method of applying boundary conditions. The boundary conditions restrict the vertical translation of the corner particle shown in Figure 28. This means, that with larger particle size, more material is not allowed to tilt inside, thus having a stiffening effect on the specimen. A similar effect can partly be seen in Figure 35b with the three smallest particle sizes of the HCP specimens. The flexural moduli of random closepacked specimens are closest to the Young's moduli obtained from compression tests. By taking into account the distribution of the load, the stiffness decreases especially with the larger particle sizes. If the load is considered as a point load, the deflection obtained from the simulations is an underestimation. However, the correction of Equation 69 does not change the overall trend of the flexural stiffness values.

When comparing the top and bottom midspan displacements, it was noticed that the beams were compressed in the loading direction. For comparison the flexural moduli were also calculated from only the bottom deflection, thus neglecting this deformation. The results from Figure 35 show that the moduli increased 4.3-13 % from the moduli obtained with the average deflection. The increase was larger with small particle sizes.

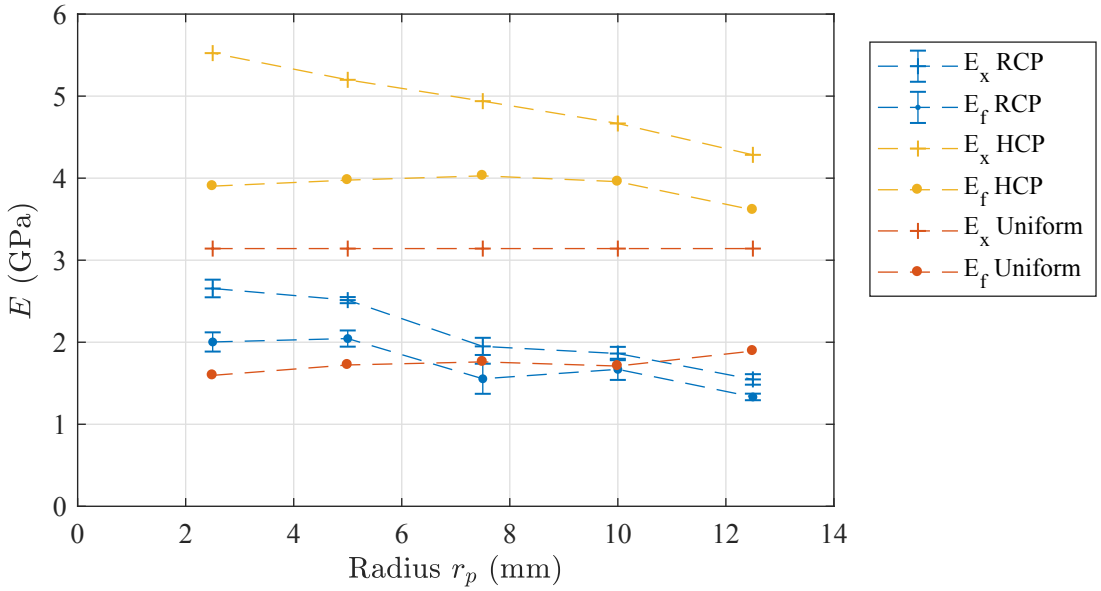

Figure 34: Comparison between the axial and flexural moduli.

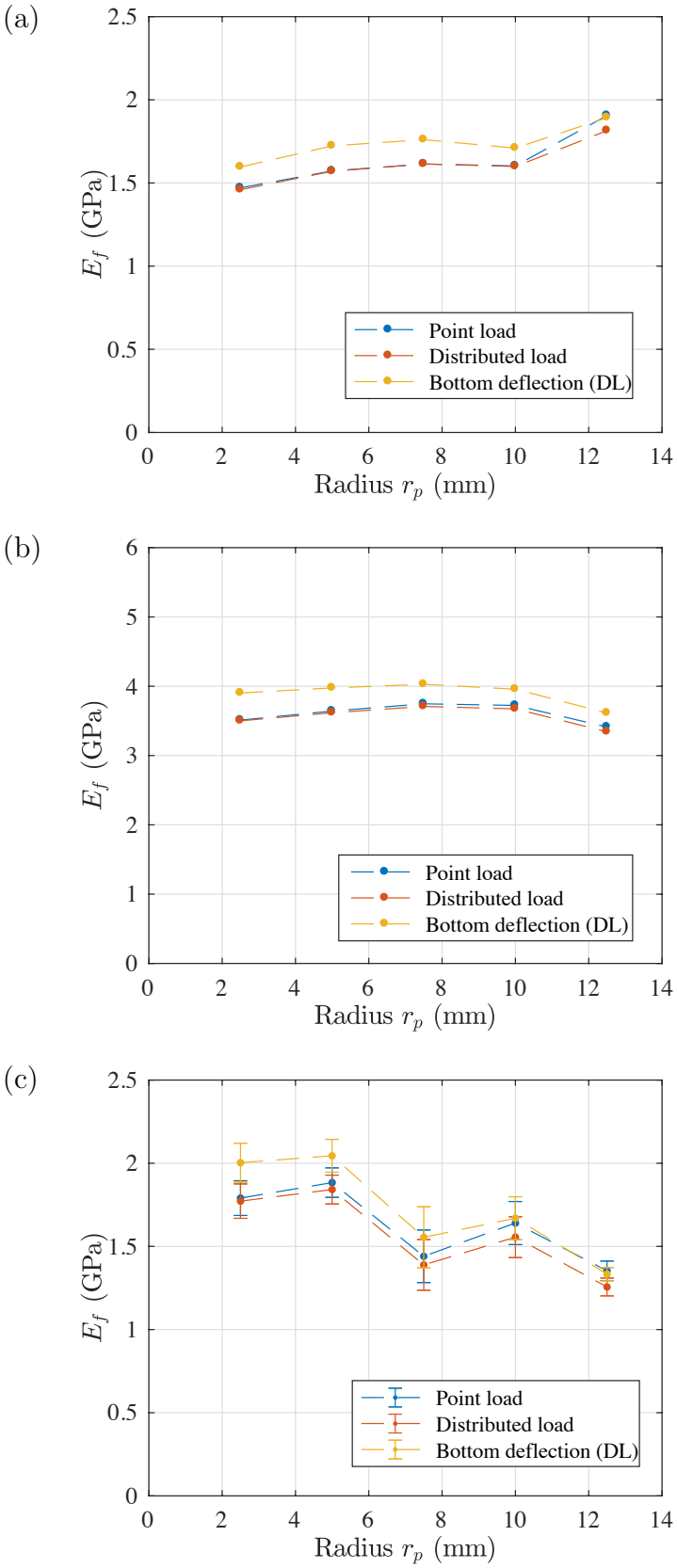

Figure 35: The flexural modulus E_f of (a) uniform packings, (b) HCP and (c) RCP plotted as a function of particle radius. For comparison, the modulus is calculated with three methods. The Point load and Distributed load curves take the deflection as an average of the top and bottom surface deflections but consider the applied load differently. In the Bottom deflection curve the deflection is taken from the bottom surface and the load is considered as a distributed load (DL).

5.3 Stress analysis

One of the main objectives of the this study was to simulate the elastic behaviour of a discretized continuum specimen. The elastic constants, obtained from the uniaxial and flexural tests, describe the behaviour of the specimen on a macroscopic level. However, no information is obtained from the microscopic behaviour. Possible stress peaks that can initiate microcracks are not noticed. In this section, the stress state in loaded specimens is visualized and analyzed by different means. The method described in section 3.7 is used to calculate stresses in individual particles and representative volume elements.

5.3.1 Stress state in compression

For the uniaxial stress analysis, each specimen is loaded by compressing the loaded end by 0.01 μm. The displacement is selected to be low in order to keep the simulation times reasonable but nevertheless so that dynamic effects at the beginning of the simulation have dampened and a quasistatic state is achieved.

The uniformity of the stress state is analyzed by dividing the specimen into 15 subvolumes and by calculating the average normal stresses in x-direction in these subvolumes. Furthermore, the distribution of normal stresses in individual particles is represented as histograms. The average stress in the specimen is calculated from the particle stresses by treating the entire specimen as a representative volume. The obtained stress tensor is compared to the continuum stress calculated from the uniaxial load recorded at the loading end of the specimen. The results of this comparison are presented in Tables 5 and 6.

From Tables 5 and 6 it can be seen that the average stresses obtained with the representative volume method are in good agreement with the corresponding continuum stresses. The difference decreases almost linearly as the particle size gets smaller and for $r_p = 2.5$ mm it is under 0.4% for all the packings. In addition to the normal stress σ_{xx}, there are some normal stresses in the y- and z-directions and shear stresses generated during the loading. Table 7 shows the average stress tensors in representative random packings for each particle size. It can be seen that the other stress components are small compared to the normal stress in the loading direction.

Table 5: Comparison betweeen the average normal stresses in RCP specimens obtained either by the RVE method or from the boundary load.

r_p (mm)	σ_{xx}^{RVE} (Pa)	σ_{xx}^{C} (Pa)	Difference (%)
2.5	-106.1	-106.5	0.36
5.0	-104.8	-105.6	0.72
7.5	-82.7	-83.7	1.22
10.0	-80.7	-82.1	1.64
12.5	-68.5	-70.2	2.51

Furthermore, the proportional part of these stress components decreases as particle size decreases. In addition, Table 7 shows that stress tensors are symmetric.

Figures 36 and 37 present the distribution of normal stresses σ_{xx} at a particle level and in 15 subvolumes in the xy-plane. From Figure 36 it can be seen that the distribution of particle stresses resembles a normal distribution with all particle sizes. The most highly loaded particles have a stress of approximately 2.5 to 3 times the average stress in all the cases. However, there are relatively more highly stressed particles in specimens with larger particle sizes. This is seen as an increase in the standard deviations of the distributions. Furthermore, with larger particle sizes the distribution is more irregular and there is more variance between the five random packings. The increase in standard deviation suggests that once the critical limit of initiation of microcracks is achieved, relatively more microcracks are initiated in specimens with larger particle sizes.

Figure 37 presents representative stress distributions of each particle size. One common trait for all these distributions is that the stresses in the middle of the specimen are higher than in the borders. This means that more load is carried through the middle part. As the particle radius decreases the effect of the boundaries becomes smaller and the distribution more uniform. Furthermore, the average stresses increase with decreasing particle radius as the specimens become stiffer.

5.3.2 Stress state in bending

The normal stress distribution in bent RCP specimens are presented in Figure 38 as representative cases for each particle size. The specimens are divided into 5 or 7 horizontal subvolumes and the average normal stress is calculated inside these volumes. The average tensile stress in the bottom part tends be higher than the

Table 6: Comparison betweeen the average normal stresses in the uniform and HCP specimens obtained either by the RVE method or from the boundary load.

	r_p (mm)	σ_{xx}^{RVE} (Pa)	σ_{xx}^{C} (Pa)	Difference (%)
Uniform	2.5	-128.6	-128.2	0.27
	5.0	-131.1	-131.8	0.54
	7.5	-131.0	-132.0	0.76
	10.0	-131.0	-132.4	1.06
	12.5	-139.8	-141.7	1.34
HCP	2.5	-223.8	-223.3	0.24
	5.0	-212.8	-213.9	0.50
	7.5	-200.0	-201.5	0.75
	10.0	-187.2	-189.1	1.01
	12.5	-181.0	-183.5	1.32

Table 7: Stress tensors of RCP specimens under compression. The tensors are calculated as average from stresses of individual particles by using Equation 54. Stress tensors fulfill well the requirement of symmetry. The proportional part of the σ_{22}, σ_{33} and shear components decreases as particle size decreases. The stress state becomes clearly uniaxial as excpected under a uniaxial load.

$r_p = 12.5$ mm	$r_p = 10$ mm
$\sigma_{ij} = \begin{bmatrix} -65.443 & -0.167 & -0.069 \\ -0.169 & -0.452 & 0.009 \\ -0.067 & 0.009 & -0.442 \end{bmatrix} [Pa]$	$\sigma_{ij} = \begin{bmatrix} -77.390 & 0.076 & 0.061 \\ 0.076 & -0.292 & 0.005 \\ 0.061 & 0.005 & -0.270 \end{bmatrix} [Pa]$
$r_p = 7.5$ mm	$r_p = 5$ mm
$\sigma_{ij} = \begin{bmatrix} -81.085 & -0.009 & -0.065 \\ -0.009 & -0.203 & 0.005 \\ 0.065 & 0.005 & -0.214 \end{bmatrix} [Pa]$	$\sigma_{ij} = \begin{bmatrix} -103.19 & -0.006 & -0.005 \\ -0.006 & -0.147 & 0.003 \\ -0.005 & 0.003 & -0.146 \end{bmatrix} [Pa]$
$r_p = 2.5$ mm	
$\sigma_{ij} = \begin{bmatrix} -106.78 & 0.0004 & -0.0001 \\ 0.0004 & -0.074 & 0.0001 \\ -0.0001 & 0.0001 & -0.074 \end{bmatrix} [Pa]$	

compressive stress in the corresponding top part. Furthermore, the stresses in the outermost subvolumes increase as particle size decreases. This is probably due to the increasing average distance between the neutral axis and the centroids of the particles in the outermost subvolume.

Figure 39 shows the stresses in a RCP specimen with particle radius $r_p = 5$ mm under a three-point flexural load. It is a representative case of the particle scale load distribution in bent specimens. The most highly stressed particles are naturally on the top and bottom surfaces. The particles in the middle near the neutral axis are on the other hand under low stresses. Contrary to the average normal stress, the most stressed particles are on the top surface. Figure 39 shows that the curvature of the top and bottom surfaces are different. The curvature is large on the midspan of the top surface, which probably causes the high stresses. On the other hand the curvature is more constant on the lower surface, thus giving a higher average stress as shown in Figure 38.

By visually analyzing Figure 39, several chains of highly stressed particles can be noticed on both top and bottom surfaces. These can be categorized as force chains that are defined as chains of more than 3 particles with stresses higher than the average and "lined up" in a sufficiently linear manner (Peters et al., 2005).

5.4 Comparison between the bond models

Two bond models, the spring-based parallel bond model and the Timoshenko beam model, were implemented in the BPM. Eventhough, these bond models are based on different mechanical elements their behaviours are fairly similar. The definition of the parallel bond normal stiffness in chapter 4.2 leads to identical axial behaviour. Here, the effect of the bond type on the simulation results is discussed.

From Figure 30 and it can be seen that the results obtained with the uniaxial compression tests are almost identical with both bond models. The flexural moduli E_f values differ slightly particularly with the larger particle size. The Timoshenko beam model gives in average 2.3 % larger values with the $r_p = 12.5$ mm RCP specimens. The difference dercreases with decreasing particle size and for the specimens with $r_p = 5$ mm the Timoshenko values are only 0.39 % larger than the parallel bond values. Contrary to the RCP specimens the uniformly packed specimens give slightly smaller E_f values (approximately 0.3 to 0.5 %) with the Timoshenko model.

Alltogether, the results obtained with the two models are very close to each other and the differences appear to decrease with smaller particle sizes. This suggests that the bond type does not affect significantly the macroscopic elastic behaviour when the bond parameters are calibrated. In other words, the bond type does not affect the Poisson's ratios or flexural modulus when it is calibrated to produce similar uniaxial Young's modulus. The most significant downside of the Timoshenko beam model is the longer computational time that it requires. The simulation times were roughly twice longer than with the parallel bond model. The difference is emphasized with larger particle numbers, which is why flexural test with Timoshenko beam model were not conducted for specimens with the smallest particle size.

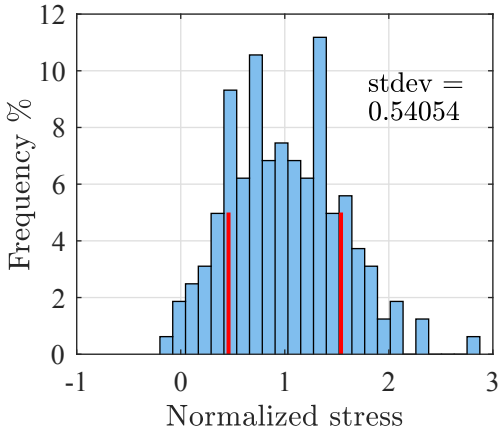

(a) $r_p = 12.5$ mm

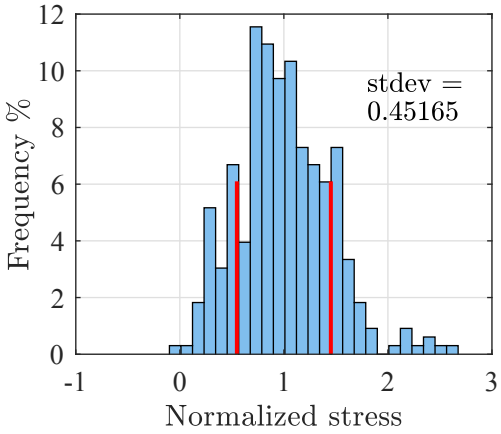

(b) $r_p = 10$ mm

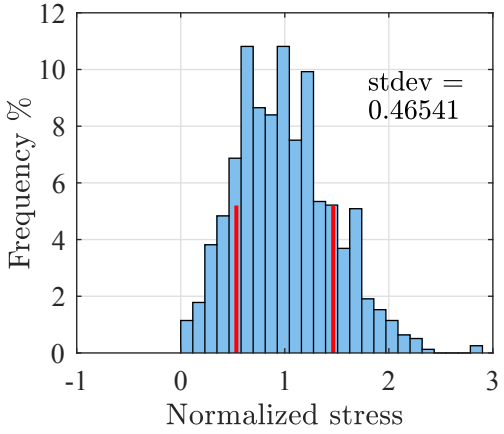

(c) $r_p = 7.5$ mm

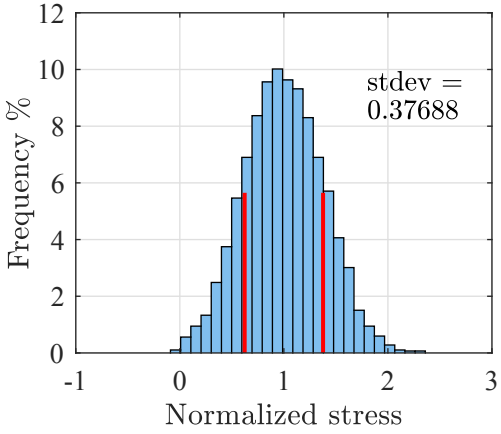

(d) $r_p = 5$ mm

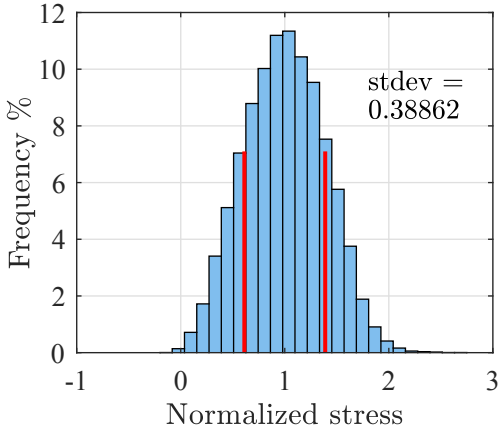

(e) $r_p = 2.5$ mm

Figure 36: The distribution of normal stresses σ_{xx} in RCP specimens under compression. The stresses are normalized with the mean normal stress σ_{xx}^{mean}. The red lines represent the standard deviations. The distribution is more irregular and has a larger deviation in specimens with larger particle size.

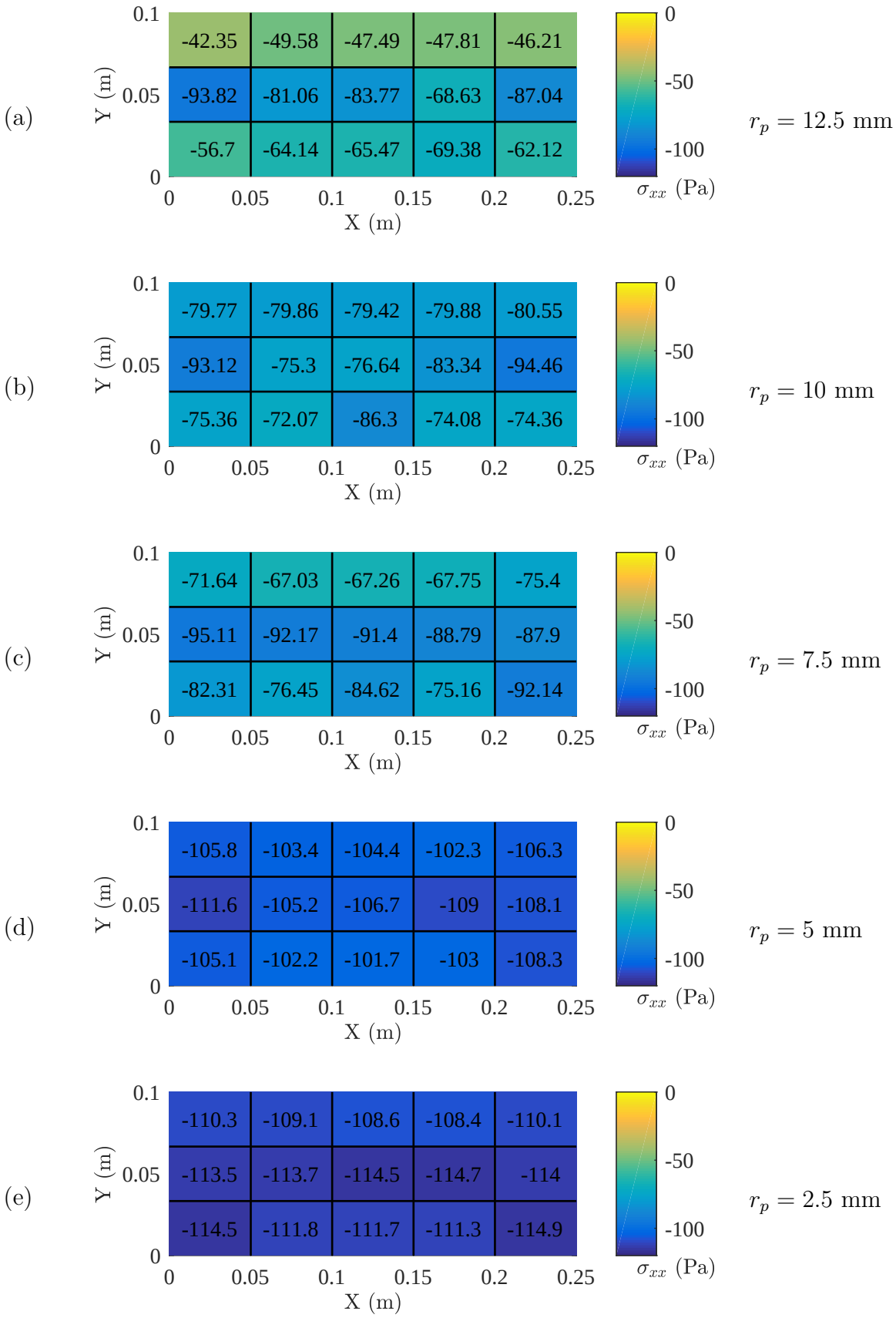

Figure 37: Normal stress distribution in the xy-plane of RCP specimens under compression. The specimens are divided into 15 subvolumes in which the average stresses are calculated.

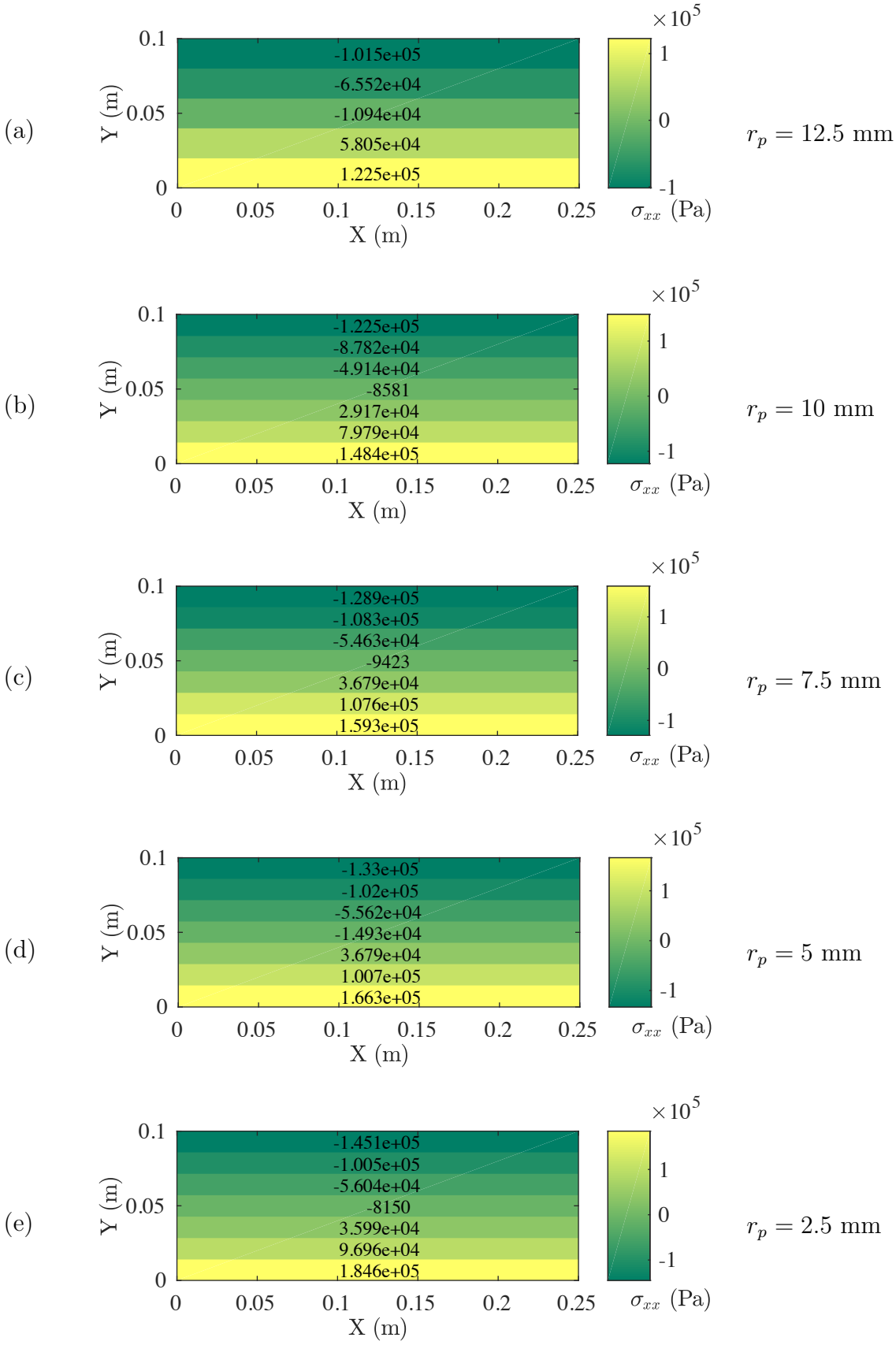

Figure 38: Normal stress distribution in the xy-plane of RCP specimens under flexural loading. The average stresses are calculated in 5 or 7 horizontal layers.

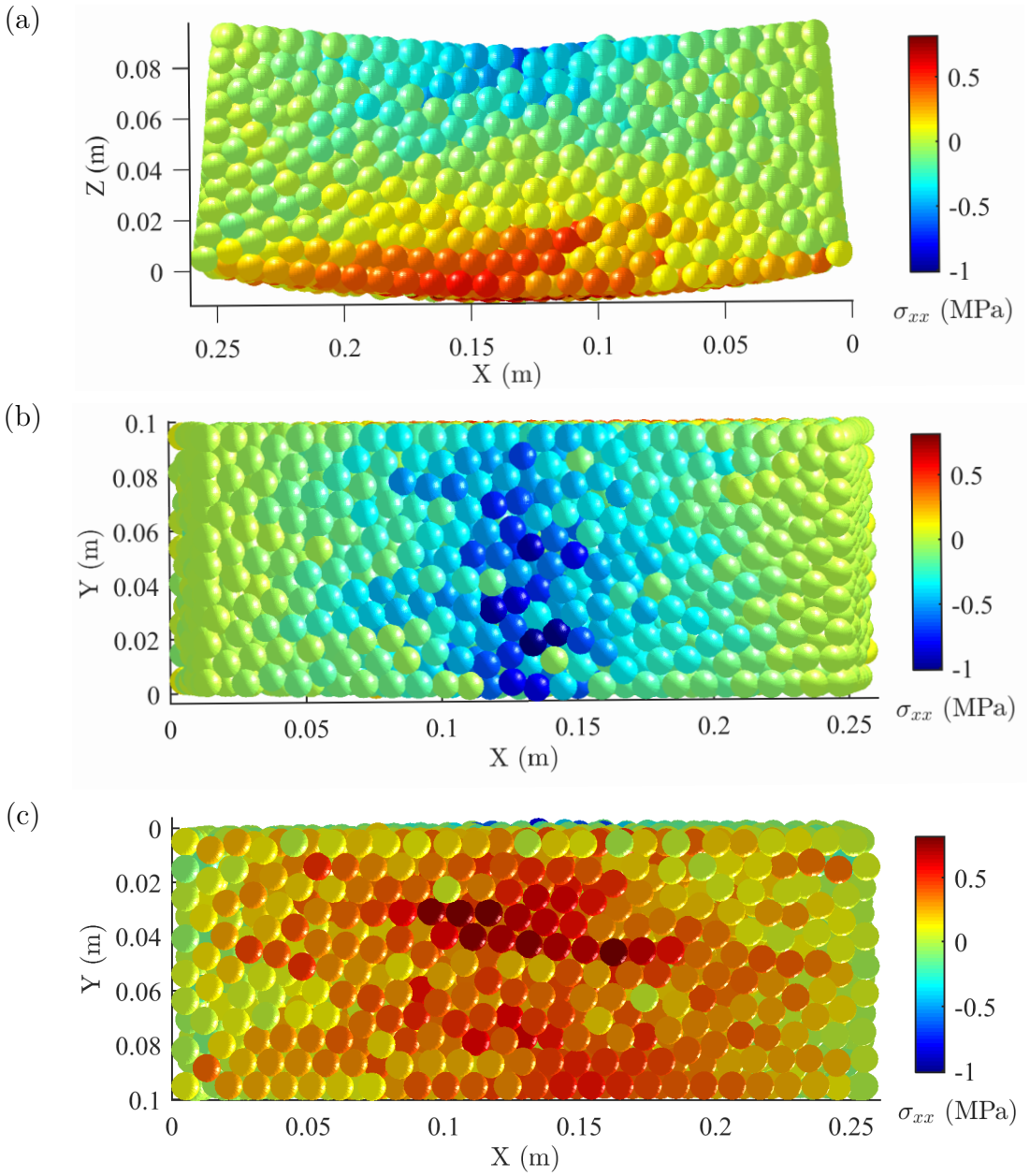

Figure 39: (a) A RCP specimen with particle radius $r_p = 5$ mm under a 3-point flexural load of 1 kN. The deformation is magnified with a factor of 500. (b) Top view of the specimen: several highly stressed particle chains can be observed. (c) Bottom view of the specimen: the most stressed particles are concentrated in one or two chains.

6 Conclusions

The main objective of this thesis was to develop a three-dimensional bonded particle model and implement the model in MATLAB. The model was developed with a goal to simulate the elastic behaviour of a continuum, while acknowledging the future objective of simulating breakage of sea ice. Furthermore, the parameter sensitivity of the model was studied by varying the particle size. Additionally, the effects of the bond model and particle packing method were studied. Two bond models, the spring based parallel bond model and Timoshenko beam model, were implemented in the BPM. The three sphere packing methods used in this study were uniform or cubic packing, hexagonal closepacking and random closepacking.

In total 35 test specimens of 0.25 x 0.1 x 0.1 m were generated with 5 different particle sizes. These specimens were tested under strain controlled uniaxial tension and compression in order to obtain the macroscopic Young's modulus and Poisson's ratio. The normal to shear spring stiffness ratio of the parallel bond was calibrated against the Timoshenko beam model with a uniaxial compression test of a random closepacked specimen with a particle radius of 10 mm. In addition to uniaxial tests, three point flexural tests were conducted to obtain the flexural stiffness of the specimens. The microscopic behavior of the specimens was studied by analyzing the stress state at a particle scale of the loaded specimens.

The tensile and compressive tests produced identical results for the Young's moduli and Poisson's ratios. This result was expected and it verifies that the model behaves correctly in both directions. The uniform packings produced constant stiffness values and did not deform laterally during the uniaxial tests. The compression test results of both hexagonal and random closepacked specimens suggest that the Young's modulus increases linearly as the porosity of the specimens decreases. Additionally, the Poisson's ratios of RCP specimens converge and the differences in lateral directions vanish as the number of particles is increased.

The flexural stiffness was lower than the uniaxial stiffness for all the tested specimens. There was no clear dependence between the flexural stiffness and particle radius or specimen porosity. The stress distributions in bent specimens were slightly asymmetric, showing larger average tensile stresses in the bottom of the beams than average compressive stresses in the top of the beams. However, the maximum stresses at particle scale occured on the top surface. This is due to different deformation curvatures on the top and bottom surfaces. Visual analysis of stresses at a particle scale in bent specimens showed clear force chains carrying more than the average load.

Comparison between the parallel bond and Timoshenko beam model showed that the bond type did not have significant effect on the macroscopic Poisson's ratios or flexural modulus, when the parameters of the parallel bond were calibrated to produce similar uniaxial stiffness. The Timoshenko beam model showed slightly larger flexural stiffness values for the RCP specimens. However, the notable differences in the macroscopic properties rather emerged from the packing geometry of the specimens.

The results suggest that if an isotropic material response and a uniform stress

distribution is desired, a great number of particles is needed to discretize a small material volume. This can be seen from Figures 31 and 37. A great amount of particles lead to very time-consuming simulations, as was the case with the flexural loading of the $r_p = 2.5$ mm specimens. However, if the effects, such as fracture or wear, are localized in a small part of the structure, a coupled discrete-continuum method should be considered to reduce the simulation time.

A natural follow-up to this work is the implementation and verification of a bond failure model. The failure model can be either brittle or a softening function can be applied. Both these models require calculation of stresses in the bonds. This can be done by utilizing beam theory equations. Additionally, when the failure of bonds is enabled, another contact model has to be implemented to work alongside with the parallel bond model or Timoshenko beam model. This model can be based on the simple spring model described in Equation 12 or a Hertz-Mindlin contact model, that has been extensively used in granular DEM codes, could be the choice.

In the following development of the model, the microstructure of sea ice should be taken into account. One of the most common sea ice types is columnar sea ice which has anisotropic mechanical properties and weak planes between the columns. These features have not yet been considered in earlier DEM studies of modelling sea ice. A potential solution to this is the use of particle clusters and several bond types and stiffnesses to mimic the ice columns or large ice crystals.

References

André, D., Iordanoff, I., Charles, J.-l., and Néauport, J. (2012). Discrete element method to simulate continuous material by using the cohesive beam model. *Computer Methods in Applied Mechanics and Engineering*, 213:113–125.

Bagi, K. (2005). An algorithm to generate random dense arrangements for discrete element simulations of granular assemblies. *Granular Matter*, 7(1):31–43.

Belytschko, T., Liu, W. K., and Moran, B. (2000). Nonlinear finite elements for continua and structures.

Brown, N. J., Chen, J.-F., and Ooi, J. Y. (2014). A bond model for dem simulation of cementitious materials and deformable structures. *Granular Matter*, 16(3):299–311.

Chen, G., Schott, D. L., and Lodewijks, G. (2016). Tensile test simulation of high-carbon steel by discrete element method. *Engineering Computations*, 33(4):1224–1245.

Cho, N. a., Martin, C., and Sego, D. (2007). A clumped particle model for rock. *International Journal of Rock Mechanics and Mining Sciences*, 44(7):997–1010.

Cundall, P. (1987). Distinct element models of rock and soil structure. *Analytical and Computational Methods in Engineering Rock Mechanics.*, pages 129–163.

Cundall, P. A. and Strack, O. D. (1979). A discrete numerical model for granular assemblies. *Geotechnique*, 29(1):47–65.

Ergenzinger, C., Seifried, R., and Eberhard, P. (2011). A discrete element model to describe failure of strong rock in uniaxial compression. *Granular Matter*, 13(4):341–364.

Fakhimi, A. and Villegas, T. (2007). Application of dimensional analysis in calibration of a discrete element model for rock deformation and fracture. *Rock Mechanics and Rock Engineering*, 40(2):193–211.

Fries, L., Antonyuk, S., Heinrich, S., and Palzer, S. (2011). Dem–cfd modeling of a fluidized bed spray granulator. *Chemical Engineering Science*, 66(11):2340–2355.

GiD (2016). *Reference Manual*. International Center for Numerical Methods in Engineering (CIMNE), Barcelona.

Gully, A., Lin, J., Cherkaev, E., and Golden, K. M. (2015). Bounds on the complex permittivity of polycrystalline materials by analytic continuation. In *Proc. R. Soc. A*, volume 471, page 20140702. The Royal Society.

Hentz, S., Daudeville, L., and Donzé, F. V. (2004). Identification and validation of a discrete element model for concrete. *Journal of engineering mechanics*, 130(6):709–719.

Hopkins, M. A. (1992). Numerical simulation of systems of multitudinous polygonal blocks. Technical report, DTIC Document.

Ji, S., Di, S., and Long, X. (2016). Dem simulation of uniaxial compressive and flexural strength of sea ice: Parametric study. *Journal of Engineering Mechanics*, 143(1):C4016010.

Jirásek, M. and Bažant, Z. P. (1995). Particle model for quasibrittle fracture and application to sea ice. *Journal of engineering mechanics*, 121(9):1016–1025.

Khattak, M. J. and Khattab, A. (2013). Modeling tensile response of fiber-reinforced polymer composites using discrete element method. *Polymer Composites*, 34(6):877–886.

Labra, C. and Onate, E. (2009). High-density sphere packing for discrete element method simulations. *International Journal for Numerical Methods in Biomedical Engineering*, 25(7):837–849.

Li, X. and Wan, K. (2011). A bridging scale method for granular materials with discrete particle assembly–cosserat continuum modeling. *Computers and Geotechnics*, 38(8):1052–1068.

MathWorks (2017). Matlab. https://se.mathworks.com/products/matlab.html. Accessed 2017-28-04.

Nemat-Nasser, S. (1999). Averaging theorems in finite deformation plasticity. *Mechanics of Materials*, 31(8):493–523.

O'Sullivan, C. (2011). *Particulate discrete element modelling.* Spon Press, Milton Park, Abingdon, Oxon, UK.

O'Sullivan, C. and Bray, J. D. (2004). Selecting a suitable time step for discrete element simulations that use the central difference time integration scheme. *Engineering Computations*, 21(2/3/4):278–303.

Ouadfel, H. and Rothenburg, L. (1999). An algorithm for detecting inter-ellipsoid contacts. *Computers and geotechnics*, 24(4):245–263.

Paavilainen, J., Tuhkuri, J., and Polojärvi, A. (2011). 2d numerical simulations of ice rubble formation process against an inclined structure. *Cold Regions Science and Technology*, 68(1):20–34.

Peters, J., Muthuswamy, M., Wibowo, J., and Tordesillas, A. (2005). Characterization of force chains in granular material. *Physical review E*, 72(4):041307.

Potapov, S., Masurel, A., Marin, P., and Daudeville, L. (2016). Mixed dem/fem modeling of advanced damage in reinforced concrete structures. *Journal of Engineering Mechanics*, 143(2):04016110.

Potyondy, D. and Cundall, P. (2004). A bonded-particle model for rock. *International journal of rock mechanics and mining sciences*, 41(8):1329–1364.

Przemieniecki, J. S. (1968). *Theory of matrix structural analysis*. McGraw-Hill, New York.

Romijn, N. E. and Fleck, N. A. (2007). The fracture toughness of planar lattices: imperfection sensitivity. *Journal of the Mechanics and Physics of Solids*, 55(12):2538–2564.

Schlangen, E. and Garboczi, E. (1996). New method for simulating fracture using an elastically uniform random geometry lattice. *International journal of engineering science*, 34(10):1131–1144.

Schneider, B., Bischoff, M., and Ramm, E. (2010). Modeling of material failure by the discrete element method. *PAMM*, 10(1):685–688.

Selvadurai, A. and Sepehr, K. (1999). Two-dimensional discrete element simulations ofice–structure interaction. *International Journal of Solids and Structures*, 36(31):4919–4940.

Tavarez, F. A. and Plesha, M. E. (2007). Discrete element method for modelling solid and particulate materials. *International Journal for Numerical Methods in Engineering*, 70(4):379–404.

Teufelsbauer, H., Wang, Y., Chiou, M. C., and Wu, W. (2009). Flow–obstacle interaction in rapid granular avalanches: Dem simulation and comparison with experiment. *Granular Matter*, 11(4):209–220.

Timco, G. and Weeks, W. (2010). A review of the engineering properties of sea ice. *Cold Regions Science and Technology*, 60(2):107–129.

Timoshenko, S. P. and Gere, J. M. (1972). *Mechanics of Materials*. Van Norstrand Reinhold Company, New York, NY.

Torquato, S., Truskett, T. M., and Debenedetti, P. G. (2000). Is random close packing of spheres well defined? *Physical review letters*, 84(10):2064.

Tsuji, Y., Tanaka, T., and Ishida, T. (1992). Lagrangian numerical simulation of plug flow of cohesionless particles in a horizontal pipe. *Powder technology*, 71(3):239–250.

Wagner, G. J. and Liu, W. K. (2003). Coupling of atomistic and continuum simulations using a bridging scale decomposition. *Journal of Computational Physics*, 190(1):249–274.

Wang, C. M. (1995). Timoshenko beam-bending solutions in terms of euler-bernoulli solutions. *Journal of engineering mechanics*, 121(6):763–765.

Wang, Y. and Mora, P. (2008). Macroscopic elastic properties of regular lattices. *Journal of the Mechanics and Physics of Solids*, 56(12):3459–3474.

Wolff, M., Salikov, V., Antonyuk, S., Heinrich, S., and Schneider, G. (2013). Three-dimensional discrete element modeling of micromechanical bending tests of ceramic–polymer composite materials. *Powder technology*, 248:77–83.

Yang, D., Ye, J., Tan, Y., and Sheng, Y. (2011). Modeling progressive delamination of laminated composites by discrete element method. *Computational Materials Science*, 50(3):858–864.

Zhu, H., Hobdell, J., and Windle, A. (2001). Effects of cell irregularity on the elastic properties of 2d voronoi honeycombs. *Journal of the Mechanics and Physics of Solids*, 49(4):857–870.

A MATLAB script for running a BPM simulation

```
%% This is the main file for BPM

% r = particle radius
% p = random packing index
% dt = time step
% lim = simulation limit
% o = packing option
% bond = bond type
% test = tensile (compressive) or bending
% ramp = number of steps in the loading ramp
% plotting = plot option

function [d,b,x_init,F,ds] = testbpm(r,p,dt,lim,o,bond,test,ramp,plotting)
tic;

% Material properties
rho = 925; % Continuum density (kg/m^3)

% Specimen size and particle packing
w = 0.25; l = 0.1; h = 0.1; % width, length, height in meters
packing = o; % uniform, closepacked (hcp) or random packing from file

% Simulation parameters
limit = dt*lim; % simulation limit
failure = 0; % 0=bond failure not allowed, 1=bonds can fail
speed = 0.00001; % pulling/pushing speed

% Class constructor
b = bpm(r,rho,[0 0 0],packing,w,l,h,p);
[b] = end_particles(b,packing); % Selecting end particles
[b] = initial(b,dt,test,packing,speed,ramp);
[b] = inertia_tensor(b);

% Variables for plotting/assistive variables
t = 0;slip = zeros(size(b.c,1),1);Fs2 = zeros(size(b.c,1),3);
v = [];v2 = [];time = [];Ek = [];Es = [];Ed = [];Eext = [];
Esum = [];ds = [];x_init = b.x;dy2 = 0;dz2 = 0;ex = 0;steps = 0;
Fext = b.Fext;n = 1;

if strcmp(test,'Tensile')
    [b,dy,dz,ex] = poisson(b,t,dy2,dz2,speed,ex,packing);
    dy2 = dy;
    dz2 = dz;
end

% Simulation loop started
while t < limit
    b.Ek = 0;b.Es = 0; % Reseting kinetic and strain energies
    F = 0; % Reseting measured load in x-direction

    if strcmp(bond,'pb') % Selecting contact model
        [b,slip,Fs2] = parallel_bond(b,slip,Fs2,test,failure);
    else
```

```
        [b] = timoshenko(b,packing);
    end

    [b] = verlet(b,test); % Explicit time integration

    time = [time;t];
    t = t + b.dt;
    steps = steps + 1;
    disp(steps);

    if strcmp(test,'Tensile')% Measuring load and calculating Poisson's ratio
        for j =1:size(b.ends,1)
            i = b.ends(j);
            if b.x(i,1) < b.width/2
                F = F + b.F(i,1);
            end
        end
        [b,dy,dz,ex] = poisson(b,t,dy2,dz2,speed,ex,packing);
    end

    if strcmp(test,'Bend') % Increasing bending load
        S = sum(b.Fext);
        if  abs(S(1,3)) < 1000
            b.Fext = Fext*(steps+1);
        end
    end

    if strcmp(test,'Bend') % Recording plotting variables
        v = [v;b.x(b.loaded(1),3)];
        v2 = [v2;b.v(b.loaded(1),3)];
    else
        v = [v;F];
        v2 = [v2;b.nu_xy];
    end

    x_diff = abs(b.x - x_init);
    d = deflection(b,x_diff); % Calculating deflection
    ds = [ds;d];

    if strcmp(plotting,'energy1')
        Ek = [Ek;b.Ek];
        Es = [Es;sum(b.Es)];
        Ed = [Ed;b.Ed];
        Eext = [Eext;-b.Eext];
        Esum = [Esum;(b.Ek+sum(b.Es)+b.Ed-b.Eext)];
    end
    if strcmp(plotting,'energy2')
        Ek = [Ek;b.Es(1,1)];
        Es = [Es;b.Es(1,2)];
        Ed = [Ed;b.Es(1,3)];
        Eext = [Eext;b.Es(1,4)];
        Esum = [Esum;sum(b.Es)];
    end
end
```

```
[b] = stresses(b,packing,test); % Calculating stresses

c = [1 0 0]; % color of particles, [red green blue]
fig = figure(1); hold on;
set(fig,'renderer','opengl');
set(gca,'Units','Centimeters','Position',[1.1,1.2,6,5]);
set(gcf,'Units','Centimeters','Position',[0,0,8,7]);
fig.PaperPositionMode = 'auto';

b.bpmplot(c,20,'light'); % Plotting the loaded specimen

xlabel('X (m)');ylabel('Y (m)');zlabel('Z (m)');
xlabh = get(gca, 'XLabel');
set(xlabh,'Position', get(xlabh,'Position') + [0 0.15 0]);
set(get(gca,
'YLabel'),'FontUnits','points','interpreter','latex','fontsize',10.5,'FontNam
e','Times');
set(get(gca,
'ZLabel'),'FontUnits','points','interpreter','latex','fontsize',10.5,'FontNam
e','Times');
set(gca,'fontsize',10.5,'FontName','Times');
campos([10 5 5]);
axis equal;
axis tight;
hold off;

% Plotting force-displacement
figure(2); hold on; grid on; box on;
if strcmp(plotting,'tensile')
    yyaxis left
    xlabel('dL (m)')
    ylabel('F (N)')
    plot(time.*speed,v);
    yyaxis right
    ylabel('Poisson''s ratio')
    plot(time.*speed,v2);
end

% Plotting deflection-time
if strcmp(plotting,'bend')
    yyaxis left
    xlabel('Time (s)')
    ylabel('z-pos')
    plot(time,v);
    yyaxis right
    ylabel('v_z')
    plot(time,v2);
end

% Plotting energy breakdown
if strcmp(plotting,'energy1') || strcmp(plotting,'energy1')
    ylabel('Energy (J)')
    plot(time,Esum,'Color','b','LineStyle','-','DisplayName','Total');
    plot(time,Ek,'Color','r','LineStyle','-','DisplayName','Kinetic');
    plot(time,Es,'Color','g','LineStyle','-','DisplayName','Spring');
    plot(time,Ed,'Color','k','LineStyle','-','DisplayName','Damping');
```

```
    plot(time,Eext,'Color','m','LineStyle','-','DisplayName','External
work','markersize',0.0001);
    legend('show');
end

toc; hold off;
```

```
%% This is a function for calculating the interparticle forces
%% according the parallel bond model

function [b,slip,Fs2] = parallel_bond(b,slip,Fs2,test,failure)

sz = size(b.c,1); % number of bonded sphere pairs

for n = 1:sz

    % Bonded speheres i and j
    i = b.c(n,1);
    j = b.c(n,2);

    % Contact point vector
    xc = b.x(i,:) + 0.5.*(b.x(j,:)-b.x(i,:));

    % Vector from center of sphere i to contact point
    rc = 0.5.*[(b.x(j,1)-b.x(i,1)) (b.x(j,2)-b.x(i,2)) (b.x(j,3)-b.x(i,3))];

    % Contact normal (normalized)
    n_c = (b.x(j,:)-b.x(i,:))./norm(b.x(j,:)-b.x(i,:));

    % Contact velocity between particles
    Vi = (b.v(j,:) + cross(b.omega(j,:), xc - b.x(j,:)) - (b.v(i,:) +
cross(b.omega(i,:), xc - b.x(i,:))));

    % Normal displacement (not used currently)
    U_n = (norm(b.x(j,:)-b.x(i,:)) - (b.r(i) + b.r(j)));

    % Normal displacement increment
    dU_n = b.dt.*dot(Vi, n_c).*n_c;

    % Relative shear-displacement increment vector
    dU_s = b.dt.*(Vi - dot(Vi,n_c)*n_c);

    % Relative angular velocity
    omegai = b.omega(j,:) - b.omega(i,:);
    % Normal component of omega_i
    omegai_n = dot(omegai, n_c).*n_c;
    % Tangential component of omega_i
    omegai_t = omegai - omegai_n;

    % Normalized tangential vector
    t_c = [0 0 0];
    if norm(omegai_t)~= 0
```

```
        t_c = omegai_t./norm(omegai_t);
    end

    % Twisting moment increment
    dM_n = -b.k_s*b.J_pb.*omegai_n.*b.dt;
    % Bending moment increment
    dM_t = -b.k_n*b.I_pb.*omegai_t.*b.dt;


% Normal force increment
    if failure == 1
        if U_n < 0
            Fn = (-b.K_n - b.k_n*b.A).*dU_n;
        end
    else
        Fn = -b.k_n*b.A.*dU_n;
    end

    % Incremental shear force
    if failure == 1
        if U_n < 0
            if norm(b.Fcs(n,:)) > norm(b.myy*b.K_n.*U_n) % Slip is checked,
                Fs = -b.k_s*b.A.*dU_s;% if shear force exceeds static
                if slip(n,1) == 0 % friction it is no longer incremented by
                    Fs2(n,:) = b.Fs(n,:); % the contact (only pb)
                    slip(n,1) = 1;
                end
                b.Ef = b.Ef + abs(dot(b.Fcs(n,:),dU_s)); % frictional
            else                                          % energy calculated
                Fs = (-b.K_s - b.k_s*b.A).*dU_s;
                b.Fcs(n,:) = b.Fcs(n,:) - b.K_s.*dU_s;
            end
        end
    else
        Fs = -b.k_s*b.A.*dU_s;
    end

    % Moment increment by shear force at contact point
    dMs = 0;
    if norm(Fs) ~= 0
        dMs = cross(rc, -Fs);
    end

    % Contact force calculation
    b.Fint(i,:) = b.Fint(i,:) - Fn - Fs;
    b.Fint(j,:) = b.Fint(j,:) + Fn + Fs;

    % Moment calculation
    b.M(i,:) = b.M(i,:) - dM_n - dM_t + dMs;
    b.M(j,:) = b.M(j,:) + dM_n + dM_t + dMs;

    % Damping
    b.Fd(i,:) = b.Fd(i,:) + b.c1*Vi;
    b.Md(i,:) = b.Md(i,:) + b.c2*omegai;
```

```
    b.Fd(j,:) = b.Fd(j,:) - b.c1*Vi;
    b.Md(j,:) = b.Md(j,:) - b.c2*omegai;

    % Storing spring forces
    b.Fn(n,:) = b.Fn(n,:) + Fn;
    b.Fs(n,:) = b.Fs(n,:) + Fs;
    b.Mn(n,:) = b.Mn(n,:) + dM_n;
    b.Ms(n,:) = b.Ms(n,:) + dM_t;

    % Calculation of strain energy
    b.Es = b.Es + [0.5*(norm(b.Fn(n,:)))^2/(b.k_n*b.A)
0.5*(norm(b.Fs(n,:)))^2/(b.k_s*b.A) 0.5*(norm(b.Mn(n,:)))^2/(b.k_s*b.J_pb)
0.5*(norm(b.Ms(n,:)))^2/(b.k_n*b.I_pb)];
    % Calculation of damping energy
    b.Ed = b.Ed + abs(dot(b.c1.*Vi, b.dt.*Vi));
end

% Calculation of kinetic energy
for n = 1:b.n
    b.Ek = b.Ek + 0.5*b.Mass*(norm(b.v(n,:)))^2 +
0.5*(2/5)*b.Mass*b.r(1)^2*(norm(b.omega(n,:)))^2;
end

% Calculation of external work
if strcmp(test,'Bend')
    for j=1:size(b.loaded,1)
        i = b.loaded(j);
        dU = b.dt*b.v(i,3);
        b.Eext = b.Eext + b.Fext(i,3)*dU;
    end
end
if strcmp(test,'Tensile')
    F = 0;
    for j=1:size(b.ends,1)
        i = b.ends(j);
        if b.x(i,1) < b.width/2
            F = F + b.F(i,1);
            k = i;
        end
    end
    b.Eext = b.Eext + abs(F*b.v(k,1)*b.dt);
end

% Total force
b.F = b.Fint + b.Fext + b.Fd;
b.M = b.M + b.Md;
```

```
%% This function calculates the bond forces based on the Timoshenko beam
%% theory

function [b, temp] = timoshenko(b,temp)
sz = size(b.c,1);
[b] = loc_coord(b);

for n = 1:sz
   i = b.c(n,1);
   j = b.c(n,2);

   xc = b.x(i,:) + 0.5.*(b.x(j,:)-b.x(i,:));
   Vi = (b.v(j,:) + cross(b.omega(j,:), xc - b.x(j,:)) - (b.v(i,:) +
cross(b.omega(i,:), xc - b.x(i,:))));
   omegai = b.omega(j,:) - b.omega(i,:);

   % local coordinate system and transformation matrix
   A = b.coord(:,:,n);
   transf = blkdiag(A,A,A,A);

   % global incremental displacements
   u(1:3) = b.v(i,:).*b.dt;
   u(7:9) = b.v(j,:).*b.dt;
   u(4:6) = b.omega(i,:).*b.dt;
   u(10:12) = b.omega(j,:).*b.dt;

   % global to local and back
   du = transf*u';
   Fl = b.K*du;
   Fg = (inv(transf))*Fl;

   % summing up increments
   b.Fint(i,:) = b.Fint(i,:) - Fg(1:3)';
   b.Fint(j,:) = b.Fint(j,:) - Fg(7:9)';
   b.M(i,:) = b.M(i,:) - Fg(4:6)';
   b.M(j,:) = b.M(j,:) - Fg(10:12)';

   % Damping
   b.Fd(i,:) = b.Fd(i,:) + b.c1*Vi;
   b.Fd(j,:) = b.Fd(j,:) - b.c1*Vi;
   b.Md(i,:) = b.Md(i,:) + b.c2*omegai;
   b.Md(j,:) = b.Md(j,:) - b.c2*omegai;

   % Storing the current beam loading
   b.Fn(n,:) = b.Fn(n,:) + Fg(1:3)';
   b.Mn(n,:) = b.Mn(n,:) + Fg(4:6)';

end

% Resultant forces
b.F = b.Fext + b.Fint + b.Fd;
b.M = b.M + b.Md;
```

```
% This function updates the particle positions using Verlet (or central
% difference method) for numerical integration

function [b] = verlet(b,test)

    for j = 1:size(b.others,1)
        i = b.others(j);
        % Translational motion
        b.v(i,:) = b.v(i,:) + b.dt.*(b.F(i,:))./b.Mass;
        b.x(i,:) = b.x(i,:) + b.dt.*b.v(i,:);
        % Rotational motion
        b.omega(i,:) = b.omega(i,:) +
b.dt.*(b.M(i,:))./(2/5*b.Mass*b.r(i)^2);
        b.theta(i,:) = b.theta(i,:) + b.dt.*b.omega(i,:);
    end

    % Particles with boundary conditions
    for j = 1:size(b.ends,1)
        i = b.ends(j);
        if strcmp(test, 'Tensile')
            b.v(i,2:3) = b.v(i,2:3) + b.dt.*(b.F(i,2:3))./b.Mass;
            b.x(i,:) = b.x(i,:) + b.dt.*b.v(i,:);
            b.omega(i,:) = b.omega(i,:) +
b.dt.*(b.M(i,:))./(2/5*b.Mass*b.r(i)^2);
            b.theta(i,:) = b.theta(i,:) + b.dt.*b.omega(i,:);
        end
        if strcmp(test, 'Bend') % Particles on the roller support
            if b.x(i,1) > b.width/2 && b.x(i,3) < 2*b.r(1)
                b.v(i,1) = b.v(i,1) + b.dt.*(b.F(i,1))./b.Mass;
                b.omega(i,2) = b.omega(i,2) +
b.dt.*(b.M(i,2))./((2/5)*b.Mass*b.r(i)^2);
                b.theta(i,2) = b.theta(i,2) + b.dt.*b.omega(i,2);
                b.x(i,1) = b.x(i,1) + b.dt.*b.v(i,1);
                % Particles on the fixed support
            elseif b.x(i,1) < b.width/2 && b.x(i,3) < 2*b.r(1)
                b.omega(i,2) = b.omega(i,2) +
b.dt.*(b.M(i,2))./((2/5)*b.Mass*b.r(i)^2);
                b.theta(i,2) = b.theta(i,2) + b.dt.*b.omega(i,2);
                b.x(i,:) = b.x(i,:) + b.dt.*b.v(i,:);
            else
                b.v(i,:) = b.v(i,:) + b.dt.*(b.F(i,:))./b.Mass; % Other end
                b.x(i,:) = b.x(i,:) + b.dt.*b.v(i,:);           % particles
                b.omega(i,:) = b.omega(i,:) +
b.dt.*(b.M(i,:))./(2/5*b.Mass*b.r(i)^2);
                b.theta(i,:) = b.theta(i,:) + b.dt.*b.omega(i,:);
            end
        end
    end

    % Damping forces reset
    b.Fd = zeros(b.n,3);
    b.Md = zeros(b.n,3);
```

```
%% This function calculates the average stress in the specimen volume as
%% described in Potyondy & Cundall (2004), Appendix 1.

function [b] = stresses(b,test)

for n = 1:size(b.c,1)
    % stress in particle from current contact
    Fr = b.Fn(n,:) + b.Fs(n,:);
    i = b.c(n,1);
    j = b.c(n,2);
    xc = b.x(i,:) + 0.5.*(b.x(j,:)-b.x(i,:));
    n_c = (b.x(j,:)-b.x(i,:))./norm(b.x(j,:)-b.x(i,:));
    b.stress{i} = b.stress{i} + (norm(xc - b.x(i,:)).*n_c.'*(-Fr))./b.V;
    b.stress{j} = b.stress{j} + (norm(xc - b.x(j,:)).*(-n_c).'*Fr)./b.V;
end

if strcmp(test,'Bend') % stress from the external load or support
    for n = 1:b.n
        if b.x(i,1) > b.width/2 && b.x(i,3) < 1.5*b.r(1) % Particles on the
            xc = b.x(n,:) - [0 0 b.r(1)];                % roller support
            n_c = (xc - b.x(n,:))./b.r(1);
            b.stress{n} = b.stress{n} + (norm(xc - b.x(n,:)).*n_c.'*(-[0 0
b.F(n,3)]))./b.V;
        elseif b.x(i,1) < b.width/2 && b.x(i,3) < 1.5*b.r(1) % Particles on
            xc = b.x(n,:) - [0 0 b.r(1)];               % the fixed support
            n_c = (xc - b.x(n,:))./b.r(1);
            b.stress{n} = b.stress{n} + (norm(xc - b.x(n,:)).*n_c.'*(-
b.F(n,:)))./b.V;
        elseif b.x(n,1) > b.width/2+b.r(1) - 0.01 && b.x(n,1) <
b.width/2+b.r(1) + 0.01 && b.x(n,3) > b.height - 1.5*b.r(1)
            xc = b.x(n,:) + [0 0 b.r(1)];
            n_c = (xc - b.x(n,:))./b.r(1);
            b.stress{n} = b.stress{n} + (norm(xc -
b.x(n,:)).*n_c.'*(b.Fext(n,:)))./b.V;
        end
    end
end

if strcmp(test,'Tensile')
    for i = 1:size(b.ends,1)
        n = b.ends(i);
        if b.x(n,1) < b.width/2
            xc = b.x(n,:) - [b.r(1) 0 0];
        else
            xc = b.x(n,:) + [b.r(1) 0 0];
        end
        n_c = (xc - b.x(n,:))./b.r(1);
        b.stress{n} = b.stress{n} + (norm(xc - b.x(n,:)).*n_c.'*(-[b.F(n,1) 0
0]))./b.V;
    end
end
% specimen porosity
n = ((b.width+2*b.r(1))*b.length*b.height -
b.V(1)*b.n)/((b.width+2*b.r(1))*b.length*b.height);

% sum of all stresses divided by total volume of specimen
```

```
% -> average stress state
catA = cat(3,b.stress{:});
b.avg_stress = ((1-n)/b.n).*sum(catA,3);
```

B Verification of the Timoshenko beam model

A simply supported beam with a circular cross section can be constructed by placing particles in a single row. Six beams with different number of particles and different lengths were formed and a static central load of 1 kN was applied to the beams as shown in Figure B1. The left end of the beam was fixed in all directions except rotations in the xz-plane. The right end was allowed to translate in horizontal x-direction and rotate in the xz-plane. The motion of the midspan and dynamics of the simulation are illustrated in Figure B2.

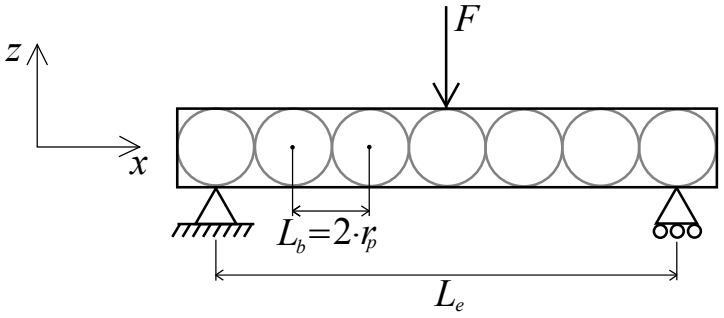

Figure B1: A simply supported beam with central loading. The beam is formed of 7 particles connected to each other by Timoshenko beams. The Timoshenko beam length L_b is two times the particle radius $r_p = 0.1$ m. The central load is $F = 1$ kN and the beam length is $L_e = 1.2$ m in this case.

For a beam with a circular cross section under a central point load and the above-mentioned boundary conditions the midspan deflection is given by

$$\delta_a = \frac{FL_e^3}{48EI} + \frac{FL_e f_s}{4GA}, \tag{B1}$$

where F is the central point load, L_e is the length of the beam, E is the Young's modulus of the material, G is the shear modulus, f_s is the form factor and I and A are the cross sectional properties given by Equations 18 and 9, respectively.

The deflections for beams that are formed of 3 to 31 particles are shown in table B1. The numerically obtained results are accurate for all the beams. However, the error increases as the number of particles increases. The largest error in the deflection is approximately 0.01 % with the 6.0 m beam.

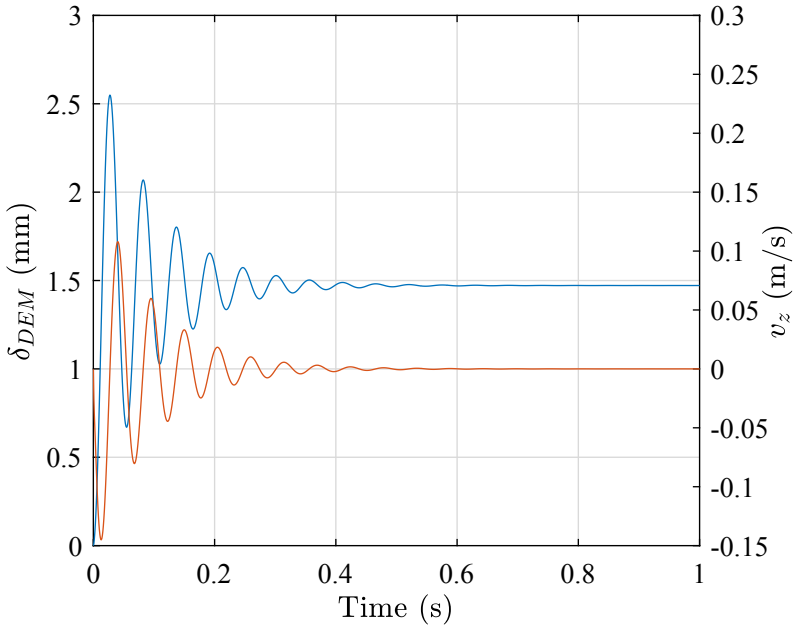

Figure B2: The deflection and velocity v_z of the midspan during loading of a simply supported beam with 15 particles and $L_e = 2.8$ m. The beam midspan vibrates until a sufficient amount of kinetic energy is dissipated as damping and the beam settles to a final deflection $\delta_{DEM} = 1.4719$ mm.

In addition to the static loading case, the dynamic behaviour of the Timoshenko beam model was verified with a free vibration test. A three particle representation of the simply supported beam (Figure B1) was used. This beam can be considered to have a concentrated central mass as the bonds are massless. The rotational inertia of the end particles was minimized by assigning them with significantly smaller masses

Table B1: Numerically obtained central deflection values compared to the analytical values.

Number of particles	L_e (m)	δ_{DEM} (mm)	δ_a (mm)	Error (%)
3	0.4	0.0065436	0.0065436	-2.24×10^{-7}
5	0.8	0.038551	0.038551	-8.89×10^{-7}
7	1.2	0.12148	0.12148	-5.38×10^{-6}
11	2.0	0.54201	0.54201	-1.67×10^{-4}
15	2.8	1.4719	1.4718	-0.0037
31	6.0	14.359	14.358	-0.0073

than with the central particle. The theoretical natural frequency for this beam is

$$f_n = \frac{1}{2\pi}\sqrt{\frac{K_{beam}}{m}}, \tag{B2}$$

where m is the mass of the central particle and K_{beam} is the beam's stiffness that is given by

$$K_{beam} = \frac{192EIGA}{4L_e^3GA + 48f_sEIL_e}. \tag{B3}$$

The beam was caused to vibrate by displacing the central particle by 1 mm (see Figure B3) and releasing it after a short hold. The particle size and the bond properties were the same as in the static case, the mass of the central particle was $m = 7.4$ kg and the length of the beam was $L_e = 0.4$ m.

The theoretical natural frequency given by Equation B2 was 723.29 Hz. The vibration frequency obtained from the DEM simulation was 723.17 Hz, which gives an error of only 0.017 %.

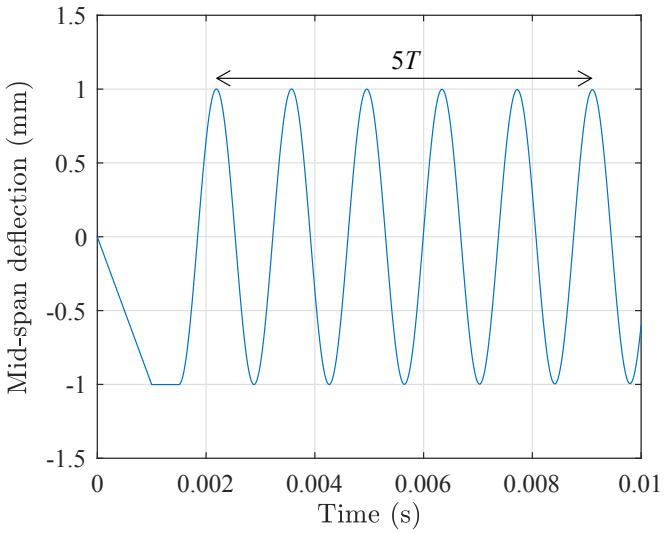

Figure B3: Free vibration of the beam constructed of three particles. The midspan is displaced by 1 mm during the first 1 ms and then set free at t = 1.5 ms. The natural frequency f_n is calculated from the 5 periods shown in the figure.

C Energy breakdown of simulations

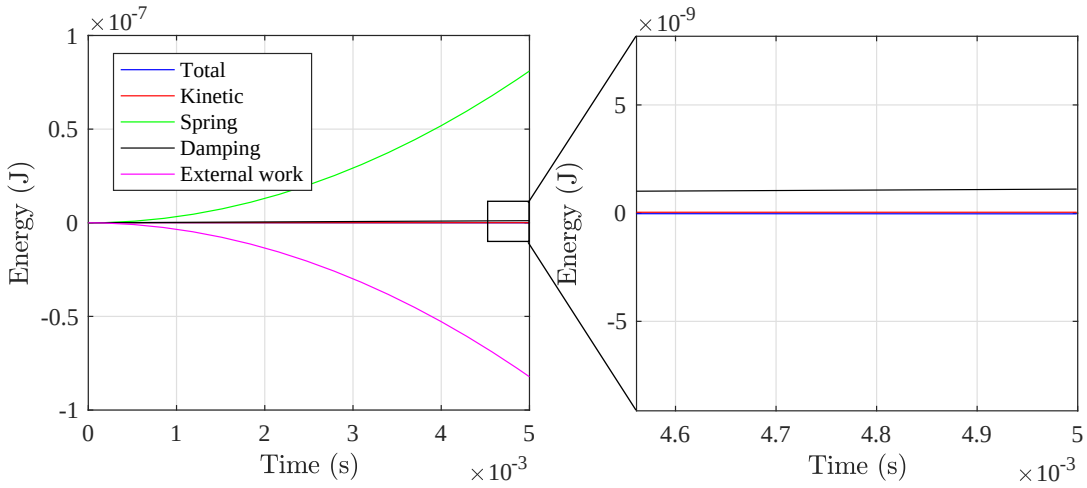

Figure C1: The breakdown of total energy during the quasistatic compression test of a random closepacked specimen with particle radius of $r_p = 12.5$ mm. The kinetic energy is negligible, which confirms that the simulation is quasistatic.

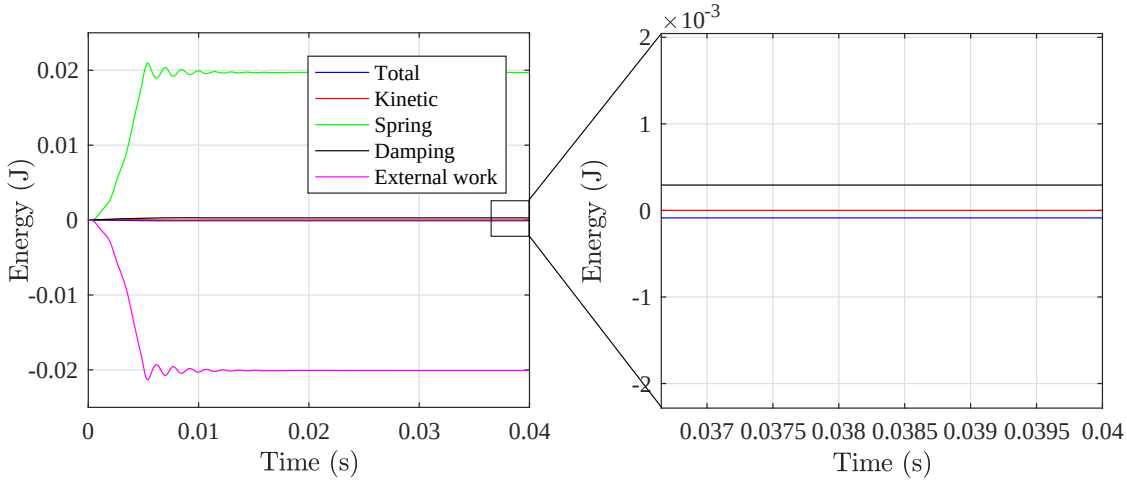

Figure C2: The breakdown of total energy during the three point flexural test of a random closepacked specimen with particle radius of $r_p = 12.5$ mm. The kinetic energy goes to zero as the beam settles to a state of equilibrium. The total energy of the system deviates slightly from zero.

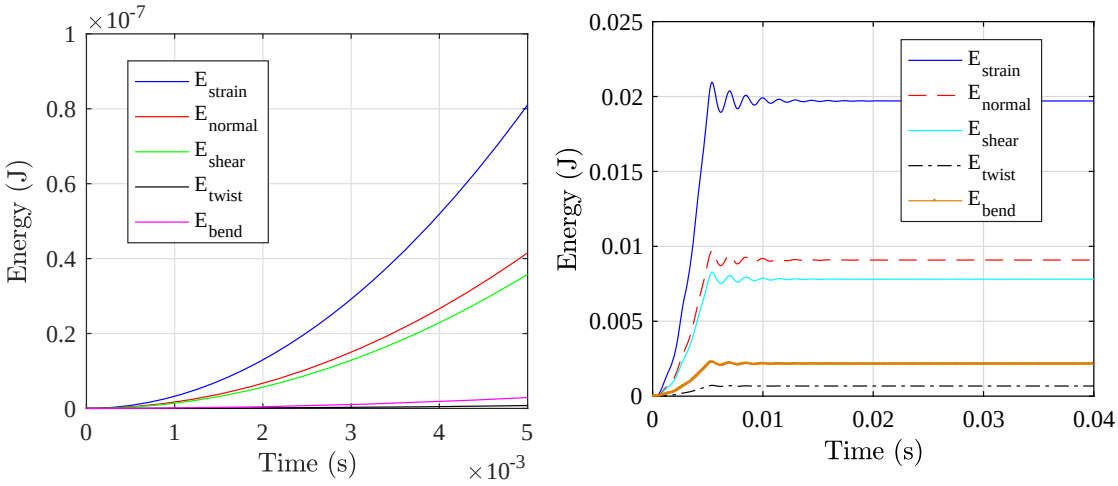

Figure C3: The energy breakdown of strain energy during (a) the quasistatic compression test and (b) the three point flexural test of a random closepacked specimen with particle radius of $r_p = 12.5$ mm.